EQUATION-OF-MOTION COUPLED CLUSTER MODEL WITH SINGLE AND DOUBLE SUBSTITUTIONS: THEORY AND APPLICATIONS

by

Sergey V. Levchenko

A Dissertation Presented to the

FACULTY OF THE GRADUATE SCHOOL

UNIVERSITY OF SOUTHERN CALIFORNIA

In Partial Fulfillment of the

Requirements for the Degree

DOCTOR OF PHILOSOPHY

(CHEMISTRY)

June 2005

Acknowledgments

First of all, I would like to express my sincere gratitude to Prof. Anna I. Krylov, a great person and mentor. Without her help and support, this work would be never accomplished. Her advises are especially valuable, since they are based on her own experience and high level of expertise, not only in science, but in many other aspects of life. She is always open to new ideas, and I appreciate very much that she taught me to value a completed work more than a promising one.

A large portion of the work presented here has been motivated and done in collaboration with Prof. Hanna Reisler and her group. I would like to thank Hanna for fruitful discussions and sharing an invaluable for theoreticians experimentalist's view and intuition. Her critical assessment of our work has improved it in many ways. Also, I would like to thank Andrei Demyanenko for his very effective and reliable help with one of the papers, and to Vladimir Dribinski and Aaron Potter.

It would take much longer time and much more effort to implement the EOM-CCSD gradients without the help of Tao Wang. I thank him for many hours of coding and extremely qualified help with C++.

I am grateful to Profs. John F. Stanton, Marcel Nooijen, Steven Gwaltney, and Rodney J. Bartlett for explaining methodological subtleties of EOM-CCSD and its gradients. Prof. John F. Stanton also provided us with the ACES II program, which I used for calculations at early stages of my work. Prof. Marcel Nooijen rendered us a great help by providing with ACES II reference data, which we used to debug our code.

I would like to express special thanks to my co-worker Lyudmila V. Slipchenko, who contributes energy and passion in everything she does, including motivation of her co-workers, which resulted in prompt implementation of the EOM-CCSD gradients code. She was also of great help in formatting this dissertation.

The most important things are usually mentioned at the beginning and at the end. So, at the end I would like to thank my friends Daniil Stolyarov, Elena Polyakova, Vladimir Dribinski, and Nikolai Markovski for their constant support and for making my life at USC interesting and enjoyable.

Contents

Acknowledgments **ii**

List of Tables **vi**

List of Figures **viii**

Abstract **xii**

Introduction **1**

Chapter I. Theory of EOM-CC **11**
I.1 Equation-of-motion formalism 11
I.2 Choice of the reference state 24
I.3 EOM-SF-CCSD model 29

Chapter II. EOM-CCSD analytic gradients. **33**
II.1 The analytic EOM-CCSD energy derivative and Lagrangian 33
II.1.1 Amplitude response equations 40
II.1.2 Orbital response equations 45

Chapter III. Electronic Structure of Halogen-Substituted Methyl Radicals: Excited States of CH_2Cl and CH_2F **51**
III.1 Introduction 52
III.2 Results and discussion 55
III.2.1 Computational details 55
III.2.2 CH_2Cl 59
III.2.3 CH_2F 68
III.2.4 Comparisons of the excited states in the CH_3 $\rightarrow CH_2F \rightarrow CH_2Cl$ sequence 74
III.3 Conclusions 79

Chapter IV. Electronic Structure of Halogen-Substituted Methyl Radicals: Equilibrium Geometries and Vibrational Spectra of CH_2Cl and CH_2F **82**
IV.1 Introduction 83

IV.2 Theory 87
IV.3 Results and discussion 92
IV.3.1 Computational details 92
IV.3.2 CH_2Cl 96
IV.3.3 CH_2F 99
IV.3.4 CH_3 104
IV.4 Conclusions 108

Chapter V. Rydberg-valence interactions in $CH_2Cl \rightarrow CH_2$ + Cl photodissociation: Dependence of absorption probability on ground state vibrational excitation 110
V.1 Introduction 111
V.2 Experimental results 113
V.3 Electronic structure calculations 118
V.3.1 Computational details 118
V.3.2 Characterization of the two lowest $^2A_1$ excited states of CH_2Cl 119
V.3.3 Rydberg-valence interactions in the lowest excited states of CH_2Cl 125
V.4 Enhancement of hot bands' intensities 130
V.5 Conclusions 134

Chapter VI. EOM-SF-CCSD versus EOM-EE-CCSD: electronic states of cyclobutadiene 136
VI.1 Molecular orbitals and characterization of low-lying valence states of cyclobutadiene 137
VI.2 Vertical and adiabatic excitation energies of cyclobutadiene 141

Chapter VII. EOM-SF-CCSD analytic gradients: equilibrium geometries and transition structures of the low-lying valence states of cuclobutadiene 148

General conclusions 153

Future work 155

Reference List 157

Appendix I 179

Appendix II 182
AII.1 Variational properties of the EOM functional 182
AII.2 Derivation of orbital response equations 183

Appendix III 185

List of Tables

II.1 Excited state's effective one- and two-electron density matrices defined by Eqns. (II.7,II.8)[a]. Intermediates are summarized in Table II.2. . 35

II.2 Intermediates used in Eqns. (II.41,II.42) and in the excited states' effective one- and two-particle density matrices defined by Eqns. (II.7,II.8). 44

III.1 Ground state equilibrium geometries for CH_2X (X=Cl,F,H) radicals, and CH_2F cation. 56

III.2 Excited states of CH_2Cl radical. EOM-CCSD/6-311(3+,3+)G(3df, 3pd), pure angular momentum. 61

III.3 Excitation energies (eV) for CH_2Cl radical. A comparison between EOM-CCSD, CIS, CIS(D), TD-DFT/B3LYP, and MRCI methods. . 66

III.4 Excited states of CH_2F radical. EOM-CCSD/6-311(3+,3+)G(3df, 3pd). 69

III.5 Excitation energies (eV) for CH_2F radical. A comparison between EOM-CCSD, CIS, CIS(D), and TD-DFT/B3LYP methods[a]. 73

III.6 Excited states of CH_3 radical. EOM-CCSD/6-311(3+,3+)G(3df,3pd), pure angular momentum. 75

III.7 Excitation energies (eV) for CH_3 radical. A comparison between EOM-CCSD, CIS, CIS(D), TD-DFT/B3LYP, and MRCI methods. . 78

IV.1 Calculated ground state geometries of CH_2X (X=Cl,F,H) radicals. . 93

IV.2 Ground state rotational constants (MHz) for CH_2X radicals (X=Cl, F, H)[a]. 94

IV.3 CH_2Cl. Calculated harmonic vibrational frequencies ω_e and experimental values ω_{01}, cm^{-1}. The relative differences, $\Delta = \frac{(\omega_e - \omega_{01})}{\omega_{01}} \cdot 100\%$, are shown in parentheses. 97

IV.4 CH_2Cl. Parameters (10^{-6} a.u.) of the analytical fit (IV.18) of the OPLA effective potentials. 98

IV.5 CH_2F. Calculated harmonic vibrational frequencies ω_e and experimental values ω_{01}, cm^{-1}. The relative differences, $\Delta = \frac{(\omega_e - \omega_{01})}{\omega_{01}} \cdot 100\%$, are shown in parentheses. 100

IV.6 CH_2F. Parameters (10^{-6} a.u.) of the analytical fit (IV.18) of the OPLA effective potentials. 101

IV.7 CH_3. Calculated harmonic vibrational frequencies ω_e and experimental values ω_{01}, cm^{-1}. The relative differences, $\Delta = \frac{(\omega_e - \omega_{01})}{\omega_{01}} \cdot 100\%$, are shown in parentheses. 105
IV.8 CH_3. Parameters (10^{-6} a.u.) of the analytical fit (IV.18) of the OPLA effective potentials. 106
IV.9 Calculated and the experimental values for the OPLA fundamental transition, cm^{-1}. The OPLA adiabatic and diabatic effective potentials are calculated at CCSD(T)/6-311++G(3df,3pd) level of theory. 108
IV.10 Calculated and the experimental values for the OPLA fundamental transition, cm^{-1}. The OPLA adiabatic and diabatic effective potentials are calculated at DFT(B3LYP)/6-311++G(3df,3pd) level of theory. 108
V.1 Ground and excited state geometries of CH_2Cl radical: 120
V.2 Calculated harmonic vibrational frequencies ω_e of the ground and excited states of CH_2Cl. 121
VI.1 Optimized geometries of the rectangular ground X^1A_g state of cyclobutadiene. The bondlength alternation, Δ_{CC}, is also shown. Bondlengths are in angstrom, angles — in degrees. 140
VI.2 Total energies (hartree) of the ground X^1A_g state of cyclobutadiene, and vertical excitation energies (eV) at the X^1A_g equilibrium geometry[a]. 142
VI.3 Total energies (hartree) of the ground X^1B_{1g} state of cyclobutadiene, and vertical excitation energies (eV) at the 1^3A_{2g} equilibrium geometry[a]. 142
VI.4 Vertical excitation energies (eV) at rectangular singlet (RS) and square triplet (ST) geometries. The geometries are specified in the footnotes. D_{4h} symmetry labels are shown in parentheses. The X^1A_g(X^1B_{1g}) is the lowest state at both geometries. 145
AI.1 Intermediates used in Eqns. (AI.3-AI.10). To avoid storage of large 6-index quantities, intermediates which have to be updated at each iteration of diagonalization procedure were introduced. 181

List of Figures

1 Illustration of the concepts of the reference determinant $|\Phi_0>$, excitation operators $\hat{R}$, $\hat{T}$, and their action on $|\Phi_0>$. The flexibility in the choice of the operator $\hat{R}$ is also demostrated by a few examples. More examples are shown in Fig. I.1. 3

I.1 Sets of determinants generated from different reference determinants. In each set, determinants required to construct spin-eigenfunctions are connected by thin solid lines. Determinants contributing to a diradical's eigenfunction with large weights are connected by dashed lines. The imbalance occurs when the connected determinants are generated by different levels of excitation. 25

III.1 Vertical excitation energies for CH_2Cl (a), CH_2F (b), and CH_3 (c). Intensities of the transitions are proportional to the oscillator strengths (no Franck-Condon factors are taken into account). Empty bars are used to show positions of forbidden transitions, i.e., those for which oscillator strength is zero due to the symmetry. Transitions are defined as parallel when the transition dipole moment is parallel to the CX bond, and perpendicular otherwise. 62

III.2 Molecular orbital picture for the ground and valence excited states of CH_2Cl radical. $7a_1$ orbital is the σ_{CCl} bonding orbital; $2b_1$ orbital is the (p-p)π_{CCl} bonding orbital; $3b_2$ is the $3p_x$ lone pair on Cl atom; $3b_1$ orbital is the singly occupied π-anti-bonding orbital; and virtual $11a_1$ orbital is the σ^*_{CCl}-anti-bonding orbital. 63

III.3 Errors in the TD-DFT excitation energies vs spherical average of the charge distribution for the CH_2Cl radical. 67

III.4 Molecular orbital picture for the ground and valence excited states of CH_2F radical. $6a'$ is the σ_{CF} bonding orbital; $2a''$ is the $2p_z$ lone pair on F atom; $7a'$ is the carbon p-orbital hosting the unpaired electron; and virtual $12a'$ orbital is the σ^*_{CF}-anti-bonding orbital. 70

III.5 Molecular orbital picture for the ground and valence excited states of CH_3 radical. 1 and 2 e' are the doubly degenerate combination of the localized C-H bonds; and $1a''_2$ is carbon's p-orbital hosting the unpaired electron. 76

III.6 Solar flux at different altitudes in the atmosphere. DNA action spectrum, i.e., the probability of DNA damage by UV radiation at various wavelengths, is also shown. 81
IV.1 Illustration of positive and negative anharmonicities. 84
IV.2 Harmonic (dashed line) and anharmonic (solid line) OPLA adiabatic effective potentials for the CH_2Cl radical [CCSD(T)/6-311(+,+)G(3df, 3pd)]. The positions of the zero and first excited vibrational levels are shown by horizontal lines. The calculated and experimental values for the fundamental transition are shown by vertical arrows. 99
IV.3 Anharmonic (solid line) OPLA adiabatic effective potential for the CH_2F radical [CCSD(T)/6-311(+,+)G(3df,3pd)]. The dashed curve represents the harmonic part of the potential at the optimized non-planar (C_s) geometry. The corresponding harmonic frequency is also shown. The negative curvature at the planar (C_{2v}) geometry (i.e., at the barrier) yields the imaginary frequency of 437i cm^{-1}. The positions of the zero and first excited levels are shown by horizontal lines. The calculated and experimental values of the OPLA fundamental transition are shown by vertical arrows. 102
IV.4 Harmonic (dashed line) and anharmonic (solid line) OPLA adiabatic effective potentials for the CH_3 radical [CCSD(T)/6-311(+,+)G(3df, 3pd)]. The positions of the zero and first excited levels are shown by horizontal lines. The calculated and experimental values for the OPLA fundamental transition are shown by vertical arrows. 107
V.1 CH_2Cl photodissociation at 266 nm (37,594 cm^{-1}) using (a) He, (b) CF_4:He (1:7), and (c) Ar carrier gases. Cl($^2P_{3/2}$) signals are plotted as a function of the total c.m. photofragment translational energy, E_t. The arrows indicate the maximum translational energy allowed for dissociation from the ground vibrational state to Cl($^2P_{3/2}$) + CH_2(X^3B_1). 115
V.2 Potential energy curves for the ground X^2B_1 and the two lowest $^2A_1$ excited states along the C-Cl coordinate (all other degrees of freedom are held at their ground state equilibrium values). All curves are shifted such that the ground state energy at equilibrium is zero. . . 123
V.3 Dipole strength dependence on the C-Cl distance for the $1^2A_1 \leftarrow X^2B_1$ and $2^2A_1 \leftarrow X^2B_1$ transitions. The vertical arrow indicates the ground state equilibrium C-Cl distance. 124

V.4 Spherical average of the electron density, $\langle r^2 \rangle$, as a function of the C-Cl distance for the ground and the two lowest $^2A_1$ excited states of the CH_2Cl radical (upper panel). The lower panel shows changes in the excited state density relative to the ground state, i.e., $\Delta\langle r^2 \rangle = \langle r^2 \rangle_{ex} - \langle r^2 \rangle_{gr}$ (this subtracts changes due to molecular size increase at larger molecular separations). The dashed line corresponds to the average value for both states. The vertical arrow indicates the ground state equilibrium C-Cl distance. 127
V.5 $\langle x^2 \rangle$, $\langle y^2 \rangle$, and $\langle z^2 \rangle$ components of the total electron charge distribution for 2^2A_1 (upper panel) and 1^2A_1 (lower panel) as a function of the C-Cl bond length. The molecular plane is the XZ-plane, the C-Cl bond defines the Z-axis. 129
V.6 Illustration of the hot bands' enhancement mechanism. Horizontal lines at the bottom of the potential energy curve for the ground state represent vibrational levels of the C-Cl stretch. Vertical arrows show electronic excitation upon absorption of a 266 nm photon. Transition dipole strength is shown in the inset. 132
VI.1 Molecular π-orbitals derived from carbons' p-orbitals at the 1^3A_{2g} equilibrium geometry (left panel), and at the X^1A_g equilibrium geometry (right panel). Electronic configuration of the triplet state is shown. 138
VI.2 Leading electronic configurations in the EOM-SF-CCSD wave functions of the valence states of cyclobutadiene at the square (left panel) and rectangular (right panel) geometries. For the D_{4h} geometries (left panel), D_{2h} symmetry labels are given in parentheses. 139
VI.3 Equilibrium geometries of the 1^3A_{2g} (left) and X^1A_g (right) references, optimized at the CCSD(T)/cc-pVTZ level of theory. Bond lengths are in angstroms, angles — in degrees. 140
VI.4 Excitation energies of the valence states of cyclobutadiene relative to the ground X^1A_g state at the CCSD(T)/cc-pVTZ optimized geometry. 143

VII.1 Optimized geometries and transition structures of the four low lying valence states of cyclobutadiene. For the square geometry, the values of C-H and C-C bond lengths, Å, for different states are separated by commas. The results are shown for the following methods (from top to bottom): EOM-SF-CCSD/cc-pVTZ(mixed), EOM-SF-CCSD/[3s2p1d/2s], MR-CCSD/[3s2p1d/2s], MR-BWCCSD/cc-pVDZ. The parameters for the rectangular ground state equilibrium geometry are shown for the following methods (starting from top): EOM-SF-CCSD/cc-pVTZ(mixed), CCSD(T)/cc-pVTZ, EOM-SF-CCSD/[3s2p1d/2s], MR-CCSD/[3s2p1d/2s]. Only the second closed-shell singlet is stabilized by the rhombic distortion, and the corresponding equilibrium geometries are shown for EOM-SF-CCSD/cc-pVTZ(mixed) (upper number) and MR-CCSD/[3s2p1d/2s] (lower number). On the lower panel, π molecular orbitals and electronic configuration of triplet reference are shown. 150

VII.2 Electronic configurations of the four low lying states of CB at the square geometry, and their change upon stabilizing distortions. In parentheses, the type of molecular geometry stationary points is indicated for each state: TS stands for a transition structure, while EG denotes an equilibrium geometry. 151

Abstract

Theory of the equation-of-motion coupled cluster model with single and double substitutions (EOM-CCSD) and its analytic gradients is presented. Details of implementation within the *Q-CHEM ab initio* package are discussed. EOM-CCSD is applied to analyze electronically excited states of halogen-substituted methyl radicals, CH_2Cl and CH_2F. The systematic changes in the equilibrium structures, vibrational frequencies and properties of the ground and electronically excited states for the $CH_3 \rightarrow CH_2F \rightarrow CH_2Cl$ sequence are explained. The observed enhancement of the hot-band intensities in the photoabsorption of the CH_2Cl radical is also explained, and the role of CH_2Cl in the atmosphere is re-evaluated. In addition, a strong anharmonicity in the out-of-plane vibrational mode of the halogen-substituted methyl radicals is characterized by a high level of theory. The discrepancy between the experimental observations that suggested planarity and the calculated non-planar equilibrium structure of the CH_2F radical is explained by: (i) incomplete orbital following (ESR measurements), and (ii) a low barrier for the interconversion between the two non-planar structures, resulting in zero-point vibrational level being above the barrier (IR spectroscopy measurements).

Cyclobutadiene is used as a benchmark system to demonstrate the advantages of the spin-flip version of EOM-CCSD, EOM-SF-CCSD, over its traditional version, EOM-EE-CCSD, for diradical systems. EOM-SF-CCSD is applied to describe low-lying electronic states of cyclobutadiene and their equilibrium geometries and transition structures. It is shown that EOM-SF-CCSD provides the best trade off between accuracy and computational cost among the existing theoretical models for this problem.

Introduction

The equation-of-motion (EOM) formalism is one of the approaches used in quantum mechanics for the direct calculation of energy differences rather than total energies [164]. It is always energy differences between the states of the system which are observed experimentally. Chemistry and spectroscopy are often concerned about energy differences that are many orders of magnitude smaller than total energies. This is the crux of a major challenge faced by the electronic structure theory — tiny errors in total energies may result in very large errors in energy differences. For example, one percent of the ethylene total energy (≈-78 hartree) is about 21 eV, which exceeds even the ionization potential of the molecule (∼10.5 eV)! That is why EOM as well as other approaches formulated for energy differences (e.g., electron propagator or Green function, and response techniques) are potentially more accurate than approximate methods of the similar complexity formulated for the states' total energies. However, this potential can be fulfilled only if the realization ensures a balanced treatment of the states of interest.

Different formalisms often yield very similar working equations [164] — for example, the linear response coupled-cluster (CC) model [124, 198, 214] is identical to EOM-CC [47, 85, 131, 132, 140, 214, 230]. However, each of the approaches offers certain advantages. The most appealing property of the linear response formalism is that it mimics optical spectroscopy, e.g., an excited state energy is obtained as a pole of the first order response function [95, 198]. The strength of EOM theory is that it makes very clear distinction between the reference and target states. In the context of coupled-cluster methods, this freedom in the reference state choice has enabled extension of EOM-CC models from treating electronically excited closed-shell molecules towards ionized and open-shell systems [182, 231, 253] (for detailed reviews, see Refs. [18, 188]). Finally, the tremendous flexibility of the EOM-CC ansatz was exploited in the development of the EOM spin-flip (SF) CC model which targets systems with extensive electronic degeneracies, such as diradicals, triradicals, and bond breaking [134].

Briefly, the EOM-CC approximation (ansatz) for the exact electronic wave function can be written as follows:

$$|\Psi > \approx \hat{R} e^{\hat{T}} |\Phi_0 >$$

where $|\Phi_0 >$ is a reference determinant, and $\hat{R}$ and $\hat{T}$ are excitation operators (see Fig. 1). These operators are parametrized, and the problem of solving the electronic

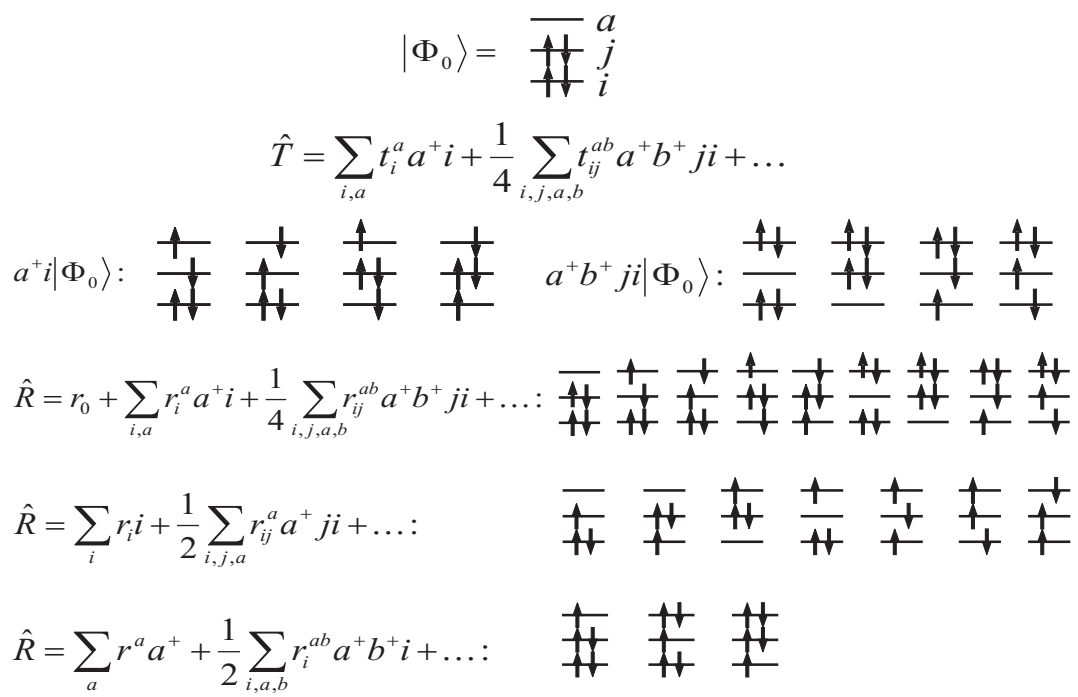

Figure 1: Illustration of the concepts of the reference determinant $|\Phi_0>$, excitation operators $\hat{R}$, $\hat{T}$, and their action on $|\Phi_0>$. The flexibility in the choice of the operator $\hat{R}$ is also demostrated by a few examples. More examples are shown in Fig. I.1.

Schödinger equation:

$$H|\Psi> = E|\Psi>$$

is reformulated in terms of these parameters. An important property of the operators $\hat{R}$ and $\hat{T}$ is that they comute (since they are both excitation operators from the same reference). Substituting the above ansatz into the Schödinger equation, we get:

$$H\hat{R}e^{\hat{T}}|\Phi_0> = E\hat{R}e^{\hat{T}}|\Phi_0>$$

Multiplying both sides of this equation by $e^{-\hat{T}}$, and using the comutation property of $\hat{R}$ and $\hat{T}$, we arrive at the following equation:

$$\bar{H}\hat{R}|\Phi_0>=E\hat{R}|\Phi_0>$$

where $\bar{H} = e^{-\hat{T}}He^{\hat{T}}$. The parameters for the operator $\hat{T}$ are first found from the above equation at the condition $\hat{R} = \hat{1}$, and then remain fixed as we solve the equation for $\hat{R}$. Since $\hat{R}$ is linearly parametrized, the problem of finding these parameters reduces to diagonalization of the $\bar{H}$ matrix in the basis of $|\Phi_0>$ and the excited determinants, with the highest excitation level being equal to that present in $\hat{R}$. It is important to understand, that the basis for the independent solution for $\hat{R}$ and $\hat{T}$, as well as for the exponential ansatz itself, is the perturbative nature of electron correlation, with the zeroth-order approximation starting from the reference determinant $|\Phi_0>$, and has rigorous mathematical foundation in the many-body perturbation theory.

Due to the separate treatment of the correlation in the reference and target states, the EOM-CC model provides means not only for accurate calculation of energy differences and properties of several states simultaneously and at a relatively low computational cost, but also yields a very compact representation of the target states. Consequently, the electronic structure of the EOM-CC target states can be easily

characterized and classified in chemically relevant terms, i.e., as changes in population of bonding, antibonding, non-bonding, and Rydberg orbitals, which establishes new standards for justification, use, and development of chemical intuition.

This dissertation presents general theory and implementation of the energy, properties, and analytic gradients for equation-of-motion coupled-cluster models with single and double substitutions (EOM-CCSD) for excitation energies (EOM-EE-CCSD) [124, 214, 230] and its spin-flip counterpart (EOM-SF-CCSD) [134, 147]. EOM-EE-CCSD accurately describes electronically excited states that are dominated by a single electron promotion in a single-step computational procedure that simultaneously calculates several electronic states, and provides a balanced account of both dynamical and non-dynamical correlation. This results in a robust and efficient computational scheme that does not require an arbitrary active space selection for each state of interest, and is free from root-flipping, intruder states, size-consistency errors, and other problems associated with multi-reference models. For example, no special treatment of near-degenerate excited states or states with strong Rydberg-valence mixing is required within EOM-CC formalism, while these situations pose a challenge for multi-reference methods [39, 76]. However, EOM-EE-CCSD would fail when the reference state acquires significant multi-configurational character due to a small HOMO-LUMO gap, e.g., at the dissociation limit or in diradicals. This can be cured by employing high-spin reference state and solving the EOM equations in the M_s=-1 subspace, as it is done in the EOM-SF-CCSD [134, 147] method. Thus, EOM-SF-CCSD [134, 147] extends single-reference EOM-CC methodology to such

chemically important cases as diradicals, triradicals, and single bond-breaking processes. This is demonstrated by application of EOM-EE-CCSD and EOM-SF-CCSD to cyclobutadiene, a system in which the electronic degeneracy is controlled by simple variations of geometry (see Chapter VI).

The importance of calculating energy derivatives analytically has been recognized several decades ago [94, 191]. Since calculations of global potential energy surfaces (PESs) with a subsequent interpolation are feasible only for very small systems [52], practical computational studies of spectroscopic and dynamical properties often focus on stationary points of PESs and thus require energy derivatives. For example, first derivatives allow one to characterize molecular equilibrium geometries, transition structures, and to calculate minimum energy paths and intrinsic reaction coordinates.

In principle, derivatives of any order can be computed numerically from total energies by a finite difference procedure. Since such calculations require only total energies, they can be performed for any electronic structure method. However, this universality of the numerical derivatives is their only advantage. The numerical evaluation of energy gradient for a system with N degrees of freedom requires $2N$ single point energy calculations (in the absence of symmetry). Moreover, the finite difference procedure often encounters numerical problems, such as poor convergence, numerical noise, etc. Calculation of analytic gradients is free of numerical instabilities, and can be performed approximately at a cost of a single point energy calculation, which results in significant time savings for polyatomic molecules.

Conceptually, derivation of analytic gradient expressions is nothing but differentiation of an energy expression with respect to (w.r.t.) nuclear coordinates. However, this seemingly simple procedure becomes rather cumbersome for wave functions that are not fully variationally optimized and thus do not satisfy the Hellmann-Feynman theorem. In these cases, the energy derivative w.r.t. perturbation ξ includes, in addition to the expectation value of the derivative of the Hamiltonian, terms that contain derivatives of the wave function $\Psi(\alpha)$ w.r.t non-variational parameters α:

$$\frac{dE}{d\xi} =< \Psi|\frac{\partial H}{\partial \xi}|\Psi > +2 < \Psi|H|\frac{\partial \Psi}{\partial \alpha} > \cdot \frac{\partial \alpha}{\partial \xi}, \tag{1}$$

where $E =< \Psi|H|\Psi >$ and $< \Psi|\Psi >= 1$. The efficiency of analytic derivatives calculation stems from the realization of Handy and Schaefer [94] that the latter term in Eq. (1) does not require evaluation of the derivatives of the non-variational parameters α w.r.t. *all* degrees of freedom, rather solving only *one* perturbation-independent linear equation for each type of the parameters (the Z-vector approach) [94]. Thus, $(2n)^{th}$ and $(2n+1)^{th}$ energy derivatives require solving only n^{th} order coupled-perturbed (and some related) equations.

Alternatively, the terms due to non-variational parameters can be evaluated by using the Lagrangian approach (see, for example, Refs. [39, 81, 92, 97, 239]). In this method, instead of the energy functional, one introduces a new functional:

$$L(\alpha, \lambda) = E + \lambda \cdot f(\alpha), \tag{2}$$

where λ denotes an undetermined Lagrange multiplier and $f(\alpha) = 0$ is an equation that defines values of the parameters α. This new functional, a Lagrangian, is stationary w.r.t. α and multipliers λ are defined such that $\frac{\partial L}{\partial \lambda} = 0$. Thus, the Hellmann-Feynman theorem is satisfied for the new functional. Since the value of the Lagrangian is equal to that of the original energy functional when the optimal values of all the parameters are used, the gradient of the new functional is equal to that of the energy:

$$\frac{dE}{d\alpha} = \frac{\partial L}{\partial \alpha}|_{\lambda=\lambda_{opt}}$$

This approach allows one to incorporate all the equations determining the non-variational parameters in the energy functional in a general way. Note that the very existence of the Lagrangian implies the possibility to avoid evaluation of the derivatives of the non-variational parameters w.r.t. all degrees of freedom, as shown by Handy and Schaefer [94].

A general theory of analytic gradients for the EOM-CCSD methods was developed by Stanton and Gauss [229, 231–233] using direct differentiation of energy functional and the Z-vector technique of Handy and Schaefer [94]. The alternative derivations, which employed the Lagrangian approach, have also been reported [92, 239]. Reduced orbital space EOM-CC optimized geometries have been presented in Ref. [13], although no details of derivation/implementation were given. We employed the Lagrangian approach (see, for example, Refs. [97] and [39,81,92,239])

to derive programmable gradient expressions for the EOM-EE-CCSD and EOM-SF-CCSD models for UHF and RHF references, and including the case of frozen core/virtual orbitals. In the spin-orbital formulation, the EOM-SF-CCSD analytic gradient expressions are identical to the EOM-EE-CCSD ones, however the spin-symmetry of the EOM-amplitudes and implementation are different, as discussed below. The EOM-SF-CCSD analytic gradients are applied to calculate equilibrium geometries and transition structures of the low lying excited states of cyclobutadiene (see Chapter VII).

The new code for the EOM-CCSD models and their analytic gradients is implemented by me in the *Q-CHEM* electronic structure package [128]. This implementation is based on the spin-orbital formalism, and exploits the C++ tensor library developed by Krylov and co-workers [138].

As was mentioned above, the EOM-CCSD model allows one to accurately describe several electronic states simultaneously, and regardless of their character and energy separation. This feature is especially important for an adequate description of the excited states of doublet radicals. These systems often have low ionization potentials, and, consequently, low lying Rydberg states, which can significantly affect their spectroscopic properties. A failure to treat valence and Rydberg states in a balanced fashion can lead to an incorrect interpretation and prediction of spectroscopic data. The advantage of EOM-CCSD over other quantum chemical methods in treating this problem is demonstrated by the application to the methyl radical CH_3, and

halogen-substituted methyl radicals CH_2Cl and CH_2F (Chapters III and V). In addition, I present an answer for an old puzzle concerning their ground state equilibrium properties (Chapter IV).

Calculations were performed using the ACES II [235] and Q-Chem [128] *ab initio* programs. ACES II was used for all CCSD [192] and CCSD with non-iterative triple corrections [CCSD(T)] [193] calculations, as well as EOM-EE-CCSD calculations of the doublet radicals. All applications of the density functional theory (DFT) and EOM-SF-CCSD method were performed using Q-Chem. Q-Chem was also used for the EOM-EE-CCSD calculations of cyclobutadiene. Some basis sets used in this work were obtained from the EMSL database [1].

Chapter I. Theory of EOM-CC

This chapter reviews the general EOM formalism and explains the importance of the reference state choice. Our derivation of EOM-CC emphasizes the variational properties of the theory and does not invoke the projective approach. We demonstrate [147], for the first time, that the killer condition is rigorously satisfied in single-reference EOM-CC theories, although, in Surján terms, "for the wrong reason" [240]. The presentation employs operator algebra — see Refs. [154, 155] for a very compact and practical summary. The general formalism is followed by the presentation of working equations and the implementation of the EOM-SF-CC model with single and double excitations (EOM-SF-CCSD).

I.1 Equation-of-motion formalism

Consider a general (not necessarily Hermitian) operator $\bar{H}$ and two of its eigenstates, $|0>$ and $|f>$, with eigenvalues E_0 and E_f, respectively:

$$\bar{H}|0>= E_0|0> \tag{I.1}$$

$$\bar{H}|f>= E_f|f> \tag{I.2}$$

For a non-Hermitian operator, bra-eigenstates are not Hermitian conjugates of ket-eigenstates: $< k| \neq (|k >^{+})$. Moreover, neither bra nor ket eigenstates form an orthonormal set. However, bra's and ket's form a biorthogonal set, $< k|l >= \delta_{kl}$, provided that the corresponding eigenvalues are non-zero. A general excitation operator $R(f)$ is defined such that it promotes a system from the initial (or reference) state $|0>$ into the final state $|f>$:

$$R(f)|0 >= |f > \tag{I.3}$$

No assumptions are made about the nature of the initial and final states: they can be the ground and electronically excited states (or any two electronic states) of an N-electron system, or states of an N-electron and an ionized or detached system, etc. It is convenient to represent the excitation operator R from Eq. (I.3) by the following bra-ket form:

$$R(f) \equiv |f >< 0| \tag{I.4}$$

The so defined operator is of rank one [1] and can act on any reference state $|\tilde{0}>$:

$$R(f)|\tilde{0}>=|f><0|\tilde{0}> \tag{I.5}$$

Therefore, for any state $|\tilde{0}>$ which has a non-zero overlap with the exact reference state $<0|$:

$$[\bar{H},R(f)]|\tilde{0}>=\omega_{0f}R(f)|\tilde{0}> \tag{I.6}$$

where $[\bar{H},R(f)]=\bar{H}R(f)-R(f)\bar{H}$, and $\omega_{0f}=E_f-E_0$. The above equation shows that if no approximations have been made for the excitation operator $R(f)$, the exact energy difference ω_{0f} can be computed without an explicit calculation of the initial and final states.

[1]The rank of a linear operator A acting in a carrier space S equals to the dimensionality of the image space $span\{Ax\}$, $x\in S$. Note that the following alternative representation of the excitation operator from Eq. (I.3):

$$R'(f)\equiv|f><0|+A(\hat{1}-|0><0|),$$

where A is any operator, does not ensure the unit rank of the operator:

$$R(f)|g>=|f><0|g>=0$$
$$R'(f)|g>=|f><0|g>+A(\hat{1}|g>-|0><0|g>)=A|g>$$

for any state $|g>\neq|0>$. Note that the operators $R(f)$ and $R'(f)$ act differently on $|\tilde{0}>$, and that $R'(f)$ does not satisfy Eqns. (I.5,I.6).

By introducing the de-excitation operator [2] $L(f) = |0 >< f|$, the transition energy ω_{0f} can be written as a general expectation value of the non-Hermitian operator $\bar{H}$:

$$\omega_{0f} = \frac{< \tilde{0}|L(f)[\bar{H}, R(f)]|\tilde{0} >}{< \tilde{0}|L(f)R(f)|\tilde{0} >} \tag{I.7}$$

In expression (I.7) (as well as in the subsequent presentation), the bra reference state $< \tilde{0}|$ can be chosen to be a Hermitian conjugate of the ket reference state. Form (I.7) provides a useful functional whose stationary values will coincide with the eigenvalues of (I.6) when operator $R(f)$ is represented in a complete operator basis set. However, the corresponding ω's do not provide upper bounds of the exact energy differences, even when a Hermitian operator (i.e., the bare Hamiltonian H) is used in Eq. (I.7), and the de-excitation operator is a Hermitian conjugate of the excitation operator (in this case the corresponding total energies are upper bounds of the exact total energies given that a linear parameterization of the excitation operator $R(f)$ is used [71]).

Alternatively, one can consider functionals based on the so-called commutator metric [154, 155, 164]:

$$\omega_{0f} = \frac{< \tilde{0}|[L(f), [\bar{H}, R(f)]]_{\pm}|\tilde{0} >}{< \tilde{0}|[L(f), R(f)]_{\pm}|\tilde{0} >} \tag{I.8}$$

[2] In the case of a Hermitian $\bar{H}$, $L(f)$ is simply the adjoint of $R(f)$: $L(f) = R(f)^{+}$. In the general case: $L(f)R(f') = \delta_{ff'}|0 >< 0|$.

All three functionals yield identical results in the complete operator basis set limit, or when the so-called killer condition is satisfied [164]:

$$L(f)|\tilde{0}>=0 \tag{I.9}$$

The killer condition means that the reference state $|\tilde{0}>$ cannot be de-excited (i.e., that the reference can be regarded as a vacuum). Alternatively, (I.9) can be interpreted as orthogonality of the reference and final states:

$$L(f)|\tilde{0}>=|0><f|\tilde{0}>=0 \tag{I.10}$$

Note that the killer condition (I.10) is satisfied when the exact initial state is used as the reference and the operator basis is complete w.r.t. the final states. Another simple case when the killer condition is easily satisfied is when the single Slater determinant is used as the reference $|\tilde{0}>$, and the operator L is pure de-excitation operators w.r.t. the reference $|\tilde{0}>$ (i.e., does not annihilate electrons from the occupied orbitals and does not create electrons in the virtual orbitals). For an excellent presentation of the different derivations of the EOM equations, and the role of the killer condition, see the recent work of Surján and coworkers [240].

One of the disturbing consequences of the violation of killer condition is that functionals (I.7) and (I.8) become non-equivalent. Indeed, which of the three functionals should be employed in the derivation of working equations? All of them give

the exact result in the limit of the complete operator basis set, however, the choice between them in the case of an approximate theory is rather arbitrary.

At this point, we depart from the textbook EOM presentation [164]. Instead of general excitation operators $R(f), L^+(f)$ which generate the *exact* final state $|f>$ when acting on *any* reference state provided that $<0|\tilde{0}> \neq 0$, we introduce less general operators $\tilde{R}(f), \tilde{L}^+(f)$ defined w.r.t. the specific reference $|\tilde{0}>$:

$$\tilde{R}(f) = |f><\tilde{0}|$$
$$\tilde{L}(f) = |\tilde{0}><f| \qquad \text{(I.11)}$$

Unlike $R(f)$, $\tilde{R}(f)$ will not yield the exact final state when acting on a state $|g>$ with non-zero overlap with $|0>$ if $<\tilde{0}|g>=0$: $\tilde{R}(f)|g>=|f><\tilde{0}|g>=0$. Because commutator equation (I.6) is no longer valid for $\tilde{R}$ (unless, of course, the reference $|\tilde{0}>$ happens to be the exact eigenstate $|0>$), functionals (I.7) and (I.8) will not yield the exact ω_{0f} even when the operators $\tilde{R}(f), \tilde{L}^+(f)$ are expanded over the complete basis. However, the *difference* between the resulting ω_{0f} and the exact one assumes the same constant value for all the target states $|f>$. [3] *Therefore,*

[3]The operator $\tilde{R}(f)$ is no longer an eigen-operator of the super-operator $\bar{H}$:

$$[\bar{H}, \tilde{R}(f)]\tilde{0} >= E_f \tilde{R}(f)|\tilde{0}> - |f> \sum_k E_k <\tilde{0}|k>^2,$$

where the sum runs over *all* eigenstates of $\bar{H}$. Consequently, the expectation value ω_{0f} from Eq. (I.7) becomes:

$$\omega_{0f} =<\tilde{0}|L(f)[\bar{H}, \tilde{R}(f)]|\tilde{0}>= E_f - \sum_k E_k <\tilde{0}|k>^2$$

Note that the second term in the r.h.s. of the above equation depends only upon the reference, and is therefore the same for all the target states $|f>$. Therefore, for an arbitrary reference $|\tilde{0}>$, the exact

for an arbitrary reference $|\tilde{0}>$, the exact energy gap between any two target states $|f>$ and $|i>$ will be retrieved from functionals (I.7) and (I.8) in the limit when the operators $\tilde{R}(f), \tilde{L}^{+}(f)$ are expanded over the complete basis.

In practice, excitation and de-excitation operators are expanded over a finite basis set. In the case of a linear parameterization, it is convenient to expand the excitation and de-excitation operators over a set of operators ρ_k and λ_k:

$$\tilde{R}(f) = \sum_k r_k^f \rho_k \tag{I.12}$$

$$\tilde{L}(f) = \sum_k l_k^f \lambda_k \tag{I.13}$$

When acting on the reference $|\tilde{0}>$, these operators generate a biorthogonal set of basis functions:

$$\rho_k|\tilde{0}> = |\tilde{k}> \tag{I.14}$$

$$<\tilde{0}|\lambda_l = <\tilde{l}| \tag{I.15}$$

$$<\tilde{l}|\tilde{k}> = \delta_{lk}, \quad <\tilde{k}| \neq (|\tilde{k}>)^{+} \tag{I.16}$$

The completeness of the operator basis set $\{\rho_k, \lambda_l\}$ is derived from the completeness of the Hilbert space $\{|\tilde{k}>, <\tilde{l}|\}$. Note that only the completeness w.r.t. the target

energy gap between any two target states $|f>$ and $|i>$ will be retrieved from functionals (I.7) and (I.8) in the limit when the operators $\tilde{R}(f), \tilde{L}^{+}(f)$ are expanded over the complete basis:

$$\omega_{if} = \omega_{0f} - \omega_{0i} = E_f - E_i$$

states $|f>$ is required for the EOM functionals to yield the exact energy differences between the target states, while the Hilbert space can be incomplete w.r.t. other groups of egenstates, provided that the target states are not interacting across the Hamiltonian with these groups (e.g., states of different point-group or spin symmetry, or with different number of electrons).

It is convenient (although not necessary) to choose operators ρ_k, λ_k to be of rank one:

$$\rho_k = |\tilde{k}><\tilde{0}|$$
$$\lambda_k = |\tilde{0}><\tilde{l}| \tag{I.17}$$

By considering the first variation of functional (I.7) w.r.t. right $\tilde{R}$ and left $\tilde{L}$ vectors, and by assuming that variations $\delta\tilde{R}$ and $\delta\tilde{L}$ are independent (see Appendix II; see also Ref. [155] for the discussion of bivariational principle, an extension of variational principle to the case of non-Hermitian Hamiltonians), we arrive at a non-Hermitian secular problem for the expansion coefficients $\{r_k\}$ and $\{l_k\}$:

$$(\bar{\boldsymbol{H}} - E_0)\boldsymbol{R} = \boldsymbol{R\Omega} \tag{I.18}$$
$$\boldsymbol{L}(\bar{\boldsymbol{H}} - E_0) = \boldsymbol{\Omega L} \tag{I.19}$$
$$E_0 =<\tilde{0}|\bar{H}|\tilde{0}>, \tag{I.20}$$

where matrices $\boldsymbol{R}$ and $\boldsymbol{L}$ are constructed from the expansion coefficients (I.12) and (I.13), e.g., $\boldsymbol{R}_{if} = r_i^f$; diagonal matrix $\boldsymbol{\Omega}$ contains the transition energies: $\boldsymbol{\Omega}_{kk} = \omega_{0k}$; and $\bar{\boldsymbol{H}}$ is the matrix of the Hamiltonian operator $\bar{H}$ in the basis of (I.14) and (I.15): $\bar{\boldsymbol{H}}_{lk} = < \tilde{l}|\bar{H}|\tilde{k} >$.

At this point, we can discuss choices of the reference $|\tilde{0} >$, the Hamiltonian $\bar{H}$, and the operator basis ρ_k, λ_k. The first applications of the EOM formalism used the bare Hamiltonian H, and employed correlated (e.g., multi-reference) wave functions as the reference state $|\tilde{0} >$ [161, 201]. By analogy, the first applications of the EOM formalism to the CC models also used the bare Hamiltonian (e.g., see Ref. [214] and references therein), and the CC wave function [43, 44] as the reference $|\tilde{0} >$. In this approach, the killer condition (I.9) is not satisfied. Moreover, a straightforward application of functional (I.7) *does not yield* EOM-CC equations even if one replaces the bra reference by $< \Phi_0|exp(-T)$ as opposed to $< \Phi_0|exp(T^+)$. That is why a projective approach has been traditionally used to derive the EOM equations [67,214, 230], although variational properties of the EOM-CC theory have been recognized [47, 230].

Alternatively, in a single-reference coupled-cluster EOM theory, one can consider a single Slater determinant $|\Phi_0 >$ as the reference state $|\tilde{0} >$ which greatly simplifies the choice of the excitation operators $\tilde{R}, \tilde{L}^+$, and easily satisfies the killer condition (I.9).

Correlation effects are folded in $\bar{H}$ through the similarity transformation: [4]

$$\bar{H} \equiv e^{-T} H e^{T} \tag{I.21}$$

$$T = T_1 + \ldots + T_n \tag{I.22}$$

where T_μ are μ-fold excitations from $|\Phi_0>$,

$$\begin{aligned} T_1 &= \sum_{ia} t_i^a a^+ i \\ T_2 &= \frac{1}{4} \sum_{ijab} t_{ij}^{ab} a^+ b^+ j i \\ &\ldots \end{aligned} \tag{I.23}$$

The reference determinant $|\Phi_0>$ defines a separation of the orbital space into a subspace of orbitals occupied in $|\Phi_0>$ and a complementary subspace of virtual orbitals. We will adhere to the convention when indexes $i, j, k, \ldots$ are reserved for the orbitals occupied in the reference determinant $|\Phi_0>$, indexes $a, b, c, \ldots$ — to

[4] If the bare Hamiltonian H and the single-determinantal reference is used in Eq. (I.7), familiar CI equations are recovered. For example, by truncating the excitation operators up to double excitations, transition energies are found by the diagonalization of the bare Hamiltonian matrix in the basis of the reference, and the singly and doubly excited determinants. Thus, EOM-CC and CI methods are very similar both conceptually and technically. Technically, Davidson iterative diagonalization procedure for the Hermitian matrices [54] should be appropriately modified [103, 197] for the case of non-Hermitian matrices ($\bar{H}$ in the EOM-CC theory). The computational cost of the diagonalization step is approximately the same for the CI and CC models truncated at the same level of excitation (e.g., N^6 for the CISD and the CCSD models). Practically, however, the truncated EOM-CC model is superior to the CI truncated at the same level because effects of higher excitations are "folded in" through the similarity transformation (I.21) into the effective Hamiltonian $\bar{H}$. The role of the similarity transformation is to achieve more compact representation of vectors $\tilde{R}, \tilde{L}$. For example, if T is not truncated and is a solution of CC equations in a full multi-electron space, the reference determinant $|\tilde{0}>$ is an eigenstate of $\bar{H}$ with the exact eigenvalue.

unoccupied orbitals, and $p, q, r, s, \ldots$ are used in a general case, i.e., when an orbital can be either occupied or virtual. Then excitation and de-excitation operators can be represented as:

$$\tilde{R} = R_0 + R_1 + \ldots + R_n$$

$$\tilde{L} = L_0 + L_1 + \ldots + L_n$$

where n is the highest excitation level, $R_0 = r_0\hat{1}$, and the form of R_k and L_k (as well as a definition of the excitation level k) depend upon the nature of the reference and final states. For example, when both the reference and the final state are states of the N-electron system, operators R_k conserve the number of electrons:

$$R_1^{EE} = \sum_{ia} r_i^a a^+ i$$
$$L_1^{EE} = \sum_{ia} l_i^a i^+ a$$

When the reference and the final state differ by number of electrons, operators R_k/L_k^+ are ionizing or electron-attaching:

$$R_1^{IP} = \sum_i r_i i$$
$$R_1^{EA} = \sum_a r_a a^+$$
$$\dots$$
$$R_1^{DIP} = \sum_{ij} r_{ij} ji$$
$$R_1^{DEA} = \sum_{ab} r_{ab} a^+ b^+$$
$$\dots$$

Regardless the nature of T, similarity transformation does not change the eigenvalues of the Hamiltonian [5] — therefore stationary values of functionals (I.7)-(I.8) yield exact energy differences between the target states when the excitation operators $\tilde{R}, \tilde{L}^+$ are expanded over the complete operator basis set. However, the exact ω_{0f} can only be obtained when both the operator set is complete and $|\tilde{0}> \equiv |0>$. The latter

[5] Let $|\Phi_i>$, $0 = 1, 2, \dots$, be a complete set of determinants, generated by excitations from the reference $|\Phi_0>$. Obviously, the eigenfunctions $|\Psi_k>$, $k = 0, 2, \dots$, of the bare Hamiltonian $\hat{H}$ can be written as linear combinations of $|\Phi_i>$:

$$\hat{H}|\Psi_k> = E_k|\Psi_k>,$$
$$|\Psi_k> = \sum_i C_{ki}|\Phi_i>$$

By inserting $\hat{1} = e^T e^{-T}$ before $|\Phi_i>$ in the above equations, and then multiplying the Schrödinger equation by e^{-T}, it is easy to see that:

$$\bar{H} \sum_i C_{ki} e^{-T}|\Phi_i> = E_k \sum_i C_{ki} e^{-T}|\Phi_i>$$

i.e., $\bar{H}$ has the same set of eigenvalues as $\hat{H}$, but different eigenvectors.

can be achieved by an appropriate choice of T from the similarity transformation, i.e., when T is not truncated and satisfies the CC equations for the reference $|\tilde{0}>$, the single determinant $|\tilde{0}>$ becomes an eigenstate of $\bar{H}$.

Even in the case of the exact $\tilde{R}, \tilde{L}^{+}$ and $\tilde{0}>$, the corresponding left and right eigenvectors of $\bar{H}$ are not Hermitian conjugates. Eigenstates of the bare Hamiltonian H can be obtained from the eigenstates of $\bar{H}$ as follows:

$$< \Psi| =< \Phi_0|e^{-T}\tilde{L}|\Psi >= \tilde{R}e^{T}|\Phi_0 >$$

In the EOM-CC approach, amplitudes T are defined by the coupled-cluster equations [43, 44, 192] for the reference state:

$$E^{CC} =< \Phi_0|\bar{H}|\Phi_0 > \tag{I.24}$$

$$< \Phi_\mu|\bar{H} - E^{CC}|\Phi_0 >= 0 \tag{I.25}$$

$$\tag{I.26}$$

In the above equations and further on, E^{CC} is the total coupled-cluster energy for the reference state, $\hat{\mu}$ is an excitation operator, Φ_μ denotes all μ-tuple excited determinants, e.g., $\Phi_1 = \{\Phi_i^a\}$, $\Phi_2 = \{\Phi_{ij}^{ab}\}$, etc., and the so called projective equations (I.25) define amplitudes of the cluster operators T_μ. Usually [140, 214, 230] but not necessarily [105], the cluster operator T is truncated at the same level as the EOM operators $\tilde{R}$ and $\tilde{L}^{+}$. When this is the case, or when T is truncated at the higher

excitation level than $\tilde{R}$, the reference determinant $|\Phi_0>$ is an eigenstate of $\bar{H}$ in the subspace of up to n-tuple excited determinants, the corresponding eigenvalue being E^{CC} from Eq. (I.24). This shows that the EOM-CC representation of the target states is more compact than the configuration interaction (CI) representation due to the explicit separation of correlation effects in the reference and target states.

I.2 Choice of the reference state

A subtle issue for discussion is the choice of the reference state $|\tilde{0}>$. Formally, any reference state can be used in Eqns. (I.6)-(I.8) without affecting the ability of the theory to converge to the exact answer (for the energy differences between the target states). However, as can be seen from Eqns. (I.14)-(I.15), the operator basis sets $\{\rho_k\}$ and $\{\lambda_k\}$ are defined w.r.t. the reference state. The quality of the operator basis set can be judged by the quality of the basis of many-electron basis functions generated by the basis operators from the reference [see Eqns. (I.14)-(I.15)]. Therefore, the choice of the reference is directly related to the choice of the operator basis: *for different references, the same ansatz for the excitation operators (see previous section) would result in a different set of many-electron basis functions*. Thus, one can consider the reference as one of the model's parameters subject for optimization. Unlike many state-by-state approaches where the reference is chosen such that it serves as the best zero-order wave function for the state of interest, the optimal reference in EOM is the one which results in the most balanced description of the EOM target

states. Moreover, when one is interested in a single target state (e.g., the ground state of a molecule), the optimal reference is not necessarily the one which has the largest overlap with the target state's wave function, but rather the one producing a more flexible and balanced set of many-electron basis functions.

Fig. I.1 illustrates how different references can provide a balanced description of different target states. One of the most popular applications of the EOM-CC theory is

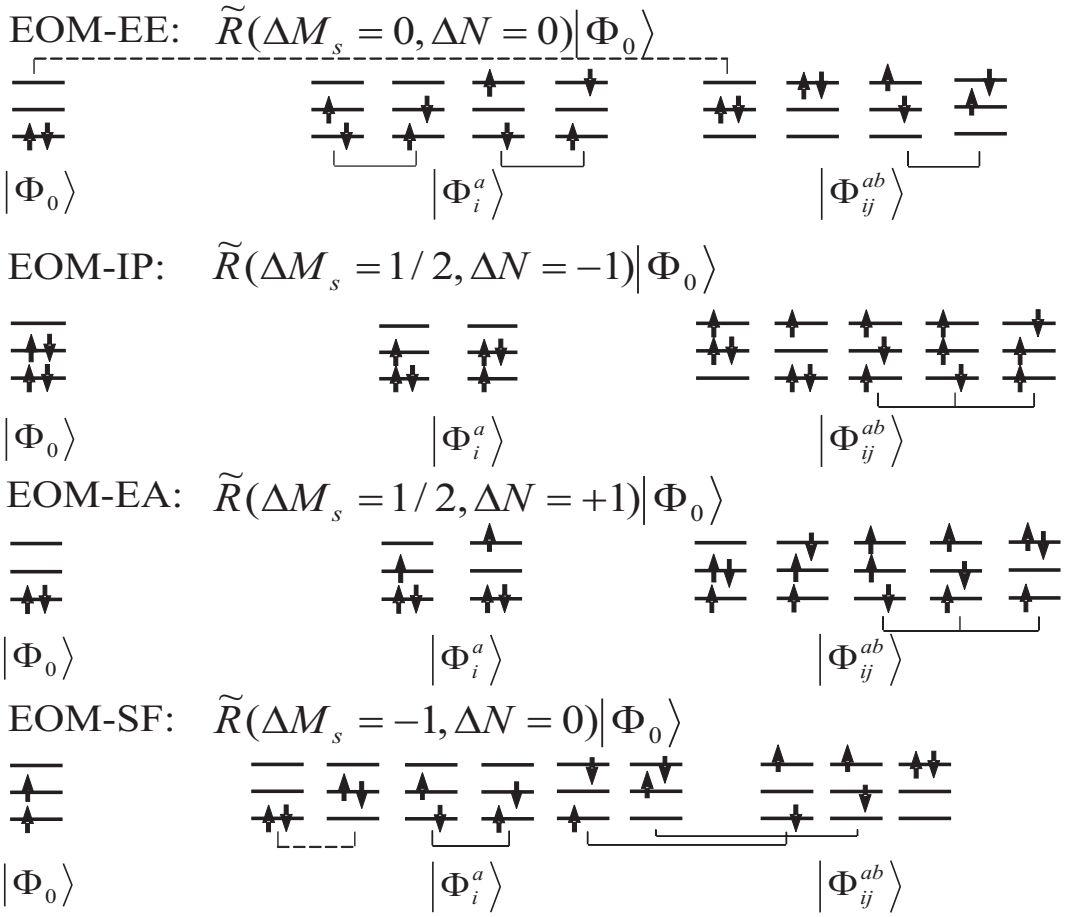

Figure I.1: Sets of determinants generated from different reference determinants. In each set, determinants required to construct spin-eigenfunctions are connected by thin solid lines. Determinants contributing to a diradical's eigenfunction with large weights are connected by dashed lines. The imbalance occurs when the connected determinants are generated by different levels of excitation.

for calculating electronic excitation energies (EOM-EE) [47, 85, 131, 132, 140, 230]. The optimal reference for EOM-EE is often the closed-shell ground state Hartree-Fock determinant, and operators $\tilde{R}$ and $\tilde{L}$ conserve the number of α and β electrons:

$$\begin{aligned} R_1^{EE} &= \sum_{ia} r_i^a a^+ i \\ L_1^{EE} &= \sum_{ia} l_i^a i^+ a \\ &\dots \end{aligned} \tag{I.27}$$

Note that open-shell excited states whose zero-order description requires two-determinantal wave functions are well described by single-reference EOM models [18]. Identical equations can be derived within the linear response formalism [124, 175, 178, 198, 214]. The EOM-EE-CC excitation energies become exact when both the EOM operators $\tilde{R}, \tilde{L}$ and the operator T from the similarity transformation include up to n-tuple excitations, and T satisfies CC equations (I.25). Interestingly enough, accurate values of the excitation energies can be obtained with *different* truncation levels in $\tilde{R}, \tilde{L}$ and T, with higher excitations being more important in the EOM part [105, 224].

More general excitations can change the number of electrons in the system. In order to calculate transition energies of such processes (i.e. ionization potentials or electron affinities), the EOM-IP or EOM-EA methods can be used [182, 231]. The reference states for EOM-IP/EA are determinants for $N+1/N-1$ electron states, whereas the final states are N-electron ones. Another class of less obvious but very

successful applications of the EOM-IP/EA methods is not concerned with electron ionization or attachment processes, but rather targets ground and excited states of problematic neutral systems. In these applications, an $N-1$ or $N+1$ electron reference state is used in order to generate a balanced set of configurations needed for a target N-electron system. For example, to avoid the troublesome symmetry breaking in doublet radicals (or to obtain spin-pure wave functions), EOM-IP/EA methods have been successfully applied [122,231]. In these models, the reference determinant is chosen to represent a *closed-shell* cation or anion, and the EOM operators $\tilde{R}$ and $\tilde{L}$ do not conserve the number of electrons [182, 218, 231]:

$$\begin{aligned} R_1^{IP} &= \sum_i r_i i \\ R_1^{EA} &= \sum_a r_a a^+ \\ &\dots \end{aligned} \tag{I.28}$$

While EOM-IP/EA-CC yield the exact IP/EA only under the same conditions as EOM-EE-CC, the exact description of the target (ionized or attached) states can be achieved with only the EOM operators being expanded over the complete basis. For example, the EOM-IP-CC description of the lithium atom will be exact even with $T=0$, provided that $\tilde{R}, \tilde{L}^+$ include up to triple electron excitations, e.g.:

$$\tilde{R}^{IP} = \sum_i r_i i + \sum_{ija} r_{ij}^a a^+ ij + \frac{1}{4}\sum_{ijkab} r_{ijk}^{ab} a^+ b^+ jik + \frac{1}{6}\sum_{ijklabc} r_{ijkl}^{abc} a^+ b^+ c^+ kjil \tag{I.29}$$

Doubly-ionized/attached EOM models which target diradicals have also been presented [253]:

$$R_1^{DIP} = \sum_{ij} r_{ij} ji$$
$$R_1^{DEA} = \sum_{ab} r_{ab} a^+ b^+$$
$$\ldots \qquad \text{(I.30)}$$

Similar approaches have been used in conjunction with propagator techniques [38, 152, 168, 169, 184].

Lastly, in cases where target states are multi-configurational due to orbital degeneracies, a high-spin reference state can be chosen. To obtain target low-spin states, the EOM operators $\tilde{R}$ and $\tilde{L}$ should include spin-flip (EOM-SF models) [134–136, 210, 210, 216]. So far, models based on a high-spin triplet and quartet references have been implemented and benchmarked [134–136,210,210,216,221–223], however, extensions of the SF approach to the higher spin references are also very promising. An attractive feature of the triplet and quartet reference based EOM-SF models is that only a single spin-flip is required to obtain target M_s=0/M_s=$\frac{1}{2}$ states. That is why the corresponding EOM-SF equations in a spin-orbital form are identical to those of the non-SF EOM theories. The following SF models have been implemented and benchmarked [134–136, 210, 216, 221–223]: (i) the SF models based on the Hartree-Fock reference wave function, i.e., SF configuration interaction singles

(SF-CIS), spin-complete SF-CIS, and SF-CI model with single and double substitutions (SF-CISD); (ii) the perturbatively corrected SF-CIS model, SF-CIS(D); (iii) the SF optimized orbitals CCD model (SF-OOCCD, or EOM-OD). The SF variant of density functional theory was also developed [216]. We introduced the EOM-SF-CCSD model [147]. As in the non-SF ground [217] and excited [139] states variants, EOM-CCSD performs very similarly to EOM-OD. Computationally, however, EOM-CCSD is more efficient since it does not involve integral transformation at each CC iteration.

I.3 EOM-SF-CCSD model

This work considers EOM-CCSD models in which T, $\tilde{R}$ and $\tilde{L}^+$ are truncated to the single and double excitations, and operators $\tilde{R}$ and $\tilde{L}^+$ conserve the total number of electrons in the system. Thus, the transformed Hamiltonian (I.21) is diagonalized in the subspace of the reference determinant (O), and the determinants generated by single (S) and double (D) electron excitations from the reference. Relative to the reference, all possible singly excited determinants can be divided into the three groups: (i) those which are generated by the $\alpha \rightarrow \alpha$ and $\beta \rightarrow \beta$ excitations, and thus having the same number of α and β electrons as the reference, i.e. (N_α, N_β); (ii) those which are generated by the $\alpha \rightarrow \beta$ excitations — these have one α-electron less and one β-electron more than the reference, i.e. $(N_\alpha - 1, N_\beta + 1)$; (iii) those which are generated by the $\beta \rightarrow \alpha$ excitations — these have one β-electron less and

one α-electron more than the reference, i.e. ($N_\alpha+1, N_\beta-1$). Likewise, one can split the R_1 operator into the three components: M_s=0, M_s=-1, and M_s=+1, respectively. In a similar fashion, doubly excited determinants (and, respectively, the R_2 operator) can be divided into the following groups: (N_α, N_β)/M_s=0, ($N_\alpha-1, N_\beta+1$)/M_s=-1, ($N_\alpha+1, N_\beta-1$)/M_s=+1, ($N_\alpha-2, N_\beta+2$)/M_s=-2, ($N_\alpha+2, N_\beta-2$)/M_s=+2. The M_s of the corresponding determinants is defined by the M_s of the excitation operator $\tilde{R}$ and the M_s of the reference determinant and is simply their sum. For example, when the $M_s = 0$ reference is used, the M_s of the excitation operator $\tilde{R}$ is equal to the M_s of the determinants generated by $\tilde{R}$ acting on the reference.

Since the non-relativistic Hamiltonian H does not include spin, the matrix of $\bar{H}$ is block-diagonal in the basis of the so generated determinants. Therefore, one can diagonalize each M_s block of $\bar{H}$ independently. In the traditional implementation of EOM-CCSD, only the M_s=0 block is diagonalized, which yields singlets and M_s=0 components of triplet states in the case of a singlet reference state. For doublet M_s=$\frac{1}{2}$ references, the M_s=0 part of R generates M_s=$\frac{1}{2}$ determinants. This procedure yields doublets and low-spin components of quartet states.

In the SF variant of EOM-CCSD, we consider spin-flipping (e.g., $M_s = 1$ or $M_s = -1$) parts of $\tilde{R}$. In the case of a singlet reference, the diagonalization of the $M_s = \pm 1$ blocks yields $M_s = \pm 1$ components of triplet states, which are exactly

degenerate with the M_s=0 counterparts calculated by the traditional approach outlined above. [6] However, when the high spin $M_s = 1$ triplet reference is used, the M_s=-1 excitations yield the M_s=0 determinants. Therefore, the diagonalization of $\bar{H}$ produces M_s=0 final states (both singlets and triplets).

In the basis of the reference, and the singly and doubly excited determinants, $\bar{H}$ assumes the following form:

$$\bar{H} = \begin{pmatrix} E^{CC} & \bar{H}_{OS} & \bar{H}_{OD} \\ 0 & \bar{H}_{SS} & \bar{H}_{SD} \\ 0 & \bar{H}_{DS} & \bar{H}_{DD} \end{pmatrix}, \tag{I.31}$$

where E^{CC} is the reference CC energy from Eq. (I.24), and $\bar{H}_{SO} = \bar{H}_{DO} = 0$ due to Eq. (I.25). It immediately follows from Eq. (I.31) that: (i) the reference CCSD wave function is an eigenvector of $\bar{H}$ with $R_0 = \hat{1}$ and $R_1 = R_2 = 0$, the corresponding eigenvalue being E^{CC}; (ii) the reference state left eigenvector has $L_0 = \hat{1}$, and all other left eigenvectors have $L_0 = 0$ due to the biorthogonality condition. Since right eigenvectors do not form an orthonormal set, the reference can be also present in final EOM states (i.e, $R_0 = r_0\hat{1}$, $r_0 \neq 0$). However, excitation energies can be calculated by diagonalizing $\bar{H}$ in the basis of single and double excitations only [47]. Values

[6] This feature is not present in most of the available EOM-CCSD implementations. We found this type of calculations very helpful in testing the correctness of our implementation of the EOM-SF methods.

of the so calculated R_1 and R_2 define the weight of the reference determinant in the right EOM-CC eigenvector:

$$r_0 = \frac{1}{\omega}\left(\bar{H}_{OS}R_1 + \bar{H}_{OD}R_2\right) \tag{I.32}$$

Alternatively, r_0 can be calculated from the biorthogonality condition by using the reference state left eigenvector (a.k.a. the Z- or Λ- vector from the CC gradient theory):

$$r_0 = -(Z_1 \cdot R_1 + Z_2 \cdot R_2) \tag{I.33}$$

In the SF variant (when the reference and excited determinants have different number of α and β electrons), the reference is not present in final EOM states (i.e., $r_0 = 0$ for all the SF-EOM states). After subtracting the reference energy from $\bar{H}$, the EOM-CCSD left and right eigen-problem reads as follows:

$$\begin{pmatrix} \bar{H}_{SS} - E^{CC} & \bar{H}_{SD} \\ \bar{H}_{DS} & \bar{H}_{DD} - E^{CC} \end{pmatrix} \begin{pmatrix} R_1 \\ R_2 \end{pmatrix} = \omega \begin{pmatrix} R_1 \\ R_2 \end{pmatrix} \tag{I.34}$$

$$\begin{pmatrix} L_1 & L_2 \end{pmatrix} \begin{pmatrix} \bar{H}_{SS} - E^{CC} & \bar{H}_{SD} \\ \bar{H}_{DS} & \bar{H}_{DD} - E^{CC} \end{pmatrix} = \omega \begin{pmatrix} L_1 & L_2 \end{pmatrix} \tag{I.35}$$

where ω is the energy difference relative to the reference state: $\omega = E - E^{CC}$. We present working equations and discuss details of the implementation in the Appendix I.

Chapter II. EOM-CCSD analytic gradients.

The chapter is organized as follows: in Sec. II.1 we derive a general expression for the EOM-CC energy gradient in terms of fully relaxed density matrices, Secs. II.1.1 and II.1.2 present derivation of programmable expressions for amplitude and orbital response equations, respectively.

II.1 The analytic EOM-CCSD energy derivative and Lagrangian

As discussed in the previous chapter, the EOM-CC energy functional (I.7) can be written in the following form [147, 230]:

$$E = \frac{< \Psi_L|H|\Psi_R >}{< \Psi_L|\Psi_R >} = \frac{< \Phi_0 L|\bar{H}|R\Phi_0 >}{< \Phi_0 L|R\Phi_0 >} \tag{II.1}$$

For convenience, let us rewrite here the EOM-CC equations (I.18, I.19) in an equivalent form:

$$< \Phi_\mu | \bar{H} - E | R\Phi_0 >= 0 \tag{II.2}$$

$$< \Phi_0 L | \bar{H} - E | \Phi_\mu >= 0 \tag{II.3}$$

$$\mu = 1, 2, \ldots, n \tag{II.4}$$

$$< \Phi_0 L^I | R^J \Phi_0 >= \delta_{IJ} \tag{II.5}$$

Once again, in the present work we consider EOM-CC models in which the maximum excitation level is 2, and excitation operators R, L [same as operators $\tilde{R}$, $\tilde{L}$ from Eq. (I.11)] conserve the total number of electrons (EOM-EE-CCSD and EOM-SF-CCSD).

For a normalized Ψ_L, Ψ_R — see Eq. (II.5) — the EOM energy of Eq. (II.1) can conveniently be expressed by using symmetrized one- and two- particle density matrices:

$$E =< \Psi_L | H | \Psi_R >= \sum_{pq} h_{pq} \gamma'_{pq} + \frac{1}{4} \sum_{pqrs} < pq||rs > \Gamma'_{pqrs} \tag{II.6}$$

$$\gamma'_{pq} = \frac{1}{2} < \Psi_L | p^+ q + q^+ p | \Psi_R > \tag{II.7}$$

$$\Gamma'_{pqrs} = \frac{1}{2} < \Psi_L | p^+ q^+ sr + s^+ r^+ pq | \Psi_R > \tag{II.8}$$

The EOM-CCSD programmable expressions for different blocks of γ'_{pq} and Γ'_{pqrs} are presented in Table II.1.

Table II.1: Excited state's effective one- and two-electron density matrices defined by Eqns. (II.7,II.8)[a]. Intermediates are summarized in Table II.2.

$$\gamma'_{ij} = \tilde{\gamma}_{ij} + \delta_{ij}$$
$$\tilde{\gamma}_{ij} = \tfrac{1}{2}P_+(ij)(-\textstyle\sum_a l_i^a \tilde{\bar{r}}_{ja} - \tilde{l}_{ij} - \sum_a Y_{ia}^1 t_j^a)$$
$$\gamma'_{ia} = \tfrac{1}{2}[r_0 l_i^a + Y_{ia}^1 + \textstyle\sum_{jb} l_j^b(\tilde{\bar{r}}_{ij}^{ab} - \tilde{r}_{ib} t_j^a - \tilde{r}_{ja} t_i^b) + \sum_{jb} Y_{jb}^1 (t_{ij}^{ab} - t_j^a t_i^b)$$
$$- \textstyle\sum_k \tilde{\bar{l}}_{ki} r_k^a - \sum_c \tilde{\bar{l}}^{ca} r_i^c - \sum_j \tilde{l}_{ji} t_j^a - \sum_b \tilde{l}^{ba} t_i^b + t_i^a]$$
$$\gamma'_{ab} = \tfrac{1}{2}P_+(ab)(\textstyle\sum_i l_i^a \tilde{\bar{r}}_{ib} + \tilde{l}^{ab} + \sum_i Y_{ia}^1 t_i^b)$$
$$\Gamma'_{ijkl} = \tilde{\Gamma}_{ijkl} - \delta_{li}\delta_{kj} + \delta_{ki}\delta_{lj} - \delta_{li}\tilde{\gamma}_{jk} + \delta_{ki}\tilde{\gamma}_{jl} + \delta_{lj}\tilde{\gamma}_{ik} - \delta_{kj}\tilde{\gamma}_{il}$$
$$\tilde{\Gamma}_{ijkl} = \tfrac{1}{4}\textstyle\sum_{ab}(l_{kl}^{ab}\bar{r}_{ij}^{ab} + l_{ij}^{ab}\bar{r}_{kl}^{ab})$$
$$\Gamma'_{abcd} = \tfrac{1}{4}\textstyle\sum_{ij}(l_{ij}^{ab}\bar{r}_{ij}^{cd} + l_{ij}^{cd}\bar{r}_{ij}^{ab})$$
$$\Gamma'_{ijka} = \tilde{\Gamma}_{ijka} - \delta_{kj}\gamma_{ia} + \delta_{ki}\gamma_{ja}$$
$$\tilde{\Gamma}_{ijka} = \tfrac{1}{2}[\textstyle\sum_b l_{ij}^{ab}\tilde{\bar{r}}_{kb} + \sum_b l_k^b \bar{r}_{ij}^{ab} + \sum_b Y_{kb}^1 \tilde{t}_{ij}^{ab} + \tilde{l}_{kj} t_i^a - \tilde{l}_{ki} t_j^a - \tilde{\bar{l}}_{ki} r_j^a + \tilde{\bar{l}}_{kj} r_i^a$$
$$+ \textstyle\sum_{lbc} l_{kl}^{bc}(\tfrac{1}{2}\bar{r}_{ij}^{bc} t_l^a - t_i^b \tilde{r}_{jl}^{ac} + t_j^b \tilde{r}_{il}^{ac} + t_{jl}^{ab} r_i^c - t_{il}^{ab} r_j^c + \tfrac{1}{2}\tilde{t}_{ij}^{bc} r_l^a)]$$
$$\Gamma'_{ijab} = \tfrac{1}{2}[\tilde{t}_{ij}^{ab} + r_0 l_{ij}^{ab} - \textstyle\sum_{kc} l_k^c (r_k^b \tilde{t}_{ij}^{ac} - r_k^a \tilde{t}_{ij}^{bc})$$
$$- \textstyle\sum_{kc} l_k^c(-t_{ik}^{ac} r_j^b + t_{jk}^{ac} r_i^b + t_{ik}^{bc} r_j^a - t_{jk}^{bc} r_i^a + t_{ik}^{ab} r_j^c - t_{jk}^{ab} r_i^c$$
$$-\tilde{\bar{r}}_{jk}^{ab} t_i^c + \tilde{\bar{r}}_{ik}^{ab} t_j^c + \bar{r}_{ij}^{ac} t_k^b - \bar{r}_{ij}^{bc} t_k^a + t_i^b \tilde{\bar{r}}_{jk}^{ac} - t_j^b \tilde{\bar{r}}_{ik}^{ac} - t_i^a \tilde{\bar{r}}_{jk}^{bc} + t_j^a \tilde{\bar{r}}_{ik}^{bc})$$
$$+ \textstyle\sum_k (\tilde{\bar{l}}_{ki} \tilde{r}_{jk}^{ab} - \tilde{\bar{l}}_{kj} \tilde{r}_{ik}^{ab}) + \sum_c (\tilde{\bar{l}}^{ca} \tilde{r}_{ij}^{bc} - \tilde{\bar{l}}^{cb} \tilde{r}_{ij}^{ac})$$
$$- \textstyle\sum_{klcd} l_{kl}^{cd}(-\tfrac{1}{4} t_{ij}^{cd} \tilde{r}_{kl}^{ab} - t_{ik}^{ac} \tilde{r}_{jl}^{bd} + t_{jk}^{ac} \tilde{r}_{il}^{bd} + \tfrac{1}{2} t_{ij}^{ac} \tilde{r}_{kl}^{bd} + t_{ik}^{bc} \tilde{r}_{jl}^{ad} - t_{jk}^{bc} \tilde{r}_{il}^{ad} - \tfrac{1}{2} t_{ij}^{bc} \tilde{r}_{kl}^{ad}$$
$$-\tfrac{1}{4} t_{kl}^{ab} \tilde{r}_{ij}^{cd} + \tfrac{1}{2} t_{ik}^{ab} \tilde{r}_{jl}^{cd} - \tfrac{1}{2} t_{jk}^{ab} \tilde{r}_{il}^{cd} + t_k^b t_{il}^{ac} r_j^d - t_k^b t_{jl}^{ac} r_i^d - t_k^a t_{il}^{bc} r_j^d + t_k^a t_{jl}^{bc} r_i^d$$
$$-\tfrac{1}{2} t_k^b \tilde{t}_{ij}^{cd} r_l^a + \tfrac{1}{2} t_k^a \tilde{t}_{ij}^{cd} r_l^b + \tfrac{1}{2} t_i^c t_{kl}^{ab} r_j^d - \tfrac{1}{2} t_j^c t_{kl}^{ab} r_i^d + t_i^c t_{jk}^{bd} r_l^a - t_j^c t_{ik}^{bd} r_l^a - t_i^c t_{jk}^{ad} r_l^b$$
$$+ t_j^c t_{ik}^{ad} r_l^b - \tfrac{1}{2} t_k^b t_l^a \bar{r}_{ij}^{cd} + t_k^b t_i^c \tilde{\bar{r}}_{jl}^{ad} - t_k^b t_j^c \tilde{\bar{r}}_{il}^{ad} - t_k^a t_i^c \tilde{\bar{r}}_{jl}^{bd} + t_k^a t_j^c \tilde{\bar{r}}_{il}^{bd} + \tfrac{1}{2} t_i^c t_j^d \tilde{\bar{r}}_{kl}^{ab})]$$
$$+ \textstyle\sum_{kc} Y_{kc}^1(-t_k^b \tilde{t}_{ij}^{ac} + t_k^a \tilde{t}_{ij}^{bc} + t_i^c t_{jk}^{ab} - t_j^c t_{ik}^{ab} - t_i^b t_{jk}^{ac} + t_j^b t_{ik}^{ac} + t_i^a t_{jk}^{bc} - t_j^a t_{ik}^{bc})$$
$$+ \textstyle\sum_k [\tilde{\bar{l}}_{ki}(t_k^b r_j^a - t_k^a r_j^b - t_j^b r_k^a + t_j^a r_k^b + t_k^b t_j^a - t_k^a t_j^b)$$
$$+ \tilde{\bar{l}}_{kj}(t_k^a r_i^b - t_k^b r_i^a + t_i^b r_k^a - t_i^a r_k^b - t_k^b t_i^a + t_k^a t_i^b)]$$
$$+ \textstyle\sum_c [\tilde{\bar{l}}^{ca}(t_j^c r_i^b - t_i^c r_j^b + t_i^b r_j^c - t_j^b r_i^c + t_j^c t_i^b - t_i^c t_j^b)$$
$$+ \tilde{\bar{l}}^{cb}(t_i^c r_j^a - t_j^c r_i^a - t_i^a r_j^c + t_j^a r_i^c + t_i^c t_j^a - t_j^c t_i^a)]$$
$$\Gamma'_{iajb} = \tilde{\Gamma}_{iajb} + \delta_{ji}\gamma_{ab}$$
$$\tilde{\Gamma}_{iajb} = -\tfrac{1}{2}[l_i^b \tilde{\bar{r}}_{ja} + l_j^a \tilde{\bar{r}}_{ib} - (Y_{ja}^1 t_i^b + Y_{ib}^1 t_j^a)$$
$$+ \textstyle\sum_{kc} l_{jk}^{ac}(t_k^b \tilde{r}_{ic} + t_i^c \tilde{r}_{kb} - \tilde{\bar{r}}_{ik}^{bc}) + \sum_{kc} l_{ik}^{bc}(t_k^a \tilde{r}_{jc} + t_j^c \tilde{r}_{ka} - \tilde{\bar{r}}_{jk}^{ac})]$$
$$\Gamma'_{iabc} = \tfrac{1}{2}[\textstyle\sum_j l_{ij}^{bc}\tilde{\bar{r}}_{ja} + \sum_j l_j^a \bar{r}_{ij}^{bc} + \sum_j Y_{ja}^1 \tilde{t}_{ij}^{bc} - r_i^c \tilde{\bar{l}}^{ab} + r_i^b \tilde{\bar{l}}^{ac} - t_i^c \tilde{l}^{ab} + t_i^b \tilde{l}^{ac}$$
$$+ \textstyle\sum_{jkd} l_{jk}^{ad}(-t_{ij}^{bd} r_k^c + t_{ij}^{cd} r_k^b + \tfrac{1}{2} t_{jk}^{bc} r_i^d + t_j^c \tilde{\bar{r}}_{ik}^{bd} - t_j^b \tilde{\bar{r}}_{ik}^{cd} + \tfrac{1}{2} t_i^d \bar{r}_{jk}^{bc})]$$

Here it is assumed that left and right excited states are biorthogonalized such that $\sum_{ia} l_i^a r_i^a + \frac{1}{4}\sum_{ijab} l_{ij}^{ab} r_{ij}^{ab} = 1$, and the factor r_0 insures orthogonality of the right excited states to the left ground state. Excited left states do not mix with the reference, thus $l_0 = 0$.

As follows from the previous chapter, the EOM-CCSD energy depends upon the following set of parameters: $E = E(L, R, T, C)$ where $L, R,$ and T are described

above, and C is a molecular orbital matrix which defines the transformation from atomic orbitals $\{\chi_\mu\}$ to molecular orbitals $\{\phi_p\}$:

$$\phi_p = \sum_\mu C_{\mu i}\chi_\mu \tag{II.9}$$

Therefore the full energy derivative w.r.t. a perturbation ξ is:

$$\frac{dE}{d\xi} = \frac{\partial E}{\partial \xi} + \frac{\partial E}{\partial L}\frac{dL}{d\xi} + \frac{\partial E}{\partial R}\frac{dR}{d\xi} + \frac{\partial E}{\partial T}\frac{dT}{d\xi} + \frac{\partial E}{\partial C}\frac{dC}{d\xi}, \tag{II.10}$$

where the first term is a Hellmann-Feynman contribution that describes explicit ξ-dependence of the Hamiltonian:

$$\frac{\partial E}{\partial \xi} = \sum_{pq} h^\xi_{pq}\gamma'_{pq} + \frac{1}{4}\sum_{pqrs} < pq||rs >^\xi \Gamma'_{pqrs} \tag{II.11}$$

$$h^\xi_{pq} = \frac{\partial h_{pq}}{\partial \xi} = \sum_{\mu\nu} C_{\mu p} h^\xi_{\mu\nu} C_{\nu q} \tag{II.12}$$

$$h^\xi_{\mu\nu} =< \chi_\mu|\frac{\partial \hat{h}}{\partial \xi}|\chi_\nu > + < \frac{\partial \chi_\mu}{\partial \xi}|\hat{h}|\chi_\nu > + < \chi_\mu|\hat{h}|\frac{\partial \chi_\nu}{\partial \xi} > \tag{II.13}$$

$$< pq||rs >^\xi = \frac{\partial < pq||rs >}{\partial \xi} = \sum_{\mu\nu\lambda\sigma} C_{\mu p}C_{\nu q} < \mu\nu||\lambda\sigma >^\xi C_{\lambda r}C_{\sigma s} \tag{II.14}$$

$$\begin{aligned} < \chi_\mu\chi_\nu||\chi_\lambda\chi_\sigma >^\xi =& < \frac{\partial \chi_\mu}{\partial \xi}\chi_\nu||\chi_\lambda\chi_\sigma > + < \chi_\mu\frac{\partial \chi_\nu}{\partial \xi}||\chi_\lambda\chi_\sigma > + \\ & < \chi_\mu\chi_\nu||\frac{\partial \chi_\lambda}{\partial \xi}\chi_\sigma > + < \chi_\mu\chi_\nu||\chi_\lambda\frac{\partial \chi_\sigma}{\partial \xi} > \end{aligned} \tag{II.15}$$

Since the EOM energy is stationary w.r.t. R, L^+, the $\frac{\partial E}{\partial L}$ and $\frac{\partial E}{\partial R}$ terms are zero (see Appendix II). The evaluation of the so-called amplitude and orbital response

terms, $\frac{dT}{d\xi}$ and $\frac{dC}{d\xi}$, respectively, is straightforward but tedious [84, 229]. As outlined in the Introduction, it can be simplified by employing the Lagrangian approach [39, 81, 92, 97, 239]. If the UHF/RHF reference is used, the EOM-CC Lagrangian is:

$$\mathcal{L}(L,R,T,C,Z,\Lambda,\Omega) = \frac{<\Phi_0 L|\bar{H}|R\Phi_0>}{<\Phi_0 L|R\Phi_0>} + \sum_{\mu=1}^{n} z_\mu <\Phi_\mu|\bar{H}-E|\Phi_0> + \frac{1}{2}\sum_{pq}\lambda_{pq}(f_{pq}-\delta_{pq}) + \sum_{pq}\omega_{pq}(S_{pq}-\delta_{pq}), \quad \text{(II.16)}$$

where $Z \equiv \{z_\mu\}$, $\Lambda \equiv \{\lambda_{pq}\}$, and $\Omega \equiv \{\omega_{pq}\}$ are undetermined Lagrange multipliers, and f and S are the Fock and MO overlap matrices, respectively:

$$f_{pq} =< p|h|q> + \sum_j <pj||qj> \quad \text{(II.17)}$$

$$S_{pq} =<\phi_p|\phi_q> \quad \text{(II.18)}$$

The first term in Eq. (II.16) is simply the energy functional of Eq. (II.1) and, since other terms of Eq. (II.16) do not depend on the EOM-amplitudes R and L, the Lagrangian is stationary w.r.t. L and R:

$$\frac{\partial\mathcal{L}}{\partial L} = \frac{\partial\mathcal{L}}{\partial R} = 0 \quad \text{(II.19)}$$

The second, third, and forth terms in Eq. (II.16) are zero when the CC amplitude equations and the Hartree-Fock equations for the reference Φ_0 (i.e., orbital

equations) are satisfied, which renders the Lagrangian as stationary w.r.t. the corresponding Lagrange multipliers. Alternatively, the amplitude and orbital equations can be retrieved by requesting the Lagrangian to be stationary w.r.t. the corresponding Lagrange multipliers:

$$\frac{\partial \mathcal{L}}{\partial Z_\mu} =< \Phi_\mu | \bar{H} - E | \Phi_0 >= 0 \tag{II.20}$$

$$\frac{\partial \mathcal{L}}{\partial \lambda_{pq}} = f_{pq} - \delta_{pq} = 0 \tag{II.21}$$

$$\frac{\partial \mathcal{L}}{\partial \omega_{pq}} = S_{pq} - \delta_{pq} = 0 \tag{II.22}$$

The first equation above is simply Eq. (I.25), whereas the second and third are equivalent to the Hartree-Fock equations. If all orbitals are active in correlated calculations, the EOM-CC energy is invariant w.r.t. unitary transformations among occupied or among virtual orbitals, and λ_{ij} and λ_{ab} are therefore zero.

To make $\mathcal{L}$ stationary w.r.t. all the parameters, we *define* the undetermined Lagrange multipliers $\{Z, \Lambda, \Omega\}$ such that $\frac{\partial \mathcal{L}}{\partial T}$ and $\frac{\partial \mathcal{L}}{\partial C}$ are zero. Thus, the *full* derivative of $\mathcal{L}$ w.r.t. ξ becomes equal to the *partial* derivative:

$$\begin{aligned} \frac{dE}{d\xi} &= \frac{d\mathcal{L}(L^{opt}, R^{opt}, T^{opt}, C^{opt}, Z^{opt}, \Lambda^{opt}, \Omega^{opt})}{d\xi} \\ &= \frac{\partial \mathcal{L}(L^{opt}, R^{opt}, T^{opt}, C^{opt}, Z^{opt}, \Lambda^{opt}, \Omega^{opt})}{\partial \xi} \end{aligned} \tag{II.23}$$

where superscript opt specifies that all the parameters satisfy the equations that ensure that $\mathcal{L}$ is fully stationary w.r.t. all the parameters.

The Lagrangian derivative can be written as follows:

$$\frac{\partial \mathcal{L}(L,R,T,C,Z,\Lambda,\Omega)}{\partial \xi} =< \Phi_0 L e^{-T} | \frac{\partial H}{\partial \xi} | e^T R \Phi_0 >$$
$$+ < \Phi_0 Z e^{-T} | \frac{\partial H}{\partial \xi} | e^T \Phi_0 > + \frac{1}{2} \sum_{pq} \lambda_{pq} \frac{\partial f_{pq}}{\partial \xi} + \sum_{pq} \omega_{pq} \frac{\partial S_{pq}}{\partial \xi} =$$
$$\sum_{pq} h^{\xi}_{pq} \rho_{pq} + \frac{1}{4} \sum_{pqrs} < pq||rs >^{\xi} \Pi_{pqrs} + \sum_{pq} \omega_{pq} S^{\xi}_{pq}, \qquad \text{(II.24)}$$

where h^{ξ}_{pq} and $< pq||rs >^{\xi}$ are defined by Eqns. (II.12-II.15) and S^{ξ}_{pq} is:

$$S^{\xi}_{pq} = \sum_{\mu\nu} C_{\mu p} C_{\nu q} \left(< \frac{\partial \chi_\mu}{\partial \xi} | \chi_\nu > + < \chi_\mu | \frac{\partial \chi_\nu}{\partial \xi} > \right) \qquad \text{(II.25)}$$

and effective density matrices ρ and Π are:

$$\rho = \gamma' + \gamma'' + \gamma''' \qquad \text{(II.26)}$$

$$\Pi = \Gamma' + \Gamma'' + \Gamma''', \qquad \text{(II.27)}$$

where γ' and Γ' are the so-called non-relaxed density matrices defined by Eqns. (II.7,II.8), γ'' and Γ'' are the amplitude response contributions:

$$\gamma''_{pq} = \frac{1}{2} < \Phi_0 Z e^{-T} | p^+ q + q^+ p | e^T \Phi_0 > \qquad \text{(II.28)}$$

$$\Gamma''_{pqrs} = \frac{1}{2} < \Phi_0 Z e^{-T} | p^+ q^+ sr + s^+ r^+ pq | e^T \Phi_0 > \qquad \text{(II.29)}$$

and γ''' and Γ''' are the orbital response contributions:

$$\gamma'''_{ij} = \frac{1}{2}\lambda_{ij} \tag{II.30}$$

$$\gamma'''_{ia} = \frac{1}{2}\lambda_{ia} \tag{II.31}$$

$$\gamma'''_{ab} = \frac{1}{2}\lambda_{ab} \tag{II.32}$$

$$\Gamma'''_{ijkl} = -\delta_{li}\tilde{\gamma}'''_{jk} + \delta_{ki}\tilde{\gamma}'''_{jl} + \delta_{lj}\tilde{\gamma}'''_{ik} - \delta_{kj}\tilde{\gamma}'''_{il} \tag{II.33}$$

$$\Gamma'''_{ijka} = -\delta_{kj}\gamma'''_{ia} + \delta_{ki}\gamma'''_{ja} \tag{II.34}$$

$$\Gamma'''_{iajb} = \delta_{ji}\gamma'''_{ab} \tag{II.35}$$

The programmable expressions for the amplitude response contributions γ''_{pq} and Γ''_{pqrs} can be retrieved from the expressions in Table II.1 by setting $r_0 = 1$, $r_i^a = 0$, $r_{ij}^{ab} = 0$, $l_i^a = z_i^a$, and $l_{ij}^{ab} = z_{ij}^{ab}$. When all occupied and/or virtual orbitals are active in correlated calculations, γ'''_{ij} and/or γ'''_{ab} are zero, respectively.

II.1.1 Amplitude response equations

The amplitude multipliers $\{Z\}$ are determined from the variational condition $\frac{\partial \mathcal{L}}{\partial T} = 0$:

$$\frac{\partial \mathcal{L}}{\partial T_\mu} = < \Phi_0 L|[\bar{H}, \hat{\mu}]|R\Phi_0 > + < \Phi_0 Z|[\bar{H}, \hat{\mu}]|\Phi_0 > = 0 \tag{II.36}$$

This is a non-homogeneous system of linear equations w.r.t. the $\{Z\}$ multipliers. It is convenient to rewrite Eq. (II.36) as [229]:

$$< \Phi_0 Z|\bar{H}|\Phi_\mu > - < \Phi_0 Z|\hat{\mu}\bar{H}|\Phi_0 >= - < \Phi_0 L|[\bar{H},\hat{\mu}]|R\Phi_0 >, \mu = 1,2,\ldots,n \tag{II.37}$$

By inserting the resolution of identity $\hat{1} = \sum_{\mu=0}^{N} \frac{1}{\mu!}|\Phi_\mu >< \Phi_\mu|$ between $\hat{\mu}$ and $\bar{H}$ in the left hand side (l.h.s.) of this equation, and using the reference state CC Eqns. (I.25), we arrive to:

$$< \Phi_0 Z|\bar{H} - E^{CC}|\Phi_\mu >= -\Xi_\mu \tag{II.38}$$

$$\Xi_\mu =< \Phi_0 L|[\bar{H},\hat{\mu}]|R\Phi_0 >, \mu = 1,2\ldots,n$$

The l.h.s. of this equation is identical to Eq. (II.3) for the left eigenstates of $\bar{H}$, upon the substitution of Z by L and E^{CC} by E. Thus, the code for the left EOM eigenstates can be reused for solving amplitude response equations.

In order to derive programmable expressions for the right hand side (r.h.s.) of Eq. (II.38), Ξ_μ [229], let us expand the commutator $[\bar{H},\hat{\mu}]$

$$< \Phi_0 L|[\bar{H},\hat{\mu}]|R\Phi_0 >=< \Phi_0 L|\bar{H}|R\Phi_\mu > - < \Phi_0 L|\hat{\mu}\bar{H}|R\Phi_0 > \tag{II.39}$$

and insert the resolution of identity between $\bar{H}$ and R in the first term, and between $\hat{\mu}$ and $\bar{H}$ in the second term. Using Eqns. (II.2,II.3), one can show that

$$< \Phi_0 L|[\bar{H}, \hat{\mu}]|R\Phi_0 >= \sum_{\nu=n+1}^{n+\mu} \frac{1}{\nu!} < \Phi_0 L|\bar{H}|\Phi_\nu >< \Phi_\nu|R\Phi_\mu > \qquad \text{(II.40)}$$

The above derivation applies both to the case of all orbitals being active in correlated calculations and to the case when some of the core and/or virtual orbitals are "frozen", i.e., when the CC and EOM excitation operators T, R, L^+ operate only in the space of active orbitals. In the latter case, the excited determinants in Eq. (II.37) belong to the active-active excitation subspace, while the resolution of identity includes all the determinants. However, only the determinants that do not involve excitations from the frozen core or into frozen virtuals survive in Eq. (II.40).

For EOM-CCSD ($n = 2$, $\mu = 1, 2$), the elements of Ξ_μ assume the following form:

$$\xi_i^a = \frac{1}{4} \sum_{jkbc} r_{jk}^{bc} < \Phi_0 L|\bar{H}|\Phi_{ijk}^{abc} >$$

$$\xi_{ij}^{ab} = \sum_{kc} r_k^c < \Phi_0 L\bar{H}|\Phi_{ijk}^{abc} > + \frac{1}{4} \sum_{klcd} r_{kl}^{cd} < \Phi_0 L\bar{H}|\Phi_{ijkl}^{abcd} >$$

and the programmable expressions are:

$$\xi_i^a = F_{ia}(1 - \sum_{jb} r_j^b l_j^b) - T_{ji}^3 l_j^a - T_{ba}^4 l_i^b + \sum_{jkbc} l_k^c r_{jk}^{bc} < ij||ab >$$
$$+\frac{1}{4} l_i^a \sum_{jkbc} r_{jk}^{bc} < jk||bc > -\frac{1}{2} \sum_b Y_{ab}^2 F_{ib} - \frac{1}{2} \sum_{bc} Y_{bc}^2 I_{ibca}^7$$
$$-\frac{1}{2} \sum_j Y_{ij}^3 F_{ja} + \frac{1}{2} \sum_{jk} Y_{jk}^3 I_{ikja}^6 - \frac{1}{2} \sum_{jb} l_{ij}^{ab} (\sum_{klc} r_{kl}^{bc} I_{kljc}^6 - \sum_{kcd} r_{kj}^{cd} I_{kbcd}^7)$$
$$+ \sum_{jb} Y_{iajb}^4 F_{jb} - \sum_{jkb} Y_{jakb}^4 I_{ikjb}^6 - \sum_{jbc} Y_{icjb}^4 I_{jcab}^7$$
$$+\frac{1}{4} \sum_{jkl} Y_{ijkl}^5 I_{lkja}^6 - \frac{1}{4} \sum_{bcd} Y_{abcd}^6 I_{ibcd}^7 \quad \text{(II.41)}$$

$$\xi_{ij}^{ab} =< ij||ab > +\omega r_0 l_{ij}^{ab} + Y_{ia}^1 F_{jb} - Y_{ja}^1 F_{ib} - Y_{ib}^1 F_{ja} + Y_{jb}^1 F_{ia}$$
$$+ \sum_c [(X_{ac}^1 + \frac{1}{2} Y_{ac}^2) < ij||bc > -(X_{bc}^1 + \frac{1}{2} Y_{bc}^2) < ij||ac >]$$
$$+ \sum_k [(X_{ik}^2 + \frac{1}{2} Y_{ik}^3) < jk||ab > -(X_{jk}^2 + \frac{1}{2} Y_{jk}^3) < ik||ab >]$$
$$+ \sum_{kc} r_k^c (l_i^a < jk||bc > -l_j^a < ik||bc > -l_i^b < jk||ac > +l_j^b < ik||ac >)$$
$$- \sum_k (l_{ik}^{ab} T_{kj}^3 - l_{jk}^{ab} T_{ki}^3) - \sum_c (l_{ij}^{ac} T_{cb}^4 - l_{ij}^{bc} T_{ca}^4) + \frac{1}{4} \sum_{kl} Y_{ijkl}^5 < kl||ab >$$
$$+\frac{1}{4} \sum_{cd} Y_{abcd}^6 < ij||cd > - \sum_{kc} r_k^c (l_{ik}^{ab} F_{jc} - l_{jk}^{ab} F_{ic})$$
$$- \sum_{kc} r_k^c (l_{ij}^{ac} F_{kb} - l_{ij}^{bc} F_{ka})$$
$$+ \sum_{klc} r_l^c (l_{kl}^{ab} I_{ijkc}^6 + l_{ik}^{ac} I_{jlkb}^6 - l_{jk}^{ac} I_{ilkb}^6 - l_{ik}^{bc} I_{jlka}^6 + l_{jk}^{bc} I_{ilka}^6$$
$$+ l_{jk}^{ab} I_{ilkc}^6 - l_{ik}^{ab} I_{jlkc}^6)$$
$$+ \sum_{kcd} r_k^d (l_{ij}^{cd} I_{kcab}^7 + l_{ik}^{ac} I_{jcbd}^7 - l_{jk}^{ac} I_{icbd}^7 - l_{ik}^{bc} I_{jcad}^7 + l_{jk}^{bc} I_{icad}^7$$
$$- l_{ij}^{ac} I_{kcbd}^7 + l_{ij}^{bc} I_{kcad}^7) + \sum_k (I_{ijka}^6 Y_{kb}^1 - I_{ijkb}^6 Y_{ka}^1) + \sum_c (Y_{jc}^1 I_{icab}^7 - Y_{ic}^1 I_{jcab}^7) \quad \text{(II.42)}$$

The expressions for the intermediates are summarized in Table II.2.

Table II.2: Intermediates used in Eqns. (II.41,II.42) and in the excited states' effective one- and two-particle density matrices defined by Eqns. (II.7,II.8).

$F_{ia} = f_{ia} + \sum_{jb} t_j^b < ij\|\|ab >$
$I^6_{ijka} =< ij\|\|ka > - \sum_c t_k^c < ij\|\|ac >$
$I^7_{iabc} =< ia\|\|bc > - \sum_j t_j^a < ij\|\|bc >$
$T^3_{ij} = \frac{1}{2}\sum_{kcd} r_{ik}^{cd} < jk\|\|cd >$
$T^4_{ab} = \frac{1}{2}\sum_{klc} r_{kl}^{ac} < kl\|\|bc >$
$X^1_{ab} = \sum_i l_i^a r_i^b$
$X^2_{ij} = \sum_a l_i^a r_j^a$
$Y^1_{ia} = \sum_{jb} l_{ij}^{ab} r_j^b$
$Y^2_{ab} = \sum_{ijc} l_{ij}^{ac} r_{ij}^{bc}$
$Y^3_{ij} = \sum_{kab} l_{ik}^{ab} r_{jk}^{ab}$
$Y^4_{iajb} = \sum_{kc} l_{ik}^{ac} r_{jk}^{bc}$
$Y^5_{ijkl} = \sum_{ab} l_{ij}^{ab} r_{kl}^{ab}$
$Y^6_{abcd} = \sum_{ij} l_{ij}^{ab} r_{ij}^{cd}$
$r_0 = \frac{1}{\omega}\left(\sum_{ia} r_i^a F_{ia} + \frac{1}{4}\sum_{ijab} r_{ij}^{ab} < ij\|\|ab >\right)$
$r_0 = -\sum_{ia} r_i^a z_i^a - \frac{1}{4}\sum_{ijab} r_{ij}^{ab} z_{ij}^{ab}$
$\tilde{r}_{ia} = r_i^a + \frac{1}{2} r_0 t_i^a$
$\tilde{\tilde{r}}_{ia} = r_i^a + r_0 t_i^a$
$Y^1_{ia} = \sum_{jb} l_{ij}^{ab} r_j^b$
$\tilde{r}_{ij}^{ab} = r_{ij}^{ab} + \frac{1}{2} r_0 t_{ij}^{ab}$
$\tilde{\tilde{r}}_{ij}^{ab} = r_{ij}^{ab} + r_0 t_{ij}^{ab}$
$\tilde{t}_{ij}^{ab} = t_{ij}^{ab} + t_i^a t_j^b - t_i^b t_j^a$
$\bar{r}_{ij}^{ab} = \tilde{\tilde{r}}_{ij}^{ab} + \tilde{r}_{ia} t_j^b - \tilde{r}_{ib} t_j^a - \tilde{r}_{ja} t_i^b + \tilde{r}_{jb} t_i^a$
$\tilde{l}_{ij} = \frac{1}{2}\sum_{kab} l_{ik}^{ab} \tilde{\tilde{r}}_{jk}^{ab}$
$\tilde{l}^{ab} = \frac{1}{2}\sum_{ijc} l_{ij}^{ac} \tilde{\tilde{r}}_{ij}^{bc}$
$\tilde{\tilde{l}}_{ij} = \frac{1}{2}\sum_{kab} l_{ik}^{ab} t_{jk}^{ab}$
$\tilde{\tilde{l}}^{ab} = \frac{1}{2}\sum_{ijc} l_{ij}^{ac} t_{ij}^{bc}$

Intermediates F_{ia}, I^6_{ijka}, and I^7_{iabc} depend only on T amplitudes and integrals, and are already employed in solving the EOM equations [147]. Other intermediates depend on the EOM amplitudes and therefore have to be recalculated for states of

interest. Similarly to the EOM amplitude equations, all the integrals and intermediates in the above equations are active-space in the case of the frozen core/virtuals.

II.1.2 Orbital response equations

The orbital response multipliers $\{\Lambda, \Omega\}$ are determined from a variational condition $\frac{\partial \mathcal{L}}{\partial C} = 0$. In order to avoid half-transformed integrals, it is convenient to transform the resulting set of equations back to the MO basis, that is, to replace the original set of equations:

$$\frac{\partial \mathcal{L}}{\partial C_{\mu p}} = 0 \tag{II.43}$$

by the following:

$$\sum_{\mu} C_{\mu u} \frac{\partial \mathcal{L}}{\partial C_{\mu p}} = 0 \tag{II.44}$$

In order to derive equations, it is convenient to rewrite the Lagrangian as follows:

$$\begin{aligned} \mathcal{L} = \sum_{pq} h_{pq}\gamma_{pq} + \frac{1}{4}\sum_{pqrs} < pq||rs > \Gamma_{pqrs} \\ + \frac{1}{2}\sum_{pq} \lambda_{pq} f_{pq} + \sum_{pq} \omega_{pq}(S_{pq} - \delta_{pq}) \end{aligned} \tag{II.45}$$

$$\gamma = \gamma' + \gamma'' \tag{II.46}$$

$$\Gamma = \Gamma' + \Gamma'' \tag{II.47}$$

The Lagrangian $\mathcal{L}$ depends on the C matrix elements through the one and two-electron integrals and the overlap matrix. After simple derivations (see Appendix II for more details) and assuming that the canonical Hartree-Fock orbitals are used

(i.e., $f_{pq} = \delta_{pq}\epsilon_p$), as well as employing the Hermitian properties of Ω and Λ, one arrives to the following set of equations:

$$0 = \sum_{\mu} C_{\mu i} \frac{\partial \mathcal{L}}{\partial C_{\mu j}} = 2\sum_{ip} h_{ip}\gamma_{jp} + \sum_{pqr} < ip||qr > \Gamma_{jpqr} + \epsilon_i \lambda_{ij} + \sum_{pq} < ip||jq > \lambda_{pq} + 2\omega_{ij} \quad \text{(II.48)}$$

$$0 = \sum_{\mu} C_{\mu a} \frac{\partial \mathcal{L}}{\partial C_{\mu i}} = 2\sum_{p} h_{ap}\gamma_{ip} + \sum_{pqr} < ap||qr > \Gamma_{ipqr} + \lambda_{ia}\epsilon_a + \sum_{pq} < ip||aq > \lambda_{pq} + 2\omega_{ia} \quad \text{(II.49)}$$

$$0 = \sum_{\mu} C_{\mu i} \frac{\partial \mathcal{L}}{\partial C_{\mu a}} = 2\sum_{p} h_{ip}\gamma_{ap} + \sum_{pqr} < ip||qr > \Gamma_{apqr} + \lambda_{ia}\epsilon_i + 2\omega_{ia} \quad \text{(II.50)}$$

$$0 = \sum_{\mu} C_{\mu a} \frac{\partial \mathcal{L}}{\partial C_{\mu b}} = 2\sum_{p} h_{ap}\gamma_{bp} + \sum_{pqr} < ap||qr > \Gamma_{bpqr} + \lambda_{ab}\epsilon_a + 2\omega_{ab} \quad \text{(II.51)}$$

By subtracting Eq. (II.50) from Eq. (II.49), we obtain the equation that determines the multipliers λ_{pq}:

$$0 = 2\sum_{p} (h_{ap}\gamma_{ip} - h_{ip}\gamma_{ap}) + \sum_{pqr} (< ap||qr > \Gamma_{ipqr} - < ip||qr > \Gamma_{apqr}) + \lambda_{ia}(\epsilon_a - \epsilon_i) + \sum_{pq} (< ip||aq > - < iq||pa >)\lambda_{pq} \quad \text{(II.52)}$$

It is convenient to uncouple the equations for λ_{ij} and λ_{ab} from the above equation for λ_{ia} by using the conditions below, which follow from the Hermitian structure of Ω:

$$\sum_{\mu} C_{\mu i} \frac{\partial \mathcal{L}}{\partial C_{\mu j}} - \sum_{\mu} C_{\mu j} \frac{\partial \mathcal{L}}{\partial C_{\mu i}} = 0 \tag{II.53}$$

$$\sum_{\mu} C_{\mu a} \frac{\partial \mathcal{L}}{\partial C_{\mu b}} - \sum_{\mu} C_{\mu b} \frac{\partial \mathcal{L}}{\partial C_{\mu a}} = 0 \tag{II.54}$$

which yields:

$$\begin{aligned} 0 &= 2 \sum_{p} (h_{ip}\gamma_{jp} - h_{jp}\gamma_{ip}) \\ &+ \sum_{pqr} (< ip||qr > \Gamma_{jpqr} - < jp||qr > \Gamma_{ipqr}) + \lambda_{ij}(\epsilon_i - \epsilon_j) \\ 0 &= 2 \sum_{p} (h_{ap}\gamma_{bp} - h_{bp}\gamma_{ap}) \\ &+ \sum_{pqr} (< ap||qr > \Gamma_{bpqr} - < bp||qr > \Gamma_{apqr}) + \lambda_{ab}(\epsilon_a - \epsilon_b) \end{aligned} \tag{II.55}$$

After Λ are determined, one can use Eqns. (II.48,II.50,II.51) to compute OO, OV, and VV blocks of Ω.

To obtain the final programmable form of the orbital response equations, we rewrite Eqns. (II.48,II.50,II.51,II.52,II.55) by breaking the density matrices to the

specific blocks, i.e. OO, OV, VV, etc., and by taking out the separable parts of OPDM and TPDMs from Table II.1:

$$
\begin{aligned}
0 = \lambda_{ia}(\epsilon_a - \epsilon_i) + \sum_{jk} < ik||ja > \lambda_{jk} + \sum_{bc} < ib||ac > \lambda_{bc} \\
+ \sum_{jb} \left(< ij||ab > - < ib||ja > \right) \lambda_{jb} + 2(\epsilon_a - \epsilon_i)\gamma_{ia} \\
-2\sum_{jk} < ik||ja > \tilde{\gamma}_{jk} - 2\sum_{jb} < ib||ja > \gamma_{jb} + 2\sum_{jb} < ij||ab > \gamma_{jb} \\
+2\sum_{bc} < ib||ac > \gamma_{bc} + \sum_{pqr} \Big(< ap||qr > \tilde{\Gamma}_{ipqr} - < ip||qr > \tilde{\Gamma}_{apqr} \Big)
\end{aligned}
\tag{II.56}
$$

$$
\begin{aligned}
0 = \lambda_{ij}(\epsilon_i - \epsilon_j) + 2\tilde{\gamma}_{ij}(\epsilon_i - \epsilon_j) \\
+ \sum_{pqr} \Big(< ip||qr > \tilde{\Gamma}_{jpqr} - < jp||qr > \tilde{\Gamma}_{ipqr} \Big)
\end{aligned}
\tag{II.57}
$$

$$
\begin{aligned}
0 = \lambda_{ab}(\epsilon_a - \epsilon_b) + 2\gamma_{ab}(\epsilon_a - \epsilon_b) \\
+ \sum_{pqr} \Big(< ap||qr > \tilde{\Gamma}_{bpqr} - < bp||qr > \tilde{\Gamma}_{apqr} \Big)
\end{aligned}
\tag{II.58}
$$

$$
0 = \omega_{ia} + \frac{1}{2}\epsilon_i\lambda_{ia} + \epsilon_i\gamma_{ia} + \frac{1}{2}\sum_{pqr} < ip||qr > \tilde{\Gamma}_{apqr} \tag{II.59}
$$

$$
\begin{aligned}
0 = \omega_{ij} + \delta_{ij}\epsilon_i + \frac{1}{2}\epsilon_i\lambda_{ij} + \epsilon_i\tilde{\gamma}_{ij} + \frac{1}{2}\sum_{pqr} < ip||qr > \tilde{\Gamma}_{jpqr} \\
+\frac{1}{2}\sum_{ka}(< ik||ja > + < jk||ia >)\lambda_{ka} + \frac{1}{2}\sum_{kl} < ik||jl > \lambda_{kl} \\
+\frac{1}{2}\sum_{ab} < ia||jb > \lambda_{ab} + \sum_{kl} < ik||jl > \tilde{\gamma}_{kl} \\
+ \sum_{ka}(< ik||ja > + < jk||ia >)\gamma_{ka} + \sum_{ab} < ia||jb > \gamma_{ab}
\end{aligned}
\tag{II.60}
$$

$$
0 = \omega_{ab} + \epsilon_a\gamma_{ab} + \frac{1}{2}\epsilon_a\lambda_{ab} + \frac{1}{2}\sum_{pqr} < ap||qr > \tilde{\Gamma}_{bpqr} \tag{II.61}
$$

where $\tilde{\Gamma}_{pqrs}$ denotes non-separable parts of Γ_{pqrs}, and:

$$
\begin{aligned}
\sum_{pqr} < ap||qr > \tilde{\Gamma}_{ipqr} &= \sum_{jkl} < aj||kl > \tilde{\Gamma}_{ijkl} + \sum_{bcd} < ab||cd > \Gamma_{ibcd} \\
&+ 2\sum_{jkb} < aj||bk > \tilde{\Gamma}_{ijbk} + \sum_{jkb} < ab||jk > \tilde{\Gamma}_{ibjk} \\
&+ 2\sum_{jbc} < ab||jc > \tilde{\Gamma}_{ibjc} + \sum_{jbc} < aj||bc > \Gamma_{ijbc} \\
\sum_{pqr} < ip||qr > \tilde{\Gamma}_{apqr} &= \sum_{jkl} < ij||kl > \tilde{\Gamma}_{ajkl} + \sum_{bcd} < ib||cd > \Gamma_{abcd} \\
&+ 2\sum_{jkb} < ij||bk > \tilde{\Gamma}_{ajbk} + \sum_{jkb} < ib||jk > \Gamma_{abjk} \\
&+ 2\sum_{jbc} < ib||jc > \tilde{\Gamma}_{abjc} + \sum_{jbc} < ij||bc > \Gamma_{ajbc} \\
\sum_{pqr} < ap||qr > \tilde{\Gamma}_{bpqr} &= \sum_{ijk} < ai||jk > \tilde{\Gamma}_{bijk} + \sum_{cde} < ac||de > \Gamma_{bcde} \\
&+ \sum_{ijc} \Big(< ac||ij > \Gamma_{bcij} + 2 < ai||jc > \tilde{\Gamma}_{bijc} \Big) \\
&+ \sum_{icd} (< ai||cd > \Gamma_{bicd} + 2 < ac||id > \Gamma_{bcid}) \\
\sum_{pqr} < ip||qr > \tilde{\Gamma}_{jpqr} &= \sum_{klm} < ik||lm > \tilde{\Gamma}_{jklm} + \sum_{abc} < ia||bc > \Gamma_{jabc} \\
&+ \sum_{kla} \Big(< ia||kl > \tilde{\Gamma}_{jakl} + 2 < ik||la > \tilde{\Gamma}_{jkla} \Big) \\
&+ \sum_{kab} \Big(< ik||ab > \Gamma_{jkab} + 2 < ia||kb > \tilde{\Gamma}_{jakb} \Big)
\end{aligned}
$$

Eqns. (II.59-II.61) are straightforward to solve w.r.t. ω_{pq}. Eqns. (II.57,II.58) are solved only when frozen core or virtual orbitals are present. Then the corresponding λ_{ij} and λ_{ab} are used in the Eq. (II.56), which should be solved iteratively w.r.t. λ_{ia}. In the case of frozen core/virtual orbitals, all DMs from the above equations are defined only within the active space, while the integrals are full-space. Thus, Λ and

Ω have non-zero terms corresponding to frozen blocks. This is implemented using our general tensor library [138] developed for active space CC models [137,139,217].

Chapter III. Electronic Structure of Halogen-Substituted Methyl Radicals: Excited States of CH_2Cl and CH_2F

Electronically excited states in CH_2Cl and CH_2F radicals are studied at the EOM-CCSD/6-311(3+,3+)G(3df,3pd) level of theory. Excited states' characters and changes in the electronic spectrum in the $CH_3 \rightarrow CH_2F \rightarrow CH_2Cl$ sequence are interpreted in terms of a simple molecular orbital picture. The key factors determining the electronic structure of these radicals are: (i) the presence of lone pairs on the halogen; and (ii) how strongly these lone pairs are bound to the halogen. In CH_2Cl, the small energy gap between the unpaired electron on carbon and the lone pair on chlorine results in additional π-bonding between C and Cl. Moreover, the relatively weak binding energy of the chlorine's lone pairs is responsible for the presence of several low lying valence states in CH_2Cl. In CH_2F, where the lone pairs have a considerably lower energy, no additional bonding is found. The character of two lowest

valence states in CH_2F is similar to that of the lowest states in CH_2Cl, but the excitation energies are considerably higher. The low lying Rydberg states appear to be similar in all three radicals.

III.1 Introduction

Halogen-substituted methyl radicals are intermediates in the photodecomposition and oxidation reactions of halogenated hydrocarbons, which represent an important source of halogen atoms in the atmosphere [75, 78]. Since atmospheric reactions occur at relatively low concentrations, and in the presence of solar radiation, the photodissociation of these radicals may compete with non-photochemical pathways of their decomposition, e.g., bimolecular reactions with other species.

It has been revealed by earlier spectroscopic (see Ref. [115] for the summary of spectroscopic data) and *ab initio* [176] studies that the seeming similarity between the methyl radical and its halogen-substituted derivatives is limited and even deceptive: the interaction of the lone pairs of halogen(s) with the unpaired electron is the cause of anomalously strong C-halogen bonds [10, 36, 37, 116, 225], deviations from planarity [36, 37], and high anharmonicity of the out-of-plane vibrations [10, 116]. Moreover, the availability of non-bonding electrons suggests the presence of low-lying valence excited states in halogenated methyl radicals, as opposed to the methyl radical whose lowest electronically excited states are almost exclusively Rydberg states [21, 98, 99, 111, 165].

Experimental studies of the excited states in halogenated methyl radicals are scarce [42, 112, 153, 181, 200, 247, 250]. Several Rydberg states of CH_2F have been probed by resonance enhanced multi-photon ionization (REMPI) spectroscopy by Hudgens *et al.* [112]. Roussel *et al.* have measured the ultraviolet absorption spectrum of CH_2Cl in the 195-235 nm range. [200]. The photodissociation dynamics of CH_2Cl has been studied by the photofragment imaging technique by Reisler and coworkers [63]. They have also employed the REMPI technique to probe Rydberg states [63]. Earlier, estimations of the energies of the lowest excited state in CH_2Cl and CH_2F have been derived from analysis of microwave spectra [68].

Theoretical studies of excited states in these species [57, 112, 113, 121, 148, 153, 247] have been mostly limited to a selected subset of states such as excited states different in symmetry from the ground state [57, 112, 113, 121, 153, 247] (calculated by Hartree-Fock and MP2). The Rydberg states of these radicals have been indirectly studied by calculating the corresponding ground state cations [57, 113, 121, 149]. Recently, Li and Francisco have reported multi-reference configuration interaction (MRCI) calculations of several valence states of CH_2Cl and CH_2Br [148].

Using the EOM-CCSD method, we have accurately investigated *both valence and Rydberg* states of the CH_2F and CH_2Cl radicals. Since these species have low ionization potentials, their Rydberg states are low in energy. On the other hand, due to the lone pairs of the halogen substituents, there exist low lying valence states. Therefore, Rydberg and valence states can strongly interact, and thus a balanced description of both is crucial to the understanding the photoinduced reactions. We have also

performed qualitative analysis of the excited states in terms of molecular orbitals, and can explain the changes in the electronic spectra in the CH_3 $\rightarrow CH_2F \rightarrow CH_2Cl$ sequence. The focus of this study is on the vertical electronic excitation spectra.

As far as vertical excitation energies are concerned, the EOM-CCSD method can describe singly excited states with remarkable accuracy (0.1-0.3 eV). Unlike multi-reference models, this accuracy is uniform for the valence and Rydberg states, provided that the excited states are derived predominantly from promotion of a single electron. However, in the case of doublet radicals, the performance of EOM-CCSD may degrade when specific doubly excited valence configurations become important. These configurations involve the simultaneous promotion of a spin-α electron from the singly occupied orbital and a spin-β electron into the singly occupied orbital [160]. The natural diagnostics for this situation are provided by: (i) the relative weight of doubly-excited configurations in the EOM-CCSD wave function; and (ii) the presence of larger spin-contamination. For the excited states reported here, these diagnostics remain uniformly small, which suggests that the EOM-CCSD treatment of these radicals is accurate and reliable.

We have also investigated the performance of several computationally inexpensive electronic structure models for these species. We report results for the configuration interaction singles (CIS) [77, 189] method; CIS augmented by perturbative corrections, [CIS(D)] [96]; and time-dependent density functional theory (TD-DFT) [104] employing the Tamm-Dancoff approximation [53, 242].

The structure of this chapter is as follows: Sec. III.2.1 outlines computational details, Sec. III.2.2,III.2.3, and III.2.4 present the results of the vertical electronic spectra calculations, as well as qualitative analysis of the excited states. Our final remarks and conclusions are given in Sec. III.3.

III.2 Results and discussion

III.2.1 Computational details

Vertical electronic excitation energies for CH_2Cl, CH_2F, and CH_3 are calculated at the geometries summarized in Table III.1.

CH_2Cl and CH_3 are planar in the ground state, which agrees with the experiment [10, 68, 116, 170, 211]. Contrary to the experimental results [69, 112, 177], CH_2F is found to be non-planar, with an inversion barrier of 0.014 eV. This issue, as well as the vibrational spectra of these radicals, is discussed in the next chapter. In order to estimate how changes from the non-planar to planar geometry would affect the electronic spectrum, we also report vertical excitation energies at C_{2v} optimized geometry (Table III.1).

This study has employed a 6-311(3+,3+)G(3df,3pd) basis set, derived from the polarized split-valence 6-311G(d,p) basis [133, 162] by augmenting it by additional sets of polarization and diffuse functions [45, 80]. To confirm valence vs. Rydberg assignment for low lying Rydberg states, additional calculations are performed in a 6-311(+,+)G(3df,3pd) basis set. Pure angular momentum spherical harmonics are used

Table III.1: Ground state equilibrium geometries for CH_2X (X=Cl,F,H) radicals, and CH_2F cation.

	Symm.	r_{CH}, Å	r_{CX}, Å	α_{HCH}	Θ^c	E_{nuc}	E_{tot}
CH_2Cl^a (X^2B_1)	C_{2v}	1.076	1.691	124.17	180	45.620 937	-499.007 703
CH_2F^a (X^2A')	C_s	1.079	1.335	124.11	153.11	32.246 535	-138.935 120
CH_2F^a (X^2B_1)	C_{2v}	1.076	1.332	127.60	180	32.274 065	-138.934 617
CH_2F^{+a} (X^1A_1)	C_{2v}	1.093	1.227	125.77	180	34.192 394	-138.608 190
CH_3^b (X^2A_2'')	D_{3h}	1.0767		120	180	9.697 919	

[a] Geometry optimized at CCSD(T)/6-311(+,+)G(3df,3pd) level. Pure angular momentum spherical harmonics are used.

[b] MRCI from [29].

[c] Dihedral HCXH angle.

in this study (5 d-functions, 7 f-functions). The third set of diffuse functions is crucial for the correct description of the components of Rydberg p- and d-states, which are perpendicular to the molecular plane. While adding third set of diffuse functions has no effect on the valence states (including states with high excitation energies), the effect on Rydberg states is very non-uniform. We have found that in the energy range considered the effect does not increase with the excitation energy. Rather, the effect is the greatest for states whose electronic densities exhibit significant changes perpendicular to molecular plane. This is an artifact of atom-centered orbital basis sets: for planar and nearly-planar molecules atom-centered basis sets are capable of better spanning of electronic density in the molecular plane than in the perpendicular direction.

As mentioned in the Introduction, in addition to the EOM-CCSD calculations [124, 230], we also report spin-unrestricted CIS [77, 189], CIS(D) [96], and TD-DFT [104] results obtained in a 6-311(3+,3+)G(3df,3pd) basis set. TD-DFT calculations employ the Tamm-Dancoff approximation [53, 242], and Becke3-Lee-Yang-Parr (B3LYP) functional with LYP and VWN correlation functionals [237].

One of the questions addressed in this study is the valence versus Rydberg character of the excited states. Even though such assignment is not rigorous, it is of great qualitative value for understanding the dynamics of the electronically excited radicals. To achieve a robust assignment, we required that the following three characteristics be consistent: (i) the spherical average of the charge distribution (calculated as an expectation value of the operator R^2) for the ground and excited states (valence

states exhibit a smaller increase in electronic density size than Rydberg states); (ii) the effect of removing two sets of diffuse functions from the basis set (valence states are rather insensitive); and (iii) the character of the molecular orbital to which excitation mainly occur (we identify a canonical Hartree-Fock orbital as having predominantly valence character if it has large overlap with one of the MP2 natural orbitals having largest natural populations [106]).

Quantum numbers are assigned to the Rydberg states based on the following considerations: (i) the Rydberg formula (see below) [98]; (ii) the symmetry; and (iii) the calculated second moments, i.e., $\langle X^2 \rangle$, $\langle Y^2 \rangle$ and $\langle Z^2 \rangle$, of the charge distribution. (ii) and (iii) are in particular useful for discriminating between different m-components.

The Rydberg formula is often used to determine the quantum numbers n and l of Rydberg states [98]:

$$E_{ex} = IP - \frac{13.61}{(n-\delta)^2}, \tag{III.1}$$

where E_{ex} is the excitation energy (in eV) of the Rydberg state, IP is the ionization potential (in eV), n is the principal quantum number, and quantum defect δ is an empirical parameter whose role is to account for the difference between the positively charged complex core cation and the bare nucleus in a hydrogen-like atom. Typical values of δ are 0.9-1.2 for s-states, 0.3-0.6 for p-states, and smaller or equal to 0.1 for d-states [98]. We used experimental values for the vertical ionization potentials, i.e., 8.87 eV for CH_2Cl [8], 9.22 eV for CH_2F [9], and 9.84 eV for CH_3 [66].

III.2.2 CH_2Cl

The leading electronic configuration in the ground state wave function is:

$$(1a_1)^2(2a_1)^2(3a_1)^2(1b_1)^2(4a_1)^2(1b_2)^2(5a_1)^2(6a_1)^2(2b_2)^2(7a_1)^2(2b_1)^2(3b_2)^2(3b_1)^1, \quad \text{(III.2)}$$

with the overall symmetry of the electronic wave function being B_1. $1a_1$, $3a_1$, $1b_1$, $4a_1$, and $1b_2$ are 1s, 2s, $2p_y$, $2p_z$, and $2p_x$ chlorine's core orbitals, respectively; the $2a_1$ orbital is 1s core orbital of carbon. $6a_1$ and $2b_2$ correspond to symmetric and antisymmetric linear combination of two σ_{CH} bonds. $5a_1$ is the 3s orbital of chlorine, and $7a_1$ is the C-Cl σ-bonding orbital, σ_{CCl} (the corresponding anti-bonding orbital, σ^*_{CCl}, is the virtual $11a_1$ orbital). $3b_2$ is $3p_x$ (lone pair) orbital on chlorine. Up to this point, our assignment of the molecular orbitals is identical to that of Li and Francisco [148]. However, we have found that there is a strong interaction between the $3p_y$ lone pair of Cl and the $2p_y$ unpaired electron of C. As a result, two delocalized orbitals, π_{CCl} ($2b_1$) and π^*_{CCl} ($5b_1$), are formed. The bonding π_{CCl} orbital is doubly occupied, and the anti-bonding π^*_{CCl} orbital hosts the unpaired electron. Thus, an additional half-π bond is formed between C and Cl in the CH_2Cl radical.

The (p-p) π additional bonding has been originally suggested by Andrews and Smith in order to explain the shorter bond-length and the higher force constant of the C-Cl bond in the CH_2Cl radical (relative to the corresponding saturated compounds) [10]. They have also noticed that this type of bonding would result in an

anomalous charge distribution: a complete delocalization of the chlorine lone pair and the unpaired electron from carbon would give a -0.5 charge on carbon, and a +0.5 charge on chlorine. We have found that the carbon indeed hosts relatively large negative charge (≈ -0.38), whereas chlorine is slightly positively charged ($\approx +0.03$). Even though the exact values for these charges depend on the electronic density used, and on the partial charge definition employed (i.e., Mulliken or Löwdin charges [238], or natural atomic charges [196]), the overall trend (i.e., a large negative charge on carbon and a small positive one on chlorine) remains unchanged.

Table III.2 contains the vertical transition energies, oscillator strengths, squared electronic transition dipole moments (further on called transition strengths), and the directions of the transition dipole moments.

The vertical transition energies from Table III.2 are shown in Fig. III.1 (panel a).

A molecular orbital picture of the ground state and valence excited states is shown in Fig. III.2.

The lowest excited state of CH_2Cl, 1^2A_1, derives from a valence transition from the anti-bonding π^*_{CCl} orbital to the anti-bonding σ^*_{CCl} orbital. Therefore, it is possible that this state is bound, but with the CCl bond considerably elongated. The vertical excitation energy is found to be 4.92 eV. This value is 0.31 eV lower than the MRCI result from Ref. [148]. The EOM-CCSD value agrees better with the available experimental information, i.e., 4.96-5.02 eV recently determined by Reisler and coworkers [63, 190]. By using the imaging technique, a maximum photofragment yield (Cl and CH_2) was observed around 4.96-5.02 eV. Their results also suggest that

Table III.2: Excited states of CH_2Cl radical. EOM-CCSD/6-311(3+,3+)G(3df, 3pd), pure angular momentum.

State[a]	E_{ex}, eV	D^b_{tr}	μ^2_{tr}, a.u.[c]	Transition[d]
$1\,^2A_1$ (V)	4.92	0.0051	0.0423 (y)	$\pi^*_{CCl} \rightarrow \sigma^*_{CCl}$
$1\,^2B_2$ (V)	5.24			$n^{Cl}_x \rightarrow \pi^*_{CCl}$
$2\,^2A_1$ (3s R)	5.54	0.0008	0.0056 (y)	$\pi^*_{CCl} \rightarrow 3s$
$2\,^2B_1$ (V)	6.33	0.0711	0.4584 (z)	$\pi_{CCl} \rightarrow \pi^*_{CCl}$
$2\,^2B_2$ ($3p_x$ R)	6.34			$\pi^*_{CCl} \rightarrow 3p_x$
$3\,^2B_1$ ($3p_y$ R)	6.61	3×10^{-5}	0.0002 (z)	$\pi^*_{CCl} \rightarrow 3p_y$
$3\,^2A_1$ ($3p_z$ R)	6.72	0.0083	0.0505 (y)	$\pi^*_{CCl} \rightarrow 3p_z$
$4\,^2A_1$ ($3d_{z^2}$ R)	7.15	0.0002	0.0009 (y)	$\pi^*_{CCl} \rightarrow 3d_{z^2}$
$5\,^2A_1$ ($3d_{x^2-y^2}$ R)	7.33	0.0089	0.0496 (y)	$\pi^*_{CCl} \rightarrow 3d_{x^2-y^2}$
$3\,^2B_2$ ($3d_{xz}$ R)	7.38			$\pi^*_{CCl} \rightarrow 3d_{xz}$
$4\,^2B_1$ ($3d_{yz}$ R)	7.45	3×10^{-5}	0.0001 (z)	$\pi^*_{CCl} \rightarrow 3d_{yz}$
$6\,^2A_1$ (4s R)	7.47	0.0022	0.0120 (y)	$\pi^*_{CCl} \rightarrow 4s$
$1\,^4A_2$ (V)	7.54			$n^{Cl}_x \rightarrow \sigma^*_{CCl}$
$4\,^2B_2$ ($4p_x$ R)	7.67			$\pi^*_{CCl} \rightarrow 4p_x$
$5\,^2B_1$ ($4p_y$ R)	7.75	0.0027	0.0144 (z)	$\pi^*_{CCl} \rightarrow 4p_y$
$7\,^2A_1$ ($4p_z$ R)	7.76	0.0062	0.0326 (y)	$\pi^*_{CCl} \rightarrow 4p_z$
$8\,^2A_1$ ($4d_{z^2}$ R)	7.99	0.0051	0.0262 (y)	$\pi^*_{CCl} \rightarrow 4d_{z^2}$
$9\,^2A_1$ (V)	8.02	4×10^{-6}	2×10^{-5} (y)	$\sigma_{CCl} \rightarrow \pi^*_{CCl}$
$5\,^2B_2$ ($4d_{xz}$ R)	8.07			$\pi^*_{CCl} \rightarrow 4d_{xz}$
$10\,^2A_1$ (5s R)	8.09	0.0001	0.0005 (y)	$\pi^*_{CCl} \rightarrow 5s$
$6\,^2B_1$ ($4d_{yz}$ R)	8.12	0.0002	0.0011 (z)	$\pi^*_{CCl} \rightarrow 4d_{yz}$
$2\,^4A_2$ (3s R)	8.26			$n^{Cl}_x \rightarrow 3s$

[a] For valence states, the spherical average of charge distribution, $\langle R^2 \rangle$, is smaller than or equal to 44 bohr^2. In the ground state, $\langle R^2 \rangle \approx 38$ bohr^2.
[b] Oscillator strength.
[c] Direction of transition dipole is shown in parentheses. The OZ axis is parallel to the CCl bond, and OY axis is perpendicular to the molecular plane.
[d] Half-filled molecular orbital is π^*_{CCl} ($5b_1$) (see Fig. III.2).

the transition dipole moment for this state is perpendicular to the CCl bond [63]. A similar value (5.01 eV) has been derived by Endo *et al.* from their analysis of the microwave spectrum of CH_2Cl [68].

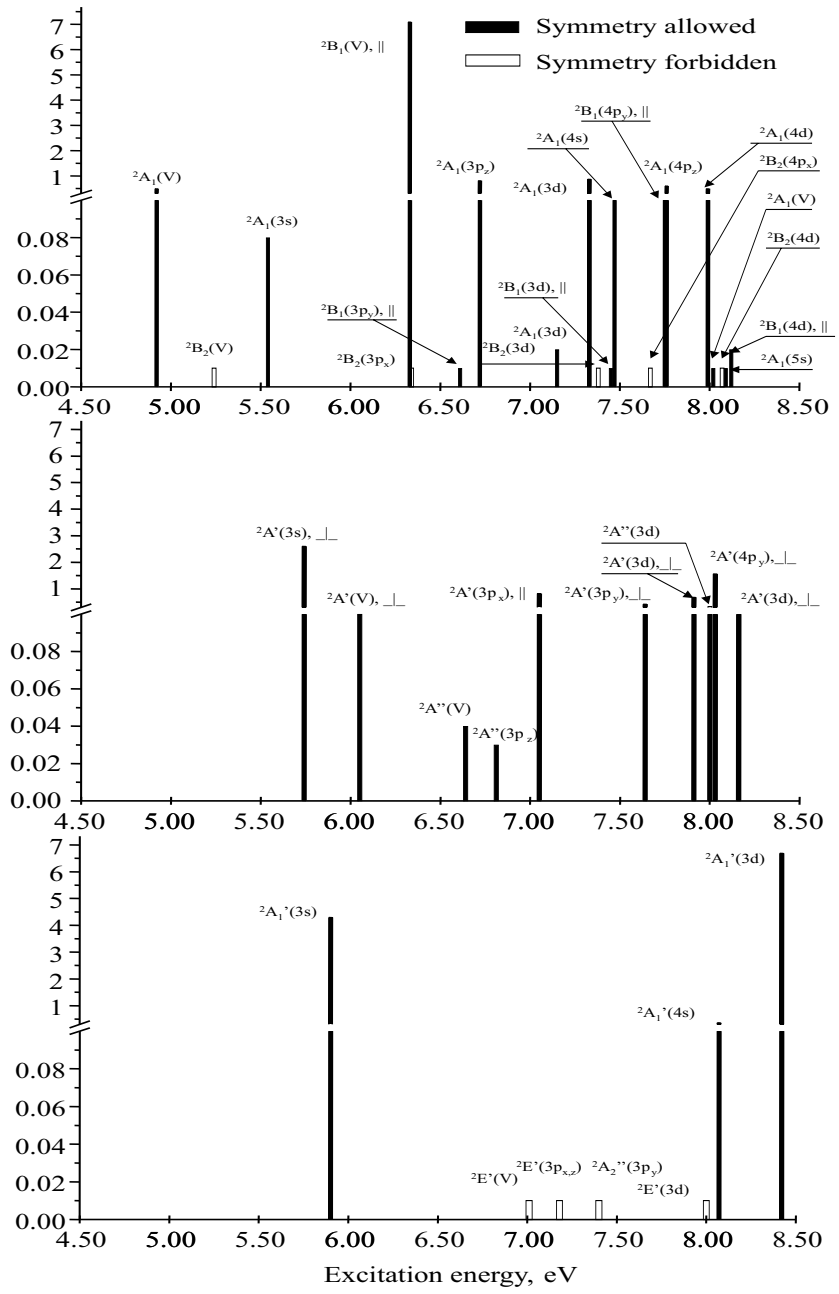

Figure III.1: Vertical excitation energies for CH_2Cl (a), CH_2F (b), and CH_3 (c). Intensities of the transitions are proportional to the oscillator strengths (no Franck-Condon factors are taken into account). Empty bars are used to show positions of forbidden transitions, i.e., those for which oscillator strength is zero due to the symmetry. Transitions are defined as parallel when the transition dipole moment is parallel to the CX bond, and perpendicular otherwise.

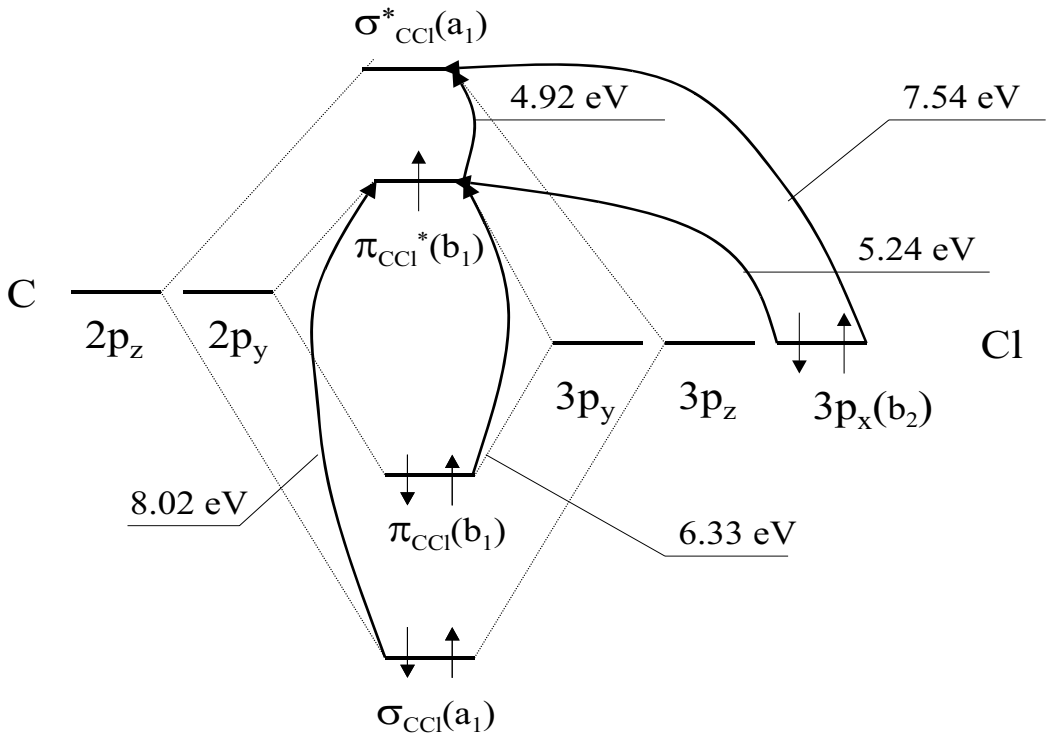

Figure III.2: Molecular orbital picture for the ground and valence excited states of CH_2Cl radical. $7a_1$ orbital is the σ_{CCl} bonding orbital; $2b_1$ orbital is the (p-p)π_{CCl} bonding orbital; $3b_2$ is the $3p_x$ lone pair on Cl atom; $3b_1$ orbital is the singly occupied π-anti-bonding orbital; and virtual $11a_1$ orbital is the σ^*_{CCl}-anti-bonding orbital.

The next excited state, 1^2B_2 at 5.24 eV, is optically dark in C_{2v} symmetry. This is also a valence transition, namely, $n_x^{Cl} \rightarrow \pi^*_{CCl}$. This dark state is closely followed by a Rydberg 2^2A_1 (3s) state at 5.54 eV. Note that the MRCI study [148], which employs (i) the full valence active space for the ground and all reported excited states, and (ii) a basis set with no diffuse functions, overestimates the valence character of this transition, and places it 1.4 eV higher in energy. The dominant Rydberg character of this state is confirmed by all three criteria listed in the Sec. III.2.1. In particular, removing two sets of diffuse functions from the basis increases the excitation energy

by 0.09 eV. For reference, the biggest observed change in this radical for the valence states is 0.04 eV (detected for the 2^2B_1 and 9^2A_1 states).

The strongest transition in the studied energy interval is to the valence 2^2B_1 state at 6.33 eV. The large value of the transition dipole moment is in agreement with our assignment of this state as $\pi_{CCl} \rightarrow \pi^*_{CCl}$ excitation (transitions involving the promotion of an electron from a bonding orbital to the corresponding anti-bonding orbital are usually the strongest, as shown by Mulliken [179]). This transition was observed experimentally as a broad peak centered around 6.20 eV in the ultraviolet absorption spectrum of CH_2Cl [200], and it was shown that the transition dipole moment is parallel to the C-Cl bond [63]. The transition is so strong (the absorption cross section is about 1.45×10^{-17} cm^2 molecule^{-1}), that several other states are likely to be buried under its tails. Note that the EOM-CCSD value for the excitation energy (6.33 eV) is closer to the observed maximum in the absorption spectrum (6.20 eV) than the MRCI value of 6.51 eV [148].

Except for the very weak $\sigma_{CCl} \rightarrow \pi^*_{CCl}$ transition at 8.02 eV (to the 9^2A_1 state), all other doublet states in this energy interval are Rydberg states. Since all Rydberg states reported here involve excitations of the unpaired electron from the π^*_{CCl} orbital, we expect them to have planar structures with a contracted CCl bond, and a higher C-Cl and out-of-plain vibrational frequencies. Reisler and co-workers [63] have detected a 3p Rydberg state at 6.59 eV by 2+1 REMPI technique. Most likely, this is the $3\ ^2B_1$ ($3p_y$) state for which the EOM-CCSD energy is 6.61 eV.

In the energy region examined there are two quartet states, both of A_2 symmetry: the valence ($n_x^{Cl} \rightarrow \sigma_{CCl}^*$) state at 7.54 eV, and the Rydberg ($n_x^{Cl} \rightarrow 3s$) state at 8.26 eV. As expected from qualitative considerations, the corresponding doublet states lie higher in energy (for quartet states, Pauli repulsion keeps the electrons apart, thus resulting in smaller electron-electron repulsion). Note that in closed shell molecules, where any excitation unpairs electrons, the lowest excited state is usually a triplet state. In doublet radicals, however, low lying states are promotions of the unpaired electron, and, therefore, are doublets. Nevertheless, when excitation energy becomes high enough to involve excitation of "core" electrons, quartets have lower energies than the corresponding doublets.

Table III.3 compares the results of CIS, CIS(D), and TD-DFT methods with the EOM-CCSD model, and summarizes the available experimental data.

As usual, CIS systematically overestimates the excitation energies by at least 1 eV (up to 1.7 eV for the valence 1^2B_2 and 2^2B_1 states). The seemingly smaller errors for the quartet states are artifacts of the large spin-contamination of these states.

Since the electronic spectrum is rather dense, errors of 1 eV and more could result in a totally incorrect ordering of the excited states, but, since the CIS errors are systematic, the relative order of states has only a few errors.

CIS(D) model represents a systematic improvement: errors against EOM-CCSD are about 0.1 eV or less for most of the states (the maximum error does not exceed $\sim$ 0.45 eV). Moreover, the double corrections partially restore the correct order of the excited states.

Table III.3: Excitation energies (eV) for CH_2Cl radical. A comparison between EOM-CCSD, CIS, CIS(D), TD-DFT/B3LYP, and MRCI methods.

State	EOM-CCSD[a]	TD-DFT[a]	CIS[a]	CIS(D)[a]	$\langle S^2 \rangle_{CIS}$	MRCI[b]	Exp.
$1\ ^2A_1$ (V)	4.92	4.53	5.72	5.13	0.95	5.23	4.96-5.02 [63, 68]
$1\ ^2B_2$ (V)	5.24	4.75	6.85	5.51	0.85	5.35	
$2\ ^2A_1$ (3s R)	5.54	5.00	6.52	5.67	0.93	6.93	
$2\ ^2B_1$ (V)	6.33	6.04	8.00	6.67	0.90	6.51	6.20 [200]
$2\ ^2B_2$ ($3p_x$ R)	6.34	5.54	7.30	6.39	0.87		
$3\ ^2B_1$ ($3p_y$ R)	6.61	5.64	7.43	6.55	0.91		6.59 [63]
$3\ ^2A_1$ ($3p_z$ R)	6.72	5.75	7.65	6.80	0.97		
$4\ ^2A_1$ ($3d_{z^2}$ R)	7.15	5.83	8.13	7.23	0.87		
$5\ ^2A_1$ ($3d_{x^2-y^2}$ R)	7.33	5.97	8.28	7.36	0.93		
$3\ ^2B_2$ ($3d_{xz}$ R)	7.38	5.91	8.37	7.37	0.92		
$4\ ^2B_1$ ($3d_{yz}$ R)	7.45	6.00	8.42	7.44	0.94		
$6\ ^2A_1$ (4s R)	7.47	6.03	8.43	7.41	0.91		
$1\ ^4A_2$ (V)	7.54	7.08	7.73	7.63	2.64		
$4\ ^2B_2$ ($4p_x$ R)	7.67	5.99	8.64	7.59	0.89		
$5\ ^2B_1$ ($4p_y$ R)	7.75	6.22	8.70	7.65	0.90		
$7\ ^2A_1$ ($4p_z$ R)	7.76	6.17	8.71	7.74	1.03		
$8\ ^2A_1$ ($4d_{z^2}$ R)	7.99	6.36	8.97	7.91	0.92		
$9\ ^2A_1$ (V)	8.02	7.75	8.87	8.47	1.51		
$5\ ^2B_2$ ($4d_{xz}$ R)	8.07	6.27	9.04	7.97	0.91		
$10\ ^2A_1$ (5s R)	8.09	6.54	9.05	7.98	0.92		
$6\ ^2B_1$ ($4d_{yz}$)	8.12	6.63	9.09	8.03	0.94		
$2\ ^4A_2$ (3s R)	8.26	7.64	8.78	8.28	2.69		

[a] 6-311(3+,3+)G(3df,3pd) basis set, pure angular momentum. Geometry is from Table III.1.

[b] MRCI from Ref. [148]. The full valence active space is used for CASSCF reference. Basis set is cc-pVTZ.

The TD-DFT results are more accurate for valence states than those of CIS: excitation energies are underestimated by 0.3-0.5 eV. However, due to the incorrect asymptotic behavior of the functional used, the errors for Rydberg states increase from 0.54 eV for the 3s state up to about 1.5-1.7 eV for the higher states. As shown in Fig. III.3, the TD-DFT errors are proportional to the size of the electron density.

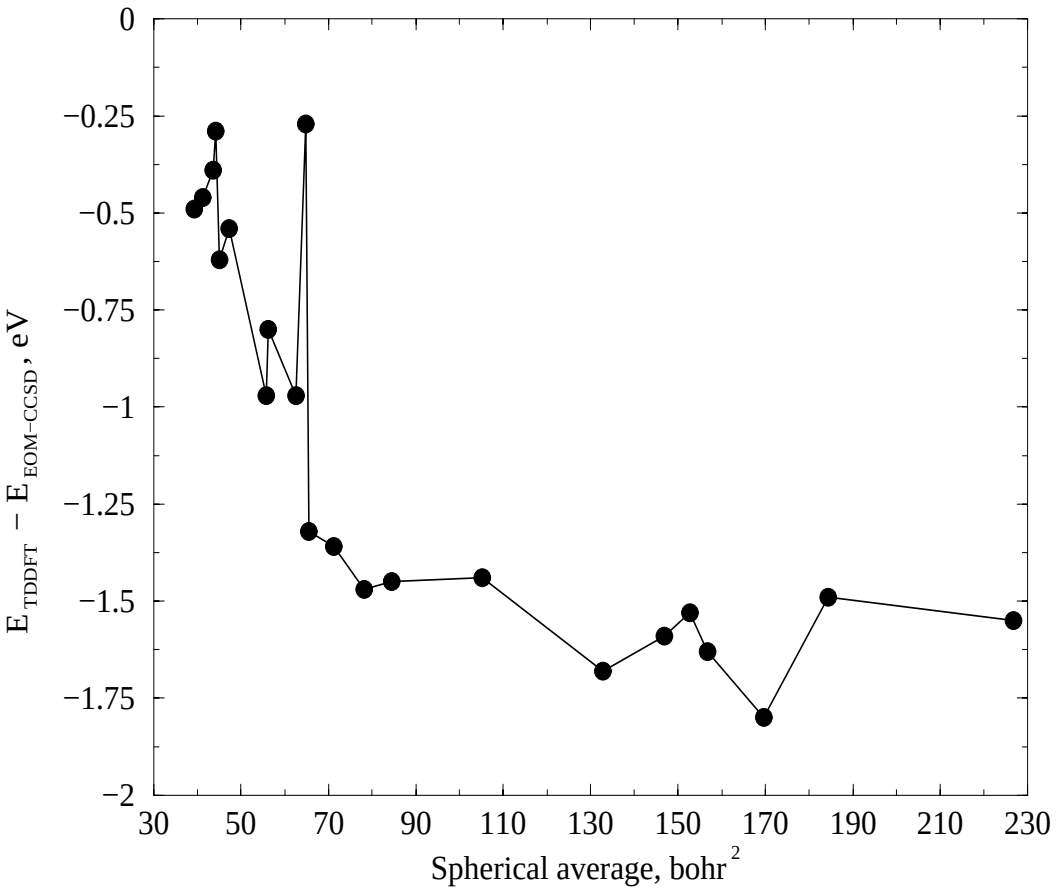

Figure III.3: Errors in the TD-DFT excitation energies vs spherical average of the charge distribution for the CH_2Cl radical.

As explained above, due to a poor basis set selection, the MRCI results [148] overestimate the valence character of the excited states, resulting in errors in the excitation energies of 0.11-1.39 eV.

III.2.3 CH_2F

The leading electronic configuration in the ground state wave function is:

$$(1a')^2(2a')^2(3a')^2(4a')^2(1a'')^2(5a')^2(6a')^2(2a'')^2(7a')^1, \qquad \text{(III.3)}$$

with the overall symmetry of the ground state electronic wave function being A'. $1a'$ and $2a'$ are 1s core orbitals on fluorine and carbon, respectively. $6a'$ orbital is the σ_{CF} bond, $2a''$ is the $2p_z$ lone pair orbital on fluorine (perpendicular to the symmetry plane), and $7a'$ is the singly occupied $2p_x$ lone pair on carbon. $3a'$ is the 2s orbital on F, $4a'$ and $1a''$ are the symmetric and antisymmetric combinations of the localized σ_{CH} bonds. $5a'$ orbital is the $2p_x$ lone pair on fluorine, which is significantly lowered in energy by partial hybridization with the 2s orbital on F. Note that, unlike in CH_2Cl, there is no significant (p-p)π bonding between C and F because the large energy gap between the lone pairs on F and the unpaired electron on carbon prevents delocalization. Consequently, there is no anomalous charge distribution in CH_2F (carbon and fluorine host positive and negative charges, respectively), and there is only a minor C-F bond contraction in CH_2F relative to the corresponding saturated compounds [69].

Table III.4: Excited states of CH_2F radical. EOM-CCSD/6-311(3+,3+)G(3df, 3pd).

State[a]	E_{ex}, eV	D^b_{tr}	μ^2_{tr}, a.u.[c]	Transition[d]	At C_{2v} geometry[e]
$2\,^2A'$ (3s R)	5.74	0.0262	0.1862 (xy)	$2p^C_x \rightarrow 3s$	5.47 (A_1)
$3\,^2A'$ (V)	6.05	0.0010	0.0069 (xy)	$2p^C_x \rightarrow \sigma^*_{CF}$	5.76 (A_1)
$1\,^2A''$ (V)	6.64	0.0004	0.0022 (z)	$n^F_z \rightarrow 2p^C_x$	6.90 (B_2)
$2\,^2A''$ (3p$_z$ R)	6.81	0.0003	0.0015 (z)	$2p^C_x \rightarrow 3p_z$	6.50 (B_2)
$4\,^2A'$ (3p$_x$ R)	7.05	0.0084	0.0480 (xy)	$2p^C_x \rightarrow 3p_x$	6.80 (B_1)
$5\,^2A'$ (3p$_y$ R)	7.64	0.0044	0.0233 (xy)	$2p^C_x \rightarrow 3p_y$	7.31 (A_1)
$6\,^2A'$ (3d$_{y^2}$ R)	7.91	0.0070	0.0362 (xy)	$2p^C_x \rightarrow 3d_{y^2}$	7.62 (A_1)
$3\,^2A''$ (3d$_{zy}$ R)	8.00	0.0035	0.0179 (z)	$2p^C_x \rightarrow 3d_{zy}$	7.75 (B_2)
$7\,^2A'$ (4p$_y$ R)	8.03	0.0158	0.0802 (xy)	$2p^C_x \rightarrow 4p_y$	7.75 (A_1)
$8\,^2A'$ (3d$_{xy}$ R)	8.16	0.0014	0.0068 (xy)	$2p^C_x \rightarrow 3d_{xy}$	7.91 (B_1)

[a] For valence states, the spherical average of charge distribution is smaller than or equal to 29 bohr^2. In the ground state, $\langle R^2 \rangle \approx 22$ bohr^2.
[b] Oscillator strength.
[c] Direction of transition dipole is shown in parentheses. The C_s plane is OXY, and the C-F bond is parallel to OY axis. OZ axis is perpendicular to the symmetry plane.
[d] Half-filled molecular orbital is $2p^C_x$ (see Fig. III.4).
[e] See Table III.1.

The absence of additional (p-p)π bonding and the lower energies of the fluorine's lone pairs are the two factors that cause the major differences in the electronic spectrum of CH_2F as compared to CH_2Cl. As shown in Table III.4 and Fig. III.1 (panel b), (i) the lowest excited state in CH_2F is a Rydberg $2^2A'$(3s) state at 5.74 eV; (ii) in the energy interval studied, there are only two valence states: $3^2A'$ at 6.05 eV and $1^2A''$ at 6.64 eV.

Fig. III.4 shows a molecular orbital picture of the ground and excited valence states in CH_2F.

The two lowest valence states can be correlated with two lowest valence states of CH_2Cl: in both cases the lowest valence state derives from the promotion of the

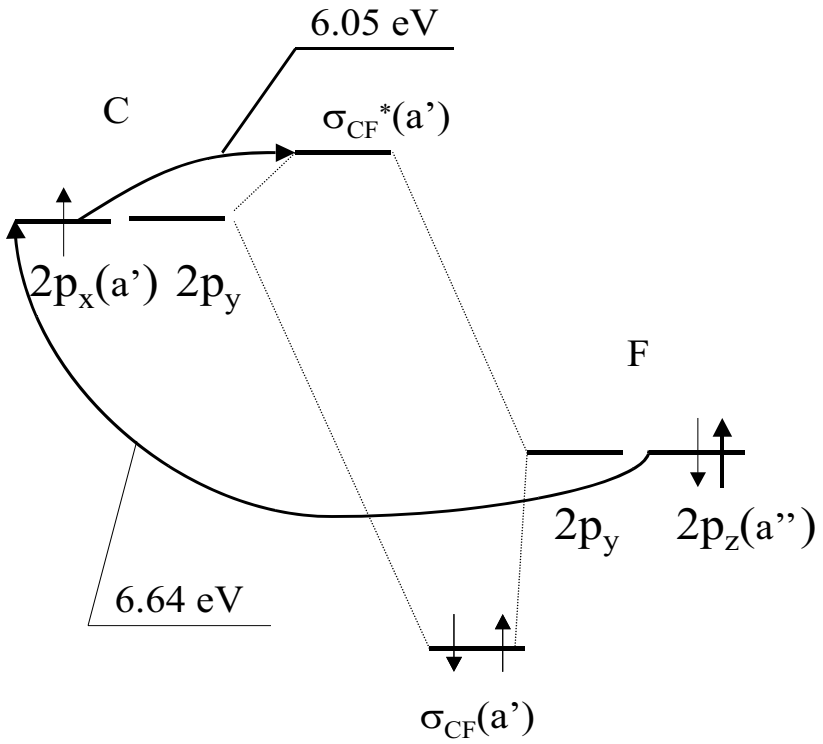

Figure III.4: Molecular orbital picture for the ground and valence excited states of CH_2F radical. $6a'$ is the σ_{CF} bonding orbital; $2a''$ is the $2p_z$ lone pair on F atom; $7a'$ is the carbon p-orbital hosting the unpaired electron; and virtual $12a'$ orbital is the σ^*_{CF}-anti-bonding orbital.

unpaired electron to the σ^*_{CX} orbital, while the second state derives from the promotion of an electron to the half-filled orbital. However, the different character of orbitals involved, i.e., delocalization in CH_2Cl vs. localization in CH_2F, results in a more than 1 eV rise in the excitation energies. The rest of the excited states in this energy interval are Rydberg states deriving from promotions of the unpaired electron. These states are expected to be planar, with a slightly contracted CF bond.

Unlike the CH_2Cl case, the assignment of the Rydberg states is more problematic for CH_2F: the calculated spectrum does not agree well with the one estimated

by Eq. (III.1). Moreover, the calculated second momenta of the charge distribution suggest significant mixing of different angular momentum components, i.e., ns, np, and nd Rydberg states. Therefore, the assignment given in the Table III.4 is very approximate. A possible reason for the strong coupling (and, therefore, mixing) of the different angular momentum components of Rydberg states may be the relatively large charge separation in the core cation.

Since the barrier between the two C_s minima in the ground state is very small, i.e., 0.014 eV at the CCSD(T) level, it turns out that the zero-point vibrational level is above the barrier (see Chapter IV and reference [146] for details). Thus, the radical behaves as effectively planar, which reconciles the theoretical predictions (C_s structure) with the experimental observations supporting a C_{2v} symmetry [69, 112, 177]. To estimate the possible effect of this pseudo-planar behavior on the electronic spectrum, we also report (Table III.4) excitation energies calculated at the C_{2v} optimized geometry (Table III.1). Note that the difference in excitation energies exceeds the ground state energy difference of 0.014 eV: all excitations energies are lowered by 0.25-0.33 eV (relative to the C_s structure), except for the $1^2A''$ state, which is 0.26 eV higher in C_{2v}. This behavior is readily rationalized: all excited states except $1^2A''$ involve excitation of the unpaired electron and thus are expected to exhibit a more cation-like (i.e., planar) structure. Therefore, their energies are lower at the planar geometry. In contrast, the $1^2A''$ state involves a promotion of an electron from the lone pair on fluorine to a half-filled $2p$ orbital of carbon. This electronic configuration suggests sp^3 hybridization of carbon, and, subsequently, a non-planar structure.

Therefore, the energy of this state is lower for C_s geometry. The important conclusion, however, is that the overall effect does not exceed 0.33 eV.

Some of the Rydberg states of the CH_2F radical have been probed experimentally by Hudgens *et al.* [112] They have reported the 0_0^0 transition energies for the 3p, 4p, and 5p states of 6.55, 7.85, and 8.34 eV, respectively. The components (i.e., x,y,z components of the np states) have not been assigned [112]. This, as well as the poor performance of the Rydberg formula (which has been used to assign the experimentally observed transitions [112]), complicates the comparison with the experimental results. Unfortunately, the calculated transition strengths cannot be used to identify which components of the np states were detected, since the experiment involves two-photon transitions [112]. Assuming that the EOM-CCSD errors do not exceed 0.3 eV, the experimentally observed transitions can be assigned as excitations to the $3p_z$ and $4p_y$ states (based on both C_s and C_{2v} vertical excitation energies). We also performed a simple estimation of the adiabatic excitation energies by calculating excited states at the equilibrium geometry of the cation, CH_2F^+ (Table III.1), as well as estimations of the zero-point energy contributions by using the experimental frequencies [112]. The corresponding excitation energies are 6.53 and 7.79 eV for the $3p_z$ and $4p_y$ states, respectively. Lastly, with zero-point energy corrections, the theoretical 0_0^0 transition energies for the $3p_z$ and $4p_y$ states are 6.62 eV and 7.88 eV, respectively. These numbers are also within 0.3 eV of the experimental values.

The vertical excitation energies for the CH_2F radical calculated by CIS, CIS(D), and TD-DFT are presented in Table III.5.

Table III.5: Excitation energies (eV) for CH_2F radical. A comparison between EOM-CCSD, CIS, CIS(D), and TD-DFT/B3LYP methods[a].

State	EOM-CCSD	TD-DFT	CIS	CIS(D)	$\langle S^2 \rangle_{CIS}$	Exp. (E_{00}) [112]
2 $^2A'$(3s R)	5.74	4.97	6.76	5.82	0.78	
3 $^2A'$(V)	6.05	5.42	7.05	6.19	0.79	
1 $^2A''$ (V)	6.64	6.21	8.05	6.98	0.81	
2 $^2A''$(3p$_z$ R)	6.81	5.72	7.82	6.80	0.78	6.55
4 $^2A'$(3p$_x$ R)	7.05	5.86	8.06	7.06	0.79	
5 $^2A'$(3p$_y$ R)	7.64	6.00	8.77	7.66	0.79	
6 $^2A'$(3d$_{y^2}$ R)	7.91	6.11	9.01	7.84	0.79	
3 $^2A''$(3d$_{zy}$ R)	8.00	6.13	9.15	7.93	0.79	
7 $^2A'$(4p$_y$ R)	8.03	6.30	9.13	7.92	0.78	7.85
8 $^2A'$(3d$_{xy}$ R)	8.16	6.31	9.32	8.06	0.79	

[a] 6-311(3+,3+)G(3df,3pd) basis set, pure angular momentum. Geometry is from Table III.1.

CIS and CIS(D) perform rather similarly to the CH_2Cl case, the errors being slightly larger. The spin-contamination of the CIS states is smaller and more uniform. That is why the ordering of states by CIS and CIS(D) is almost correct (and, perhaps, also because the spectrum is less dense). The performance of TD-DFT in this case is poor: the errors are not uniform, and gradually increase from 0.4-0.6 eV (for valence states) up to 1.87 eV for the higher Rydberg states. The errors are larger than in the CH_2Cl case because of the increasing Rydberg character in the excited states.

III.2.4 Comparisons of the excited states in the CH_3 $\rightarrow CH_2F \rightarrow CH_2Cl$ sequence

In order to address the issue of the effect of the halogen atoms on the electronic spectrum, we compare the character of the excited states in the CH_3 $\rightarrow CH_2F \rightarrow CH_2Cl$ sequence.

The electronic configuration of the ground state of the CH_3 radical is:

$$(1a_1')^2(2a_1')^2(1e')^4(1a_2'')^1 \qquad \text{(III.4)}$$

The electronic symmetry of the ground state is A_2''. $1a_1'$ is the carbon core orbital, $2a_1'$ and $1e'$ are totally symmetric and doubly degenerate combinations of the localized σ_{CH} bonds, respectively, and $1a_2''$ is the singly occupied $2p_y$ orbital.

Table III.6 and Fig. III.1 (panel c) show vertical excitation energies for CH_3.

Table III.6: Excited states of CH_3 radical. EOM-CCSD/6-311(3+,3+)G(3df,3pd), pure angular momentum.

State[a]	E_{ex}, eV	D^b_{tr}	μ^2_{tr}, a.u.[c]	Transition[d]
$1\,^2A'_1$ (3s R)	5.90	0.0431	0.2983 (y)	$2p_y^C \rightarrow 3s$
$1\,^2E'$ (V)	7.01			$\sigma_{CH} \rightarrow 2p_y^C$
$2\,^2E'$ ($3p_{x,z}$ R)	7.18			$2p_y^C \rightarrow 3p_x, 3p_z$
$2\,^2A''_2$ ($3p_y$ R)	7.40			$2p_y^C \rightarrow 3p_y$
$3\,^2E'$ ($3d_{yz,xy}$ R)	8.00			$2p_y^C \rightarrow 3d_{yz}, 3d_{xy}$
$2\,^2A'_1$ (4s R)	8.07	0.0038	0.0193 (y)	$2p_y^C \rightarrow 4s$
$3\,^2A'_1$ ($3d_{xz}$ R)	8.42	0.0670	0.3250 (y)	$2p_y^C \rightarrow 3d_{xz}$
$4\,^2E'$ ($4p_{x,z}$ R)	8.53			$2p_y^C \rightarrow 4p_x, 4p_z$
$3\,^2A''_2$ ($4p_y$ R)	8.61			$2p_y^C \rightarrow 4p_y$

[a] For valence states, the spherical average of charge distribution is smaller than or equal to 12 bohr^2. $\langle R^2 \rangle$ for the ground state is 10 bohr^2.
[b] Oscillator strength.
[c] Direction of transition dipole is shown in parentheses. The CH_3 molecule is in OXZ plane.
[d] Half-filled molecular orbital is $2p_y^C$ (see Fig. III.5).

The molecular orbital picture of the ground and a valence excited states is shown in Fig. III.5.

Due to the absence of the lone pairs of halogen, the lowest valence state in CH_3 involves excitation from a bonding σ_{CH} orbital to a half-occupied p_y orbital on carbon, located at 7.01 eV. The rest of the states in this energy interval are Rydberg states involving promotion of the unpaired electron.

Note that the lowest Rydberg state in all three radicals derives from a promotion of the unpaired electron to a 3s Rydberg orbital. The excitation energies for this Rydberg state appear to be surprisingly insensitive to the core cation nature (5.90 eV in CH_3, 5.74 eV in CH_2F, and 5.54 eV in CH_2Cl). The similar result holds for the 3p Rydberg states as well: the excitation energies for all three radicals lie within 1 eV,

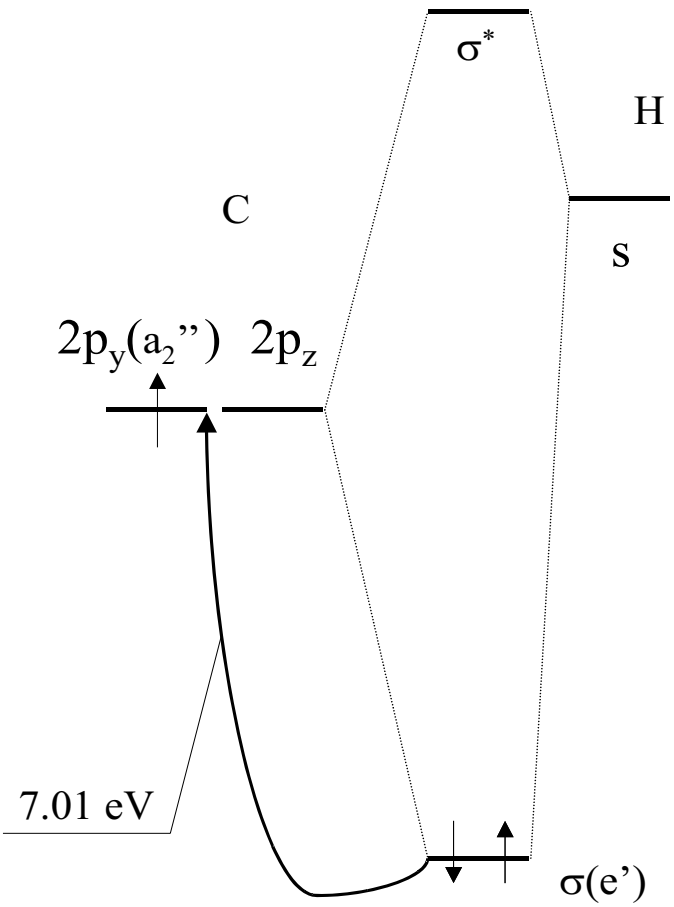

Figure III.5: Molecular orbital picture for the ground and valence excited states of CH_3 radical. 1 and 2 e' are the doubly degenerate combination of the localized C-H bonds; and $1a_2''$ is carbon's p-orbital hosting the unpaired electron.

the differences being smaller between CH_3 and CH_2F (about 0.4 eV). Therefore, the nature and even the excitation energies for the low lying Rydberg states are similar in all three radicals. The transition strengths, however, are very different due to symmetry imposed selection rules, i.e., the $B_1 \rightarrow B_2$ transition is forbidden in C_{2v}, and the $A_2'' \rightarrow A_2'$, $A_2'' \rightarrow A_2''$, $A_2'' \rightarrow E'$, and $A_2'' \rightarrow A_1''$ ones are forbidden in D_{3h} symmetry.

The valence states, however, are very different. The number of low-lying valence states increases as we move from CH_3 to CH_2F, and then to CH_2Cl. The key factors determining the character and excitation energies of the valence states are the presence of the lone pairs on halogen, and how strongly they are bound to the halogen. As far as valence states in CH_2F and CH_2Cl are concerned, the nature of the two lowest valence states is very similar, however, the lowest valence state in CH_2F lies more than 1 eV above the lowest valence state in CH_2Cl.

Table III.7 presents the excitation energies calculated by the CIS, CIS(D) and TD-DFT methods.

CIS overestimates excitation energies by about 0.5-0.7 eV, except the valence state, for which the error is 0.94 eV. CIS(D) performs very well for the Rydberg states: it gives an error of 0.12 eV for the first (3s) state, and then the errors become less then 0.1 eV. The excitation energy to the valence $1^2E'$ state is overestimated by 0.3 eV. Similarly to CH_2Cl and CH_2F, the TD-DFT errors in excitation energies for the Rydberg states are large, i.e., 0.7-2 eV. Moreover, the TD-DFT ordering of states is erroneous, despite the fact that the spacing between individual states is relatively large for this radical. The MRCI excitation energies, calculated by Mebel and Lin [165] (see Table III.7), differ from the EOM-CCSD excitation energies by no more than 0.23 eV, with the difference for four states out of the seven considered being smaller than 0.05 eV.

Table III.7: Excitation energies (eV) for CH_3 radical. A comparison between EOM-CCSD, CIS, CIS(D), TD-DFT/B3LYP, and MRCI methods.

State	EOM-CCSD	TD-DFT	CIS	CIS(D)	$\langle S^2 \rangle_{CIS}$	MRCI [165]	Exp. (E_{00})
$1\,^2A_1'$(3s R)	5.90	5.20	6.55	6.02	0.76	5.86	5.73 [99]
$1\,^2E'$(V)	7.01	6.87	7.95	7.31	0.78	7.13	
$2\,^2E'$($3p_{x,z}$ R)	7.18	6.06	7.77	7.18	0.77	6.95	
$2\,^2A_2''$($3p_y$ R)	7.40	6.17	7.95	7.46	0.77	7.37	7.44 [111]
$3\,^2E'$($3d_{yz,xy}$ R)	8.00	6.40	8.72	8.05	0.76	8.03	
$2\,^2A_1'$(4s R)	8.07	6.27	8.75	8.07	0.76	8.10	
$3\,^2A_1'$($3d_{xz}R$)	8.42	6.64	9.07	8.45	0.76	8.36	8.2 [99]
$4\,^2E'$($4p_{x,z}$ R)	8.53	6.62	9.21	8.47	0.76		
$3\,^2A_2''$($4p_y$ R)	8.61	6.62	9.26	8.54	0.77		8.66 [21]

[a] 6-311(3+,3+)G(3df,3pd) basis set, pure angular momentum. Geometry is from Table III.1.

III.3 Conclusions

In this chapter, we report the vertical electronic excitation energies for CH_2Cl, CH_2F, and CH_3 radicals, and present a qualitative molecular orbital picture for the ground and excited states. The key factors determining the character of the ground state and valence excited states are: (i) the presence of lone pairs on halogen; and (ii) how strongly these lone pairs are bound to the halogen. The small energy gap between the unpaired electron of carbon and the lone pair of chlorine results in an additional (p-p)-π bonding in CH_2Cl. This explains why the CCl bond is shorter and stronger in CH_2Cl as compared to the saturated compound. In contrast, there is no significant electron delocalization, and, therefore, additional bonding in CH_2F.

The energies and the character of the valence excited states are also determined by the energies of halogen lone pairs. As expected, the number of low-lying valence states increases in CH_3 $\rightarrow$$CH_2F$$\rightarrow$$CH_2Cl$ sequence. In CH_2F and CH_2Cl the nature of the two lowest valence states is similar, but the lowest valence state in CH_2F lies more than 1 eV above the lowest valence state in CH_2Cl. The low lying Rydberg states appear to be similar in all three radicals, i.e., the excitation energies for $3s$, $3p$, and $4s$ states are found to be rather insensitive to the core cation nature. The transition strengths, however, are very different due to symmetry selection rules. As a general trend, the Rydberg excited states in CH_2F are more similar to those in CH_3, rather than to those in CH_2Cl.

We have also investigated the performance of less expensive electronic structure models for these radicals. The major conclusion is that TD-DFT/B3LYP [237] yields rather large and non-systematic errors (due to the incorrect asymptotic behavior of the functional employed). The performance of CIS is more uniform, and, even though the errors are rather large ($>$ 1 eV), the accuracy of CIS is approximately the same for all three radicals, and the ordering of states is reproduced better than by TD-DFT. CIS(D) model presents a systematic improvement over CIS.

The atmospheric implications concern the interesting question posed by Li and Francisco [148]: do these radicals absorb significantly solar light at the wavelengths available at altitudes around 30 km, i.e. where there is a maximum in ozone abundance [75] (see Fig. III.6). At this altitude, significant actinic fluxes are available at the wavelengths $>$ 280 nm (E $<$ 4.43 eV). The vertical excitation for the lowest excited state in CH_2Cl is about 0.5 eV higher. Nevertheless, a definite conclusion about the importance of the photo-absorption at these wavelengths can be drawn only when Franck-Condon factors are taken into account. This is discussed in Chapter V and reference [144]. The actinic fluxes available at 190-230 nm (5.34-6.53 eV) are two orders of magnitude lower, but still considerable. Therefore, one may expect a considerable absorption by CH_2Cl, since its strongest electronic transition has been found to be at 6.20-6.33 eV. The strongest transition in CH_2F, i.e., to the 2 $^2A'$ state, also occurs in this interval (at 5.74 eV).

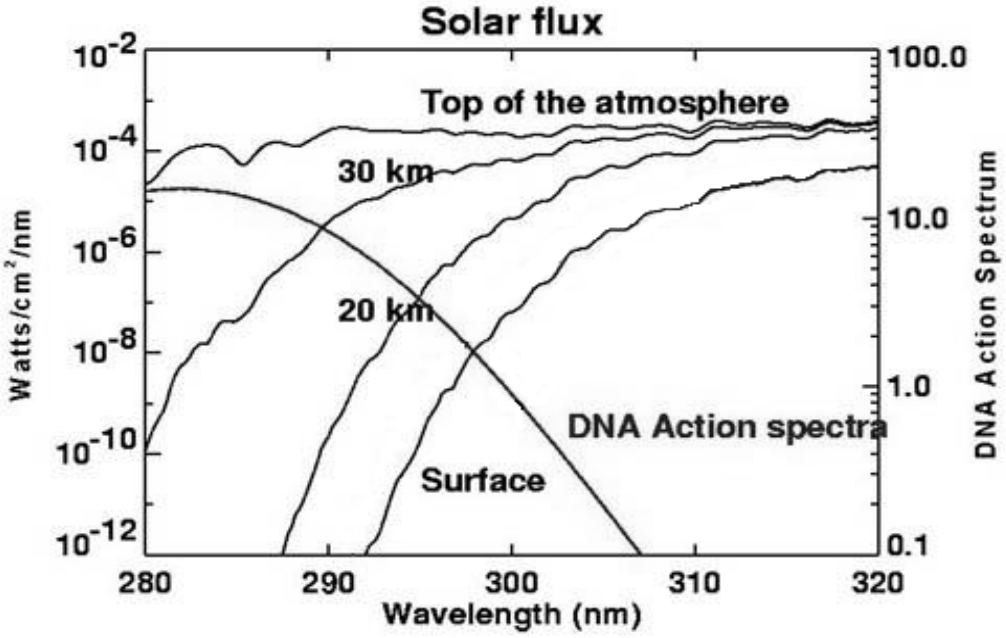

Figure III.6: Solar flux at different altitudes in the atmosphere. DNA action spectrum, i.e., the probability of DNA damage by UV radiation at various wavelengths, is also shown.

Chapter IV. Electronic Structure of Halogen-Substituted Methyl Radicals: Equilibrium Geometries and Vibrational Spectra of CH_2Cl and CH_2F

Anharmonic corrections for the out-of-plane (OPLA) vibrational modes of CH_2Cl, CH_2F, and CH_3 radicals have been calculated. For these radicals, it is possible to describe the OPLA motion within a simple one-dimensional model based on the adiabatic separation of the (slowest) OPLA mode from all other vibrations. The effective potentials have been calculated by CCSD(T) and DFT/B3LYP methods with 6-311(+,+)G(3df,2pd) basis sets. It is found that halogen substitution increases the anharmonicities dramatically, i.e., from 19 % in CH_3 up to about $\pm$ 100 % in CH_2Cl and CH_2F. The resulting frequencies of the fundamental OPLA transition are in a good agreement with the experimental values. In the case of CH_2F, the large anharmonicity in the OPLA mode results in a wave function delocalized over the two

minima of the double well potential. This reconciles the experimentally determined planar (C_{2v}) structure with the calculated pyramidal (C_s) equilibrium geometry.

IV.1 Introduction

The methyl radical in its ground electronic state possesses a rather rigid, planar (D_{3h}) structure, and the frequency of its out-of-plane (OPLA) vibration is about 600 cm^{-1} [72, 98, 172, 243, 256]. This is easily rationalized in terms of hybridization theory: the unpaired electron occupies the $2p_z$ orbital of carbon, while the 2s, $2p_x$, and $2p_y$ orbitals form three equivalent σ_{CH} bonds (sp^2-hybridization). Obviously, the repulsion between the unpaired electron and those involved in the CH bonds is minimal for the planar structure, and it rapidly increases for large amplitude OPLA displacements. That is why the anharmonicity of the OPLA mode is *negative* (i.e., the potential steepness increases with a vibrational excitation), as opposed to the *positive* anharmonicity found for a stretching Morse-type potential (see Fig. IV.1). Such anharmonicity (about 11 % from the experimental fundamental frequency ω_{01} value) for the OPLA mode of the methyl radical has been postulated by Riveros [199] in order to explain the deviation of the observed [172] isotope shifts of the OPLA fundamentals from the values calculated assuming a planar structure [72], and harmonic OPLA motion.

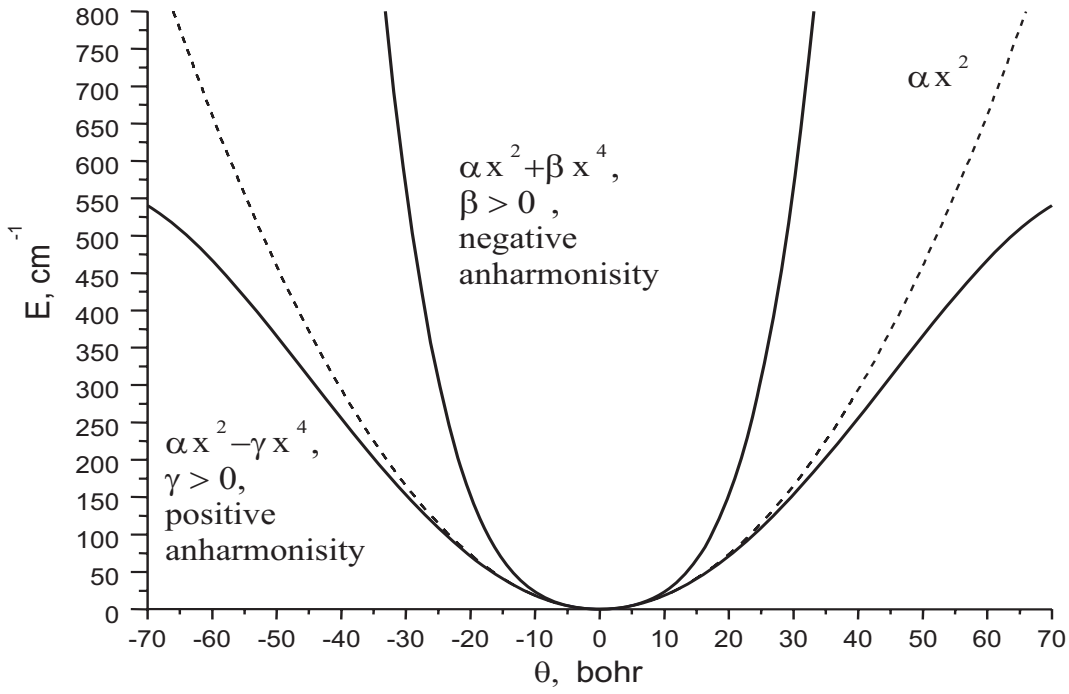

Figure IV.1: Illustration of positive and negative anharmonicities.

When one or more hydrogen atoms are substituted by halogens, the interaction of the lone pairs of the latter with the unpaired electron changes the bonding considerably: the carbon-halogen bonds contract and the corresponding force constants increase [10,36,37,116,225], some radicals assume pyramidal structures [36,37], etc (see Ref. [115] for a summary of the spectroscopic data). Recently, in collaboration with Reisler and coworkers, we have analyzed [63, 145] the bonding in the ground and electronically excited states of CH_2X (X=F,Cl) radicals: our *ab initio* calculations have shown [145] that a $\frac{1}{2}$ (n-p)-π bond forms between the chlorine and carbon atoms in CH_2Cl, whereas in CH_2F no significant electron delocalization is obtained

because of the much larger difference in the electronegativities of carbon and fluorine. This chapter demonstrates that halogen substitution also increases dramatically the anharmonicity of the OPLA mode.

Electronic structure calculations of halogen-substituted methyl radicals are difficult [19, 20, 129, 149, 176]. The ground state equilibrium geometries and frequencies of well-behaved molecules are usually reproduced accurately by high-level *ab initio* calculations, e.g., CCSD [192] and CCSD(T) [193]. However, in the case of halogen-substituted methyl radicals, the discrepancy between theory and experiment is alarmingly large: while theory predicts non-planar structures [19, 20, 129, 149], the experiments consistently yield planar geometries with well defined minima [68, 69, 112, 177, 211, 226]. For example, the calculated equilibrium geometry of the CH_2F radical deviates from the experimentally determined [69, 112, 177] planar structure by 30^o [19, 20, 129], and the calculated harmonic frequency of the umbrella mode is twice higher than the experimental value of the ω_{01} transition [69, 112]. In the case of CH_2Cl, the situation is reversed: the calculated harmonic frequency is twice *lower* than the experimental ω_{01} [10, 116].

The main purpose of this study has been to identify the origin of this large discrepancy, e.g., a failure of *ab initio* theory, an erroneous interpretation of the experiment, or unexpected subtleties in the electronic structure of these seemingly simple species. Indeed, the results of *ab initio* calculations for open-shell species have to be scrutinized carefully; in addition to the obvious observation that the requirements for the one-particle basis set are higher than for closed shell molecules (due to the more

diffuse nature of the unpaired electron), the doublet radicals are known to exhibit artifactual spatial symmetry breaking [55], which often results in anomalous vibrational frequencies and incorrect structures [4, 17, 49–51, 70, 110, 114, 122, 163, 234, 254].

We have found that the potential energy surfaces of CH_2X and CH_3 radicals are described accurately by CCSD(T) theory, and that the source of the discrepancy mentioned above is in the anomalously large anharmonicity in the OPLA mode, which is roughly equal to the harmonic frequency. Density functional theory (DFT) [186] with B3LYP exchange-correlation functional [237] yields similar results. The good performance of DFT/B3LYP is in agreement with recent benchmark studies of the equilibrium properties of doublet radicals [33, 46, 219].

There are numerous examples of highly anharmonic systems, especially among van der Waals clusters. In the extreme case of weekly interacting He atoms, the zero-point energy is so high that the vibrational wave function is delocalized over several minima of the potential energy surface and, therefore, bears no resemblance to localized harmonic wave functions [109]. In the less dramatic case of Ar clusters, the anharmonic corrections change the values of the fundamental transitions by 10-25 % of the corresponding harmonic frequencies [119]. Large anharmonicities, i.e., up to 100%, have been reported for the *inter*-molecular modes in water clusters [120]. However, the anharmonicities of *intra*-molecular vibrations are usually much smaller: 1-5 percent is a typical value [14, 22, 23, 40, 41, 82, 83, 159, 187, 219, 220]. In this context, the anharmonicities of the OPLA motion in the halogen-substituted methyl radicals are exceptionally large.

The chapter is organized as follows: Sec. IV.2 describes the theoretical model, Sec. IV.3.1 outlines the computational details, Sec. IV.3.2, IV.3.3, and IV.3.4 present the calculated equilibrium structures and vibrational spectra. Our final remarks and conclusions are given in Sec. IV.4.

IV.2 Theory

In very small systems, where it is possible to obtain a nearly global analytic fit of the multi-dimensional surface, the vibrational problem can be solved with very high accuracy [220]. In polyatomic systems, the moderate anharmonicity can be accounted for by calculating higher, i.e., third and fourth, derivatives with subsequent second-order perturbative theoretical treatment of the fundamental vibrational frequencies [14, 22, 23, 82, 83, 159, 187, 236]. In order to treat systems with larger anharmonicities, the vibrational self-consistent field (VSCF) method can be applied [30, 31, 86, 87]. The approximation recently proposed by Chaban and Gerber for multi-dimensional integral evaluation has enabled the application of the VSCF method to very large systems [40, 41]. Below we outline a less general approach, which can be employed to calculate the vibrational wave functions for OPLA motions in CH_2X radicals. A similar strategy has been employed by Johnson and Hudgens in their calculations of anharmonic effects in the CH_2OH radical [118].

For an M-atomic system, it is customary to use normal coordinates $\{Q_i\}_{i=1}^{N}$ (where $N = 3M - 6$ for a non-linear molecule). The non-unitary transformations

between Cartesian ($\{X_i\}_{i=1}^{3M}$) and normal ($\{Q_i\}_{i=1}^{N}$) coordinates are defined as follows:

$$Q_i = \sum_{j=1}^{3M} R_{ij} X_j \tag{IV.1}$$

$$X_i = \sum_{j=1}^{N} L_{ij} Q_j \tag{IV.2}$$

$$RL = I, \tag{IV.3}$$

where I is an $N \times N$ unit matrix, $I_{ij} = \delta_{ij}$. The transformation matrices R ($N \times 3M$) and L ($3M \times N$) are found by solving the normal mode problem:

$$UL = TL\Lambda, \quad \Lambda_{ij} = \delta_{ij}\omega_i^2 \tag{IV.4}$$

$$L^+ TL = I \tag{IV.5}$$

$$R = L^+ T, \tag{IV.6}$$

where T is a diagonal matrix composed of atomic masses, ω_i is the vibrational frequency of mode i, and U is the Hessian matrix evaluated at the equilibrium geometry $\{X_i^{eq}\}$:

$$U_{ij} = \frac{\partial^2 V(X_1^{eq}, \ldots, X_{3M}^{eq})}{\partial X_i \partial X_j} \tag{IV.7}$$

In normal coordinates, the Schrödinger equation for the N-dimensional vibrational wave function $\Psi(Q_1, \ldots, Q_N)$ reads:

$$\left(-\frac{1}{2} \sum_{i=1}^{N} \frac{\partial^2}{\partial Q_i^2} + V(Q_1, \ldots, Q_N) \right) \Psi_n(Q_1, \ldots, Q_N) = E_n \Psi_n(Q_1, \ldots, Q_N), \tag{IV.8}$$

where $V(Q_1, \ldots, Q_N)$ is the full potential energy surface, and atomic masses have been absorbed into the transformation R from Eq. (IV.1). In the spirit of the VSCF approximation, we employ a separable ansatz for the wave function:

$$\Psi_n(Q_1, \ldots, Q_N) = \xi_{n'}(\theta) \cdot \Phi_{n''}(Q_2, \ldots, Q_N), \tag{IV.9}$$

where $\theta \equiv Q_1$ is the normal coordinate of the OPLA mode. The wave functions $\xi_{n'}(\theta)$ and $\Phi_{n''}(Q_2, \ldots, Q_N)$ are defined by the two coupled equations:

$$\left(-\frac{1}{2} \frac{\partial^2}{\partial \theta^2} + V_\Phi(\theta) \right) \xi_{n'}(\theta) = \epsilon_{n'} \xi_{n'}(\theta) \tag{IV.10}$$

$$\left(-\frac{1}{2} \sum_{i=2}^{N} \frac{\partial^2}{\partial Q_i^2} + V_\xi(Q_2, \ldots, Q_N) \right) \Phi_{n''}(Q_2, \ldots, Q_N) = = \epsilon_{n''} \Phi_{n''}(Q_2, \ldots, Q_N), \tag{IV.11}$$

where $V_\Phi(\theta)$ and $V_\xi(Q_2, \ldots, Q_N)$ are the mean-field potentials:

$$V_\Phi(\theta) = \langle \Phi(Q_2, \ldots, Q_N) | V(\theta, Q_2, \ldots, Q_N) | \Phi(Q_2, \ldots, Q_N) \rangle_{Q_2, \ldots, Q_N} \tag{IV.12}$$

$$V_\xi(Q_2, \ldots, Q_N) = \langle \xi(\theta) | V(\theta, Q_2, \ldots, Q_N) | \xi(\theta) \rangle_\theta \tag{IV.13}$$

Since we are interested in the OPLA fundamental only (i.e., $n' = 0, 1$), all the other vibrational degrees of freedom can be assumed to be in their ground state. That is why only the lowest $\Phi_{n''}(Q_2, \ldots, Q_N)$ is needed, i.e., $n'' = 0$.

At this point, we introduce additional approximations to the mean-field separation of the OPLA motion. Instead of solving Eqns. (IV.10-IV.13) self-consistently, we assume that the wave function $\Phi(Q_2, \ldots, Q_N)$ has the following simple form:

$$\Phi(Q_2, \ldots, Q_N) = \prod_{i=2}^{N} \delta(Q_i - Q_i^{opt}), \tag{IV.14}$$

where δ stands for the δ-function, and the choice of optimal coordinates $\{Q_i^{opt}\}_{i=2}^N$ is described below. With this approximation, the effective potential for the OPLA motion assumes the following form:

$$V_\Phi(\theta) \approx V(\theta, Q_2^{opt}, \ldots, Q_N^{opt}) \tag{IV.15}$$

We consider two different choices of parameters $\{Q_i^{opt}\}_{i=2}^N$ from Eqns. (IV.14,IV.15). The first model completely neglects the interaction between modes, and thus assumes that when atoms move along the OPLA coordinate, all the other coordinates do not change, i.e. $Q_i^{opt} \equiv Q_i^{eq}$:

$$V_\Phi(\theta) \approx V(\theta, Q_2^{eq}, Q_3^{eq}, \ldots, Q_N^{eq}) \tag{IV.16}$$

Drawing from the analogy with the electronic structure problem, we call Eq. (IV.16) the *diabatic approximation*.

Alternatively, one can consider a model, which assumes that the motions of all the other coordinates are much faster than that of the OPLA vibration. In this model, all the other degrees of freedom can simultaneously adjust to the current value of the OPLA coordinate. Thus, $\{Q_i^{opt}\}_{i=2}^N$ are found by optimizing the potential $V(\theta, Q_2, \ldots, Q_N)$ w.r.t. $\{Q_i\}_{i=2}^N$ and at a fixed value of θ:

$$\frac{\partial V(\theta, Q_2, \ldots, Q_N)}{\partial Q_i}|_{Q_i=Q_i^{opt}} = 0, \quad i = 2, \ldots, N \tag{IV.17}$$

We call this model the *adiabatic approximation*. The low frequency of the OPLA motion, which is at least twice slower than any other vibration in these radicals, justifies the adiabatic separation of the slow and fast motions. Due to symmetry considerations, the diabatic and adiabatic OPLA effective potentials have an identical harmonic part (see Appendix III).

Our results show that the approximate account of the interaction between the modes in the adiabatic model yields a better agreement with the experiment. However, even the oversimplified diabatic model is capable of describing the anharmonicity in a qualitatively correct way.

IV.3 Results and discussion

IV.3.1 Computational details

We report results obtained with the CCSD(T) [193] and DFT/B3LYP [186, 237] methods. All calculations employ the 6-311(+,+)G(3df,3pd) basis set, derived from the polarized split-valence 6-311G(d,p) basis [133, 162] by augmenting it by additional sets of polarization and diffuse functions [45, 80]. We find that the heavy polarization is crucial for the correct description of the equilibrium structures of halogen substituted methyl radicals: for example, CH_2Cl becomes pyramidal in smaller basis sets.

The CCSD(T) harmonic frequencies are calculated by using second analytic derivatives [235], at the geometries optimized with the CCSD(T) method. Finite differences of analytically computed first order derivatives are used to calculate the harmonic frequencies with the DFT/B3LYP method [128], at the geometries optimized with DFT/B3LYP.

The optimized geometries of the CH_2X radicals are given in Table IV.1.

The rotational constants calculated at these equilibrium geometries are summarized in Table IV.2.

Since the calculated rotational constants are not vibrationally averaged, the comparison with experiment is not straightforward.

The procedure for calculating the one-dimensional diabatic and adiabatic effective potentials [Eqns. (IV.15)-(IV.17)] is outlined below. First, geometry optimization

Table IV.1: Calculated ground state geometries of CH_2X (X=Cl,F,H) radicals.

	Symm.	r_{CH}, Å	r_{CX}, Å	α_{HCH}	Θ^b	E_{nuc}	E_{tot}
CCSD(T)/6-311(+,+)G(3df,3pd)[a]							
CH_2Cl (X^2B_1)	C_{2v}	1.076	1.691	124.17	180	45.620 937	-499.007 703
CH_2F (X^2A')	C_s	1.079	1.335	124.11	153.11	32.246 535	-138.935 120
CH_2F (X^2B_1)	C_{2v}	1.076	1.332	127.60	180	32.274 065	-138.934 617
CH_3 (X^2A_2'')	D_{3h}	1.0783		120	180	9.683 711	-39.783 994
DFT(B3LYP)/6-311(+,+)G(3df,3pd)[a]							
CH_2Cl (X^2B_1)	C_{2v}	1.076	1.698	124.41	180	45.479 968	-499.490 818
CH_2F (X^2A')	C_s	1.079	1.338	125.13	156.70	32.180 494	-139.128 583
CH_2F (X^2B_1)	C_{2v}	1.076	1.336	127.79	180	32.201 855	-139.128 331
CH_3 (X^2A_2'')	D_{3h}	1.0779		120	180	9.687 270	-39.858 366

[a] Pure angular momentum spherical harmonics are used.

[b] Dihedral HCXH angle.

Table IV.2: Ground state rotational constants (MHz) for CH_2X radicals (X=Cl, F, H)[a].

Method	A	B	C
		CH_2Cl	
CCSD(T)/C_{2v}	277 359.	16 016.398	15 142.006
DFT(B3LYP)/C_{2v}	277 071.	15 899.166	15 036.336
Exp. [68]	274 380. $\pm$ 78	15 948.028 2 $\pm$ 126	15 057.044 3 $\pm$ 123
		CH_2F	
CCSD(T)/C_{2v}	268 993.	31 177.081	27 938.892
CCSD(T)/C_s	264 292.	31 102.495	28 074.005
DFT(B3LYP)/C_{2v}	268 352.	31 019.521	27 805.420
DFT(B3LYP)/C_s	264 835.	30 962.334	27 904.259
Exp. [69]	265 200.	30 948.322(27)	27 727.773(27)
		CH_3	
CCSD(T)/D_{3h}	287 526.470	287 526.470	143 763.235
DFT(B3LYP)/D_{3h}	287 738.378	287 738.163	143 869.135
Exp. [256]	287 145(5)	287 145(5)	142 165(20)

[a] Theoretical values are calculated at the equilibrium geometries and therefore do not include vibrational averaging.

with a C_{2v} symmetry constraint and normal mode analysis are performed at each level of theory. This yields the transformation matrices R and L from the Eqs. (IV.1)-(IV.2). Second, the equilibrium values of the normal coordinates, $\{Q^{eq}\}$, are calculated from the equilibrium values of the Cartesian coordinates, $\{X^{eq}\}$, by using Eq. (IV.1). Finally, a grid of θ-values and the corresponding optimal values of the other coordinates, $\{Q_i^{opt}\}_{i=2}^{N}$, are generated and the total energies are computed at these points.

For the diabatic effective potentials, a non-uniform grid of displacements along θ (i.e. the OPLA normal coordinate) is generated. All the other normal coordinates are frozen at their equilibrium values. The corresponding Cartesian geometries are

computed by using Eq. (IV.2). To calculate the adiabatic effective potentials, a grid of values for the torsion angle is generated and the geometry is optimized w.r.t. all the other internal coordinates at each value of the torsion angle. By using the transformation matrix R from Eq. (IV.1), these Cartesian coordinates are transformed to the normal coordinates. This yields values of the normal coordinate θ which correspond to a fixed torsion angle, and optimum values of all the other internal coordinates. This procedure is equivalent to a constrained geometry optimization in the normal coordinates, with the OPLA normal coordinate being frozen at a certain value of θ.

The energy points calculated in this way are then used to determine the parameters of the following analytical form of the effective potential:

$$V(\theta) = a_2\theta^2 + a_4\theta^4 + a_6\theta^6 + a_8\theta^8 \tag{IV.18}$$

The analytical fit of the potential allows extrapolation of the potential function beyond the range in which the energy points are calculated. We have found that powers of θ higher than fourth are necessary for an accurate fit, e.g., in order to reproduce the correct second derivative of the effective potentials. The harmonic frequencies of our effective OPLA potentials parameterized by Eq. (IV.18) agree within 1 cm^{-1} with the harmonic frequencies calculated by solving the normal mode problem at the optimized geometry.

Anharmonic frequencies, ω_{01}, are calculated by numerically solving the one-dimensional Schrödinger equation (IV.10) with potentials (IV.18) by using the program LEVEL [143].

IV.3.2 CH_2Cl

The calculated harmonic frequencies of the CH_2Cl radical are summarized in Table IV.3.

The deviation of the calculated harmonic frequencies from the corresponding experimental values does not exceed 5% for the CCl stretch and CH_2 scissors. However the calculated value of the OPLA harmonic frequency is twice lower than the experimental value of ω_{01}. The agreement between the calculated and the experimental values seems to be better for DFT/B3LYP than for the reliable and accurate CCSD(T) method.

The parameters of the analytical fit of the diabatic and adiabatic effective potentials (see Sec. IV.2) are given in Table IV.4.

The CCSD(T) adiabatic effective potential is shown in Fig. IV.2, along with the corresponding harmonic potential (dashed line).

Fig. IV.2 illustrates the strikingly large negative anharmonicity of the OPLA vibrational mode of CH_2Cl. The calculated value of the 0-1 OPLA transition is 422 cm^{-1}, more than twice higher than the harmonic frequency of 168 cm^{-1}. The former is in a good agreement with the experimental value of 402 cm^{-1}. The DFT/B3LYP

Table IV.3: CH_2Cl. Calculated harmonic vibrational frequencies ω_e and experimental values ω_{01}, cm^{-1}. The relative differences, $\Delta = \frac{(\omega_e - \omega_{01})}{\omega_{01}} \cdot 100\%$, are shown in parentheses.

Method	CCl stretch	CH_2 scissors	OPLA	CH_2 rock	CH_2 s-stretch	CH_2 a-stretch
	a_1	a_1	b_1	b_2	a_1	b_2
CCSD(T)	868 (5%)	1434 (3%)	168 (58%)	1004	3179	3335
DFT	835 (1%)	1415 (2%)	229 (43%)	997	3169	3320
Exp.	827 [10, 116]	1391 [10]	402 [10, 116]			

Table IV.4: CH_2Cl. Parameters (10^{-6} a.u.) of the analytical fit (IV.18) of the OPLA effective potentials.

Method	a_2	a_4	a_6	a_8
Diabatic potential				
CCSD(T)	0.29518	0.00305444	$-4.13673\cdot10^{-7}$	$3.3010\cdot10^{-11}$
DFT	0.55895	0.00292334	$-3.86651\cdot10^{-7}$	$2.8935\cdot10^{-11}$
Adiabatic potential				
CCSD(T)	0.29443	0.00118134	$-3.6527\cdot10^{-8}$	$5.750\cdot10^{-12}$
DFT	0.54487	0.00109229	$-3.2434\cdot10^{-8}$	$3.480\cdot10^{-12}$

adiabatic effective potential yields a similar value (434 cm^{-1}). Therefore, both models give anharmonic corrections to the OPLA mode of CH_2Cl, which are roughly equal in magnitude to the harmonic frequency. The OPLA fundamental transition energy calculated by CCSD(T) deviates from the experiment by 5%, and the DFT/B3LYP value by 8 %. The amplitude of the zero point motion for the OPLA mode is rather large: the turning points of the anharmonic potential from Fig. IV.2 correspond to a 26^o deviation from a planar structure.

As expected, the diabatic effective potentials are too steep because the relaxation in the other coordinates is neglected. Thus, the diabatic model overestimates the anharmonicities. The values of the diabatic ω_{01} are 543 and 554 cm^{-1} for the CCSD(T) and DFT/B3LYP methods, respectively. Nevertheless, even this oversimplified model produces a better estimate for ω_{01} than the harmonic model.

It is interesting to compare our OPLA effective potential with that reconstructed by Andrews and Smith [10]. Their anharmonic quartic potential has been parameterized to reproduce the OPLA vibrational frequencies of the deuterated CH_2Cl radicals.

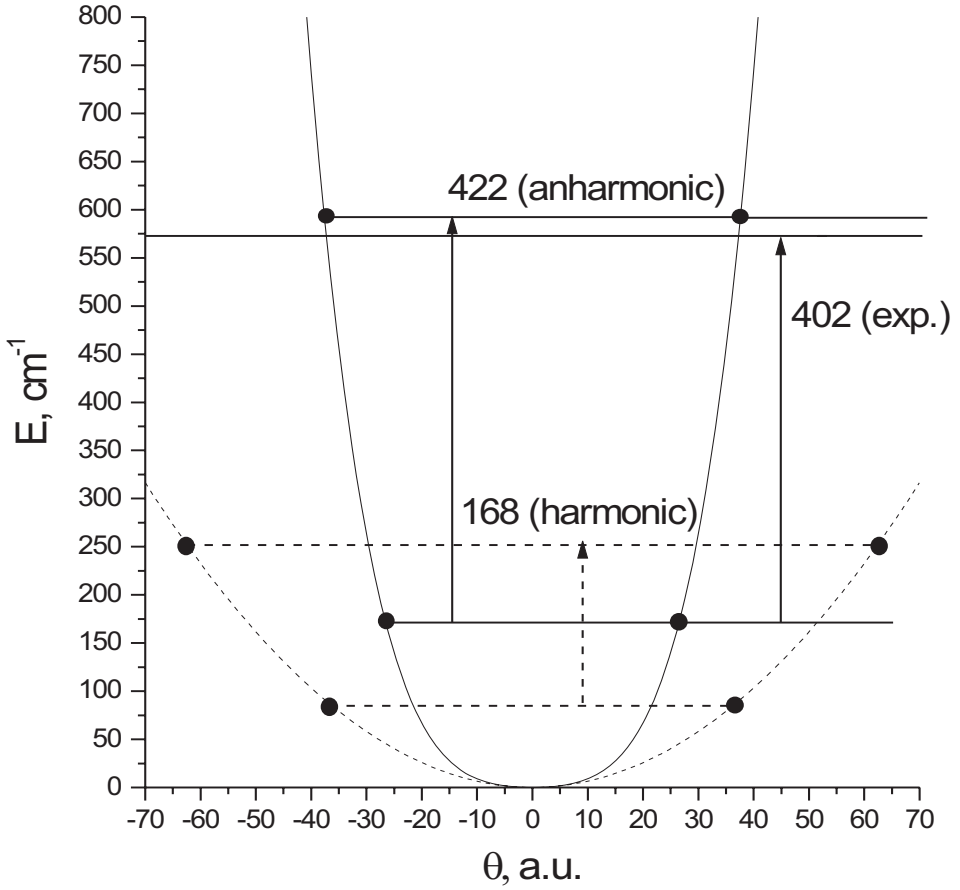

Figure IV.2: Harmonic (dashed line) and anharmonic (solid line) OPLA adiabatic effective potentials for the CH_2Cl radical [CCSD(T)/6-311(+,+)G(3df, 3pd)]. The positions of the zero and first excited vibrational levels are shown by horizontal lines. The calculated and experimental values for the fundamental transition are shown by vertical arrows.

The harmonic frequency calculated with their potential is 262 cm^{-1}. This value is 94 cm^{-1} above the CCSD(T) harmonic frequency of 168 cm^{-1}. This large discrepancy is due to the absence of higher powers of θ in their effective potential.

IV.3.3 CH_2F

The calculated harmonic frequencies for the CH_2F radical are presented in Table IV.5.

Table IV.5: CH_2F. Calculated harmonic vibrational frequencies ω_e and experimental values ω_{01}, cm^{-1}. The relative differences, $\Delta = \frac{(\omega_e - \omega_{01})}{\omega_{01}} \cdot 100\%$, are shown in parentheses.

Method	CF stretch	CH_2 scissors	OPLA	CH_2 rock	CH_2 s-stretch	CH_2 a-stretch
	a_1	a_1	b_1	b_2	a_1	b_2
CCSD(T)/C_{2v}	1208 (3%)	1478	437i	1167	3173	3347
DFT/C_{2v}	1184 (1%)	1439	361i	1130	3120	3290
CCSD(T)/C_s	1199 (2%)	1482	585 (95%)	1185	3142	3302
DFT/C_s	1177 (0.6%)	1440	482 (61%)	1142	3093	3254
Exp.	1170 [194, 255]	1515 [194]	300±30 [69, 112]			

Table IV.6: CH_2F. Parameters (10^{-6} a.u.) of the analytical fit (IV.18) of the OPLA effective potentials.

Method	a_2	a_4	a_6	a_8
Diabatic potential				
CCSD(T)	-1.98828	0.00372125	$-5.58976\cdot10^{-7}$	$5.33584\cdot10^{-11}$
DFT	-1.31826	0.00336544	$-4.55563\cdot10^{-7}$	$3.45819\cdot10^{-11}$
Adiabatic potential				
CCSD(T)	-1.98633	0.00205917	$-2.05565\cdot10^{-7}$	$2.8313\cdot10^{-11}$
DFT	-1.31281	0.00175463	$-1.22598\cdot10^{-7}$	$1.1967\cdot10^{-11}$

For this radical, the OPLA harmonic frequency calculated at the optimized equilibrium geometry (C_s structure) is about twice higher than the experimental ω_{01} for the OPLA fundamental transition (Hudgens *et al.* recommend 260$\pm$30 cm^{-1} [112], and Endo *et. al.* recommend 300$\pm$30 cm^{-1} [69]). This situation is exactly the reverse of that in the CH_2Cl radical, where the harmonic OPLA frequency is twice lower than the experimental ω_{01}. Similarly to CH_2Cl, the discrepancy between the theoretical harmonic frequencies and the experimental value of ω_{01} is larger for CCSD(T) than for DFT.

The parameters of the analytical fit of the diabatic and adiabatic effective potentials (see Sec. IV.2) are given in Table IV.6.

The CCSD(T) adiabatic effective potential is shown in Fig. IV.3, as well as the corresponding harmonic potential.

As shown in Fig. IV.3, the zero-point vibrational level is 57 cm^{-1} above the barrier between the two non-planar (C_s) minima. The amplitude of the zero-point OPLA

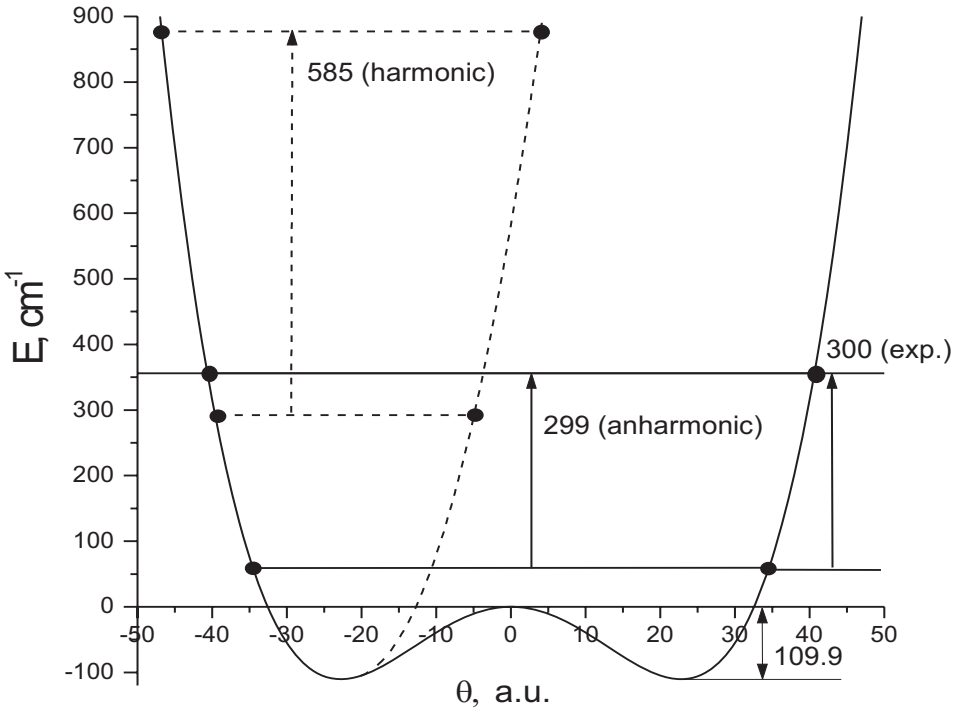

Figure IV.3: Anharmonic (solid line) OPLA adiabatic effective potential for the CH_2F radical [CCSD(T)/6-311(+,+)G(3df,3pd)]. The dashed curve represents the harmonic part of the potential at the optimized non-planar (C_s) geometry. The corresponding harmonic frequency is also shown. The negative curvature at the planar (C_{2v}) geometry (i.e., at the barrier) yields the imaginary frequency of 437i cm^{-1}. The positions of the zero and first excited levels are shown by horizontal lines. The calculated and experimental values of the OPLA fundamental transition are shown by vertical arrows.

vibration of CH_2F is very large: the turning points of the effective potential (Fig. IV.3) correspond to the 38^o deviation from the planar structure (vs 26^o in CH_2Cl).

These results reconcile the theoretical predictions of a non-planar equilibrium structure (with a deviation from planarity of about 27^o) with the experimental results (microwave spectroscopy) which strongly support a C_{2v} symmetry [69, 177]. Planar or near-planar ($< 5^o$ deviation from planarity) geometry has also been suggested by

the electron spin-resonance (ESR) study of Fessenden and Schuler [73]. A double-well potential with two strongly non-planar minima has been ruled out as inconsistent with the measured value of the carbon hyperfine coupling constant [73]: even with the zero-point energy being above the barrier, the large-amplitude zero-point vibrations in the double well potential were estimated to cause a large increase in the vibrationally averaged carbon hyperfine coupling constant (thus revealing the non-planar equilibrium structure of the radical). However, that estimate was based on the complete orbital following model [7] ,which was shown to fail in similar circumstances, i.e. for the CH_3 radical [209]. To check the validity of the complete orbital following assumption, we performed Natural Bond Orbital analysis [88] of the CH_2F density at the optimized (strongly non-planar) geometry. We find that the unpaired electron has only 6 % s-character, whereas the complete orbital following model predicts about 14% s-character [7] , [8] .This demonstrates incomplete orbital following and reconciles the small value of the carbon hyperfine coupling constant [73] with

[7]The complete orbital following model assumes that the s-character of the unpaired electron is directly proportional to the OPLA angle Θ, as suggested by the hybridization theory. That is, from the orthogonality considerations for the hybrid orbital, the s-character of the unpaired electron is estimated to be $2 \cdot tan^2\Theta$. Since the hyperfine interactions are much stronger for s-electrons (contrarily to the higher angular momentum, s-orbitals do not have a node on the nucleus), the angular dependence of the carbon hyperfine coupling constant a_C is assumed to have the following form: $a_C(\Theta) = a_C(0) + A \cdot 2 \cdot tan^2\Theta$, where $A \sim 1190\ G$ is the contribution from an electron on 2s carbon orbital. Thus, complete orbital following predicts a strong increase in the a_C at the non-planar geometries. The incomplete orbital following means that the s-character of the hybrid orbital containing the unpaired electron cannot be derived from the hybridization theory and, therefore, makes the dependence $a_C(\Theta)$ less dramatic.

[8]The larger incompleteness of the orbital following in CH_2F (as compared to the orbital following in CH_3) can be readily rationalized: the electrostatic attraction of the positively charged hydrogens to the negatively charged fluorine results in the additional stabilization of the non-planar structure. Thus, the relative role of the orbital hybridization is smaller in CH_2F than in CH_3.

the large amplitude zero-point OPLA motion in the double-well potential shown in Fig. IV.3.

The calculated value of ω_{01}, 299 cm^{-1} [CCSD(T), adiabatic model] is in the excellent agreement with the experimental value of about 300 cm^{-1} [69, 112](Fig. IV.3). The adiabatic DFT potential results in a slightly higher value of 332 cm^{-1}. Similarly to the CH_2Cl case, the diabatic model overestimates the frequencies. A better performance of the adiabatic separation of the OPLA motion in CH_2F has been anticipated, because of the larger difference in frequencies between the OPLA vibration and all the other modes.

For CH_2F, the difference between the harmonic and anharmonic wave functions is even more dramatic than for CH_2Cl. The harmonic frequency is either too high (if calculated at the optimized C_s geometry), or imaginary (if calculated at the optimized C_{2v} geometry). These frequencies reflect the large local curvature at the C_s stationary point or the negative curvature at the barrier, but have no relation to the real vibrational levels of CH_2F.

IV.3.4 CH_3

Table IV.7 summarizes the calculated CH_3 harmonic frequencies and the experimental values of its fundamental transitions.

For CH_3, the discrepancy between the calculated harmonic OPLA frequencies and the experimental value of the transition energy ω_{01} is not as remarkable as it is for CH_2Cl and CH_2F. Nevertheless, the relative difference is still at least four times

Table IV.7: CH_3. Calculated harmonic vibrational frequencies ω_e and experimental values ω_{01}, cm^{-1}. The relative differences, $\Delta = \frac{(\omega_e - \omega_{01})}{\omega_{01}} \cdot 100\%$, are shown in parentheses.

Method	CH stretch	CH_2 scissors & rock	OPLA	CH_2 s,a-stretch
	a_1'	e'	a_2''	e'
CCSD(T)	3104 (3%)	1424 (2%)	507 (16%)	3293 (4%)
DFT	3109 (3%)	1408 (0.4%)	542 (11%)	3287 (4%)
Exp.	3004 [108, 123, 246, 257]	1402 [174, 241]	607 [243, 256]	3161 [7, 56, 174, 185, 227, 244]

Table IV.8: CH_3. Parameters (10^{-6} a.u.) of the analytical fit (IV.18) of the OPLA effective potentials.

Method	a_2	a_4	a_6	a_8
Diabatic potential				
CCSD(T)	2.67068	0.00252317	$-3.0602\cdot10^{-7}$	$2.468\cdot10^{-11}$
DFT	3.06987	0.00230044	$-2.1121\cdot10^{-7}$	$3.74\cdot10^{-12}$
Adiabatic potential				
CCSD(T)	2.66894	0.00151257	$-1.3727\cdot10^{-7}$	$2.243\cdot10^{-11}$
DFT	3.10764	0.00124858	$-4.33\cdot10^{-9}$	$8.17\cdot10^{-12}$

larger than for any other mode. As seen from the Table IV.7, this discrepancy is larger for CCSD(T) than for DFT (16% versus 11%). Since the molecule has been extensively studied both theoretically [28, 62, 165] and experimentally [7, 56, 108, 123, 174, 185, 199, 227, 241, 243, 244, 246, 256, 257], it is instructive to investigate how our model performs in this case.

The CCSD(T)/6-311(+,+)G(3df,3pd) harmonic OPLA frequency is 507 cm^{-1}, which is considerably lower than the harmonic frequency of 544 cm^{-1} derived from the Riveros' fit [199]. Moreover, improving the one-electron basis set further lowers the harmonic frequency, e.g., the CCSD(T)/aug-cc-pVTZ value is 497 cm^{-1} [62]. Similarly to the CH_2Cl case, we attribute this difference to the absence of higher than quartic terms in the Riveros' potential.

The parameters for the analytical fit of the diabatic and adiabatic effective potentials (see Sec. IV.2) are given in Table IV.8.

The CCSD(T) adiabatic effective potential is shown in Fig. IV.4, as well as the corresponding harmonic potential.

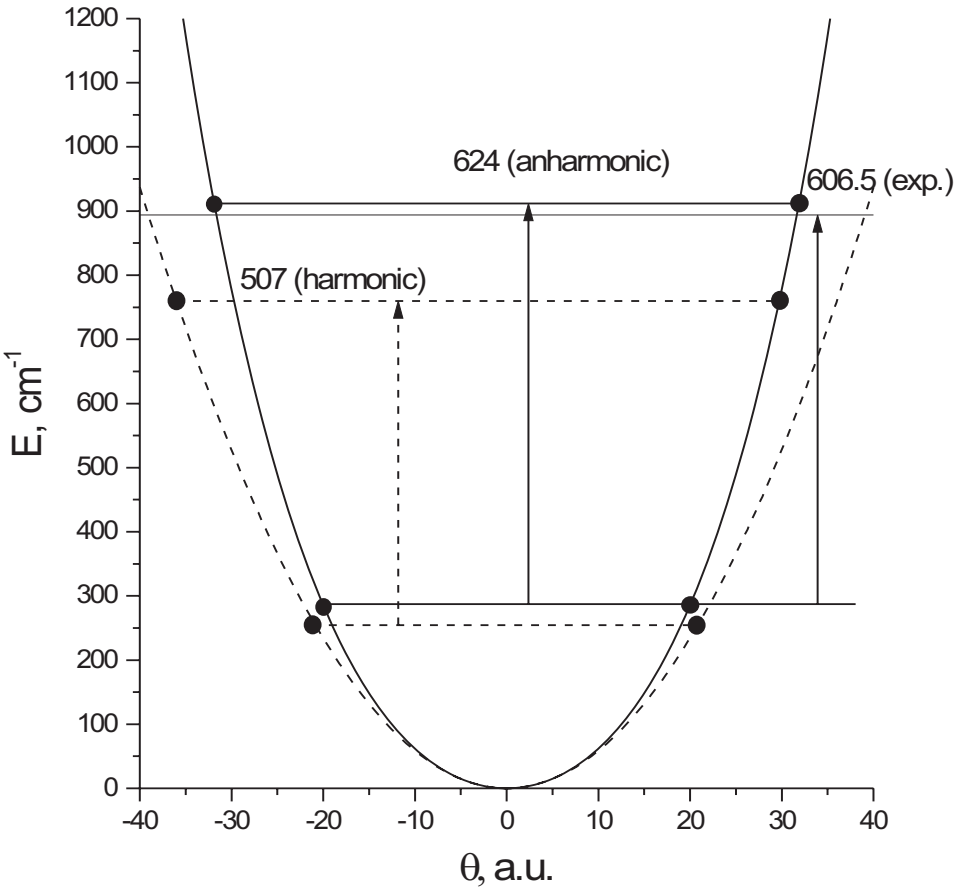

Figure IV.4: Harmonic (dashed line) and anharmonic (solid line) OPLA adiabatic effective potentials for the CH_3 radical [CCSD(T)/6-311(+,+)G(3df, 3pd)]. The positions of the zero and first excited levels are shown by horizontal lines. The calculated and experimental values for the OPLA fundamental transition are shown by vertical arrows.

The corresponding anharmonic frequency is 624 cm^{-1}. The adiabatic DFT value is 645 cm^{-1}. The deviation of the adiabatic anharmonic ω_{01} from the experiment is thus 4.5% for CCSD(T), and 6% for DFT model. As in the previous two cases, the anharmonic frequencies calculated using the diabatic effective potential overestimate the experimental transition energy by about 11% for CCSD(T), and 14% for DFT method.

Table IV.9: Calculated and the experimental values for the OPLA fundamental transition, cm^{-1}. The OPLA adiabatic and diabatic effective potentials are calculated at CCSD(T)/6-311++G(3df,3pd) level of theory.

Species	ω_e	ω_{01}^{diab}	ω_{01}^{adiab}	Exp.
CH_2Cl	168	543	422	402
CH_2F	437i	419	299	300$\pm$30
CH_3	507	672	624	607

Table IV.10: Calculated and the experimental values for the OPLA fundamental transition, cm^{-1}. The OPLA adiabatic and diabatic effective potentials are calculated at DFT(B3LYP)/6-311++G(3df,3pd) level of theory.

Species	ω_e	ω_{01}^{diab}	ω_{01}^{adiab}	Exp.
CH_2Cl	229	554	434	402
CH_2F	361i	447	332	300$\pm$30
CH_3	542	689	645	606

Even though the frequency of the OPLA motion is higher than in CH_2Cl, the amplitude of the zero-point motion in the potential shown in Fig. IV.4 is almost the same as in the case of CH_2Cl: the turning points correspond to a 25^o deviation from planarity (vs 26^o in CH_2Cl).

IV.4 Conclusions

We find large anharmonic corrections for the OPLA vibrational mode of the CH_2Cl, CH_2F, and CH_3 radicals. For these radicals, it is possible to describe the OPLA motion within a simple one-dimensional model based on the the adiabatic separation of the (slowest) OPLA mode from all the other vibrations. The OPLA vibrational frequencies of all three radicals are summarized in Tables IV.9 and IV.10.

We find that halogen substitution increases the anharmonicities dramatically, i.e., from 19 % in CH_3 up to about $\pm$ 100 % in CH_2Cl and CH_2F. The resulting frequencies of the fundamental OPLA transitions are in good agreement with the experimental values (the deviations are about 5 %, similar to the other modes). In the case of CH_2F, the large anharmonicity in the OPLA mode results in a wave function delocalized over two minima of the double well potential. This reconciles the experimentally determined planar (C_{2v}) structure with the calculated pyramidal (C_s) equilibrium geometry.

As demonstrated in Tables IV.9 and IV.10, the agreement of the CCSD(T) model with the experiment is consistently better than that of DFT. Nevertheless, DFT/B3LYP also yields reasonably accurate anharmonic potentials for the OPLA motion. This is consistent with other recent benchmark studies of radicals [33, 46].

Chapter V. Rydberg-valence interactions in $CH_2Cl \rightarrow CH_2$ + Cl photodissociation: Dependence of absorption probability on ground state vibrational excitation

A strong enhancement of absorption to the lowest $^2A_1$ state is observed for vibrationally excited chloromethyl radicals. It is demonstrated that this enhancement is due to a significant increase in both electronic and vibrational Franck-Condon factors. Electronic structure calculations of potential energy surfaces and transition dipole moments for the ground and the two lowest excited states of A_1 symmetry, the 1^2A_1 valence and 2^2A_1 Rydberg states, reveal the origin of this effect. The shelf-like shape of the 1^2A_1 PES in the Franck-Condon region and the strong dependence of the electronic transition dipole moment on C-Cl distance are responsible for the enhancement. Analysis of the shape of the electron density distribution demonstrates that Rydberg-valence interaction in the two lowest excited states causes the changes in the shape of PESs and transition dipoles with C-Cl distance.

V.1 Introduction

Photodissociation of CH_2Cl and other small polyatomic molecules provides an ideal opportunity for the study of molecular dynamics at a detailed state-to-state level [208]. As has been demonstrated in the previous two chapters, halogen-substituted small radicals exhibit several interesting phenomena, such as additional bonding due to the interaction of the unpaired electron with the lone pairs of the halogen [145], unusually large ($\pm$ 100%) OPLA mode anharmonicities caused by the unpaired electron [146], and strong Rydberg-valence interactions in excited states.

The photodissociation of CH_2Cl was investigated experimentally by Reisler and coworkers [63, 190]. Using the ion imaging technique, they concluded that Cl + CH_2 was the main channel in the wavelength region 312-214 nm. They found a broad maximum in product yield at $\sim$250 nm (4.96 eV) associated with a perpendicular electronic transition, in excellent agreement with the calculated 4.92 eV value for the vertical $1^2A_1 \leftarrow X^2\mathrm{B}_1$ excitation [145]. The valence character of the 1^2A_1 state [145] explains the observed fast dissociation [63]. With shorter excitation wavelengths (240 - 214 nm), products deriving from a parallel transition were also detected [63]. Our *ab initio* calculations [145] identified the upper state as 2^2B_1 resulting from the $\pi^*_{CCl} \leftarrow \pi_{CCl}$ promotion of the unpaired electron. The large

absorption cross-section for this transition [145, 200] is responsible for its contributions to the photodissociation at energies considerably lower than the vertical excitation energy of 6.33 eV (theoretical estimate [145], in agreement with the experimental value of 6.2 eV [200]).

The focus of this chapter is on the photodissociation on the 1^2A_1 excited state. It was observed that despite efficient vibrational and rotational cooling of CH_2Cl by carrier gases in supersonic expansion, a large fraction of the dissociation products on this state appeared with total energies exceeding the energy available to vibrationally *unexcited* radicals after photon absorption [63]. Quantitatively, the relative product yields from vibrationally excited radicals are greater than predicted based solely on the thermal "hot band" population. This suggests a significant enhancement in absorption probabilities for vibrationally excited radicals. To explain this finding, we calculated PESs and transition dipole moments along the C-Cl bond-breaking coordinate for the ground and the 1^2A_1 and 2^2A_1 excited states. We find that the shelf-like shape of the 1^2A_1 PES in the Franck-Condon region and the strong dependence of the electronic transition dipole upon the C-Cl distance are responsible for the enhancement. We conclude that it is the Rydberg-valence interaction between the two lowest excited states that causes the changes in the shape of PESs and transition dipoles with C-Cl distance. Such Rydberg-valence interactions are common in bond breaking [202], especially in radicals, which often have low-lying valence and Rydberg states [145].

The equilibrium properties of the two lowest $^2A_1$ states are also characterized. The shapes of the PESs and the changes in vibrational frequencies are explained in terms of a molecular orbital picture developed in our previous work [145].

The structure of the chapter is as follows. Sec. V.2 presents the experimental evidence for the enhancement in product intensities from "hot bands", and demonstrates that it can only be explained by a considerable increase in Franck-Condon factors for vibrationally excited CH_2Cl. In Sec. V.3, results of *ab initio* calculations are summarized and discussed. Section V.3.1 describes technical details of the calculations; Sec. V.3.2 presents our analysis of the equilibrium structures, vibrational frequencies, and PESs of the ground and the two lowest excited states of CH_2Cl; and Sec. V.3.3 discusses the shapes of the PESs in terms of Rydberg-valence interaction. Based on these results, Sec. V.4 explains the observed enhancement from "hot bands". Our final remarks and conclusions are given in Sec. V.5.

V.2 Experimental results

Experimental results on the photodissociation of CH_2Cl following excitation at selected wavelengths in the region 214-312 nm were reported elsewhere [63, 190]. The CH_2Cl radical was produced in a molecular beam by using pulsed pyrolysis. The gas mixture, 0.5-1% of CH_2ClI in 2 atm of He, Ar, or different mixtures of CF_4:He, was expanded through a pulsed supersonic nozzle with an attached SiC tube [125]. The tube was heated to a temperature of T≈1800 K, which resulted in the fission of I

atoms from CH_2ClI with an efficiency greater than 50%. After supersonic expansion, the radicals were photodissociated with laser radiation. The photofragments were detected by resonance enhanced multiphoton ionization (REMPI), and their velocity and angular distributions were determined using the velocity map ion imaging technique, as described before [59, 64].

Cl and CH_2 fragments are the major products throughout the excitation wavelength region 214-312 nm:

$$CH_2Cl \rightarrow Cl + CH_2, \quad \Delta H = 391 \pm 5 \text{ kJ} \cdot \text{mol}^{-1} \tag{V.1}$$

In the region 247-312 nm CH_2 (X^3B_1) and Cl ($^2P_{1/2,3/2}$) products derive predominantly from dissociation via the perpendicular (β=-0.7) electronic transition $1^2A_1 \leftarrow X^2B_1$. At wavelengths shorter than 240 nm, the Cl ($^2P_{1/2,3/2}$) products exhibit angular distributions that are characteristic of a parallel transition ($2^2B_1 \leftarrow X^2B_1$; β=1.2), and $CH_2(\tilde{a}^1A_1)$ is the main co-fragment.

The measured velocity distributions were converted into translational energy distributions of the products (see Fig. V.1).

The widths of the energy distributions for Cl correspond to a range of internal excitations in the CH_2 co-fragment. The maximum allowed translational energy for ground state reactants, E_t^{max} is given by:

$$E_t^{max} = h\nu - D_0 \tag{V.2}$$

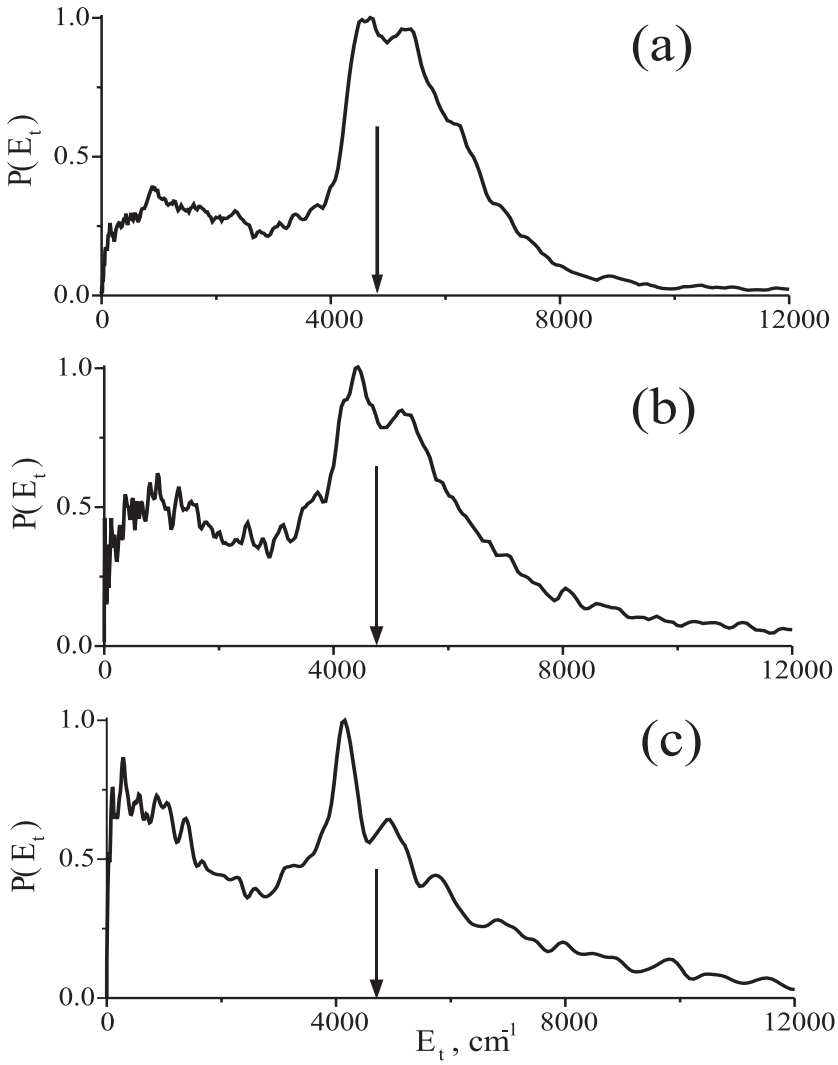

Figure V.1: CH_2Cl photodissociation at 266 nm (37,594 cm^{-1}) using (a) He, (b) CF_4:He (1:7), and (c) Ar carrier gases. $Cl(^2P_{3/2})$ signals are plotted as a function of the total c.m. photofragment translational energy, E_t. The arrows indicate the maximum translational energy allowed for dissociation from the ground vibrational state to $Cl(^2P_{3/2})$ + $CH_2(X^3B_1)$.

where D_0 is the dissociation threshold. The complete energy balance for CH_2Cl dissociation is given by:

$$E_{int}(CH_2Cl) + h\nu = D_0 + E_t + E_{int}(CH_2) + E_{int}(Cl) \qquad \text{(V.3)}$$

where $h\nu$ is the photon energy, D_0 is the dissociation threshold of the CH_2Cl radical, and $E_{int}(CH_2Cl)$, $E_{int}(CH_2)$, and $E_{int}(Cl)$ are the internal energies (rotational, vibrational, and electronic) of the respective reactant and fragments. The value of D_0 = 391 $\pm$ 5 kJ/mol (32,690 $\pm$ 420 cm^{-1}), was derived from the enthalpies of formation of CH_2Cl, CH_2, and Cl [2, 58, 107, 150, 212, 213, 248, 252]. In experiments carried out with He carrier gas, it was found that in the excitation range 214-240 nm (parallel transition) the measured highest translational energy is close to E_t^{max}, while for photolysis via the perpendicular transition (247-312 nm) large fractions of the products have translational energies exceeding E_t^{max} (see Fig. V.1a).

Based on previous work [34, 171], effective rotational cooling of CH_2Cl radicals is expected in supersonic expansion combined with the pyrolysis source, but He is not efficient in relaxing vibrational excitations. Typically in supersonic cooling T_{vib} = 30-60 K and T_{rot} = 2-10 K are achieved. Considering the high initial temperature of the radical produced in the 1800 K pyrolysis one may assume a somewhat higher final vibrational temperature of the radical (few hundreds instead of few tens of degrees). Thus, the high energy tails of the observed product distributions can be attributed to dissociation of vibrationally excited ("hot") CH_2Cl radicals. Another possible source of fragments with excess kinetic energy, two-photon dissociation of CH_2Cl, was ruled out before [63].

In order to confirm that products with kinetic energy in excess of E_t^{max} result from dissociation of vibrationally excited radicals, experiments were carried out with Ar and He/CF_4 mixtures as carrier gases. Fig. V.1c shows the energy distribution

of Cl($^2P_{3/2}$) obtained from the dissociation of CH_2Cl at 266 nm in Ar carrier gas and detected at 235.337 nm. Similar results were obtained with 247 nm photolysis, though the ”hot band” component was substantially smaller. Compared with the He results (Fig. V.1a), two main differences are observed. First, the Cl translational energy distribution becomes narrower with the largest peak at high energies corresponding to the dissociation of vibrationally “cold” CH_2Cl. Second, a band-like structure is discernible with $\sim$ 800 cm^{-1} separation between bands, close to the frequency of the C-Cl stretch in CH_2Cl (see Table V.2).

The vibrational relaxation in CH_2Cl can be enhanced by using molecular carrier gases, and therefore various mixtures of CF_4:He were also used (Fig. V.1b). Depending on the CF_4:He ratio, the results range between pure He and Ar.

However, a high vibrational temperature in the ground electronic state of the radical cannot alone explain the large fraction of ”hot band” component in the translational energy distributions at 247-312 nm. This follows directly from comparison with the results obtained with 214-240 nm photolysis (parallel type excitation), where the maximum translational energy of the products does not exceed significantly E_t^{max}, and does not depend on carrier gas. Also, at 247-312 nm the effect of the carrier gas depends on the photolysis wavelength. It was found that while at $\lambda \geq$ 280 nm most of the CH_2 and Cl signals derive from ”hot band” excitation, at 266 nm the contribution of fragments with translational energies exceeding E_t^{max} is smaller, and this fraction decreases further at 247 nm.

The above observations and analysis indicate that for the perpendicular transition, the fraction of fragments with translational energies greater than E_t^{max} is larger than expected based on a thermal vibrational population and equal excitation efficiency for excited and unexcited radicals. A large increase in the Franck-Condon factors for "hot band" excitation must also be taken into account. This implies that the ground and excited electronic state geometries must be rather different. The lowest vibrational frequency in CH_2Cl is associated with the OPLA bend ($\sim$ 390 cm^{-1}) [10, 116]. This mode should give the largest contribution to the "hot band" populations, and its substantial cooling in Ar carrier gas is expected. However, even in Ar some of the Cl fragments have energies exceeding E_t^{max}, with bands separated by $\sim$ 800 cm^{-1}, i.e., the C-Cl stretch frequency in CH_2Cl. The persistence of the C-Cl vibrational structure in the translational energy distribution, even upon cooling in Ar, suggests a large geometrical change in the C-Cl coordinate between the ground and 1^2A_1 state. Therefore, *ab initio* calculations of the PES along this coordinate were carried out as described below.

V.3 Electronic structure calculations

V.3.1 Computational details

The ground state structures and harmonic frequencies of CH_2Cl and CH_2Cl^+ (which approximates the Rydberg states) are calculated by the CCSD(T) [193] method. The equilibrium structure and vibrational frequencies of the valence state are computed

by the EOM-CCSD [124, 230] method. PESs along the C-Cl bond breaking coordinate of the ground and excited states are calculated by using the CCSD [192] and the EOM-CCSD [124, 230] methods, respectively. Geometry optimizations and vibrational analysis are performed using the 6-311(+, +)G(3df,3pd) basis set, derived from the polarized split-valence 6-311G(d,p) basis [133, 162] by augmenting it by additional sets of polarization and diffuse functions [45, 80]. For PESs, 6-311(3+, 3+)G(3df, 3pd) is employed.

The ground and excited states' PESs along the C-Cl coordinate are calculated with the C-H bond length and the H-C-H angle fixed at their ground state equilibrium values. In this study, we vary the C-Cl distance from 1.25 to 2.7 Å. Thus, the displacements from the ground state equilibrium C-Cl distance of 1.69 Å are small enough for the CCSD and EOM-CCSD results to be reliable. We have calculated total energies, transition dipole moments, and average sizes of the electron density for the X^2B_1 ground state and the two lowest $^2A_1$ excited states: the 1^2A_1 $\sigma^*_{CCl} \leftarrow \pi^*_{CCl}$ valence state and the 2^2A_1 $3s \leftarrow \pi^*_{CCl}$ Rydberg state. The calculated dipole strengths of the transitions and the PESs are then used to estimate vibrational overlaps and to calculate Franck-Condon factors.

V.3.2 Characterization of the two lowest $^2A_1$ excited states of CH_2Cl

Equilibrium structures and vibrational frequencies of the ground state, the valence 1^2A_1 excited state, and the CH_2Cl^+ cation are presented in Tables V.1 and V.2.

Table V.1: Ground and excited state geometries of CH_2Cl radical:

	Symm.	r_{CH}, Å	r_{CCl}, Å	α_{HCH}	Θ^a	Total energy, hartree
X^2B_1 [b]	C_{2v}	1.076	1.691	124.17	180	-499.007704
1^2A_1 [c]	C_{2v}	1.092	2.095	121.98	180	-498.843600
$X^1A_1CH_2Cl^+$ [b]	C_{2v}	1.088	1.590	121.91	180	-498.692604

[a] Dihedral H-C-Cl-H angle.
[b] CCSD(T)/6-311(+, +)G(3df,3pd). The cation structure approximates the structure of the Rydberg 2^2A_1 state.
[c] EOM-CCSD/6-311(+, +)G(3df,3pd)

For a perfect Rydberg state (i.e., a highly excited electron orbiting a positively charged and structureless core), the optimized geometry should be close to that of the cation, and the CH_2Cl^+ calculations were performed to determine approximately the properties of the Rydberg states. [9] .

The equilibrium structures and harmonic vibrational frequencies of the ground and 1^1A_1 valence excited state of CH_2Cl, and of CH_2Cl^+ (Table V.1) are in good agreement with the simple molecular orbital picture developed before [145]. We have found that the unpaired p-electron on carbon interacts with the chlorine lone pair, which results in an additional $\frac{1}{2}\pi$ bond between C and Cl in the CH_2Cl ground state (this yields stronger C-Cl bonding in the radical relative to the saturated compound [10]). The lowest valence 1^2A_1 excited state is derived by promotion of the unpaired electron from the π^*_{CCl} antibonding orbital to the σ^*_{CCl} antibonding orbital (see Fig. 2 in Ref. [145]). Therefore, in this state a full π bond exists, but the σ bond

[9] We also attempted to optimize the structure of the 2^2A_1 Rydberg state by using the EOM-CCSD method, however, because of the strong coupling between this state and the valence state we were unable to locate the equilibrium structure of the Rydberg state on the multidimensional PES.

Table V.2: Calculated harmonic vibrational frequencies ω_e of the ground and excited states of CH_2Cl.

State	C-Cl stretch a_1	CH_2 scissors a_1	OPLA b_1	CH_2 rock b_2	CH_2 s-stretch a_1	CH_2 a-stretch b_2
X^2B_1 [a]	868	1434	168[c]	1004	3179	3335
1^2A_1 [b]	535	1256	1253	194	3026	3206
$X^1A_1CH_2Cl^+$ [a]	1074	1492	1147	1056	3104	3249

[a] CCSD(T)/6-311(+, +)G(3df,3pd)

[b] EOM-CCSD/6-311(+, +)G(3df,3pd). The cation structure approximates the structure of the Rydberg 2^2A_1 state.

[c] Due to large anharmonicity, the harmonic OPLA frequency is about twice lower than the anharmonic 01 transition. The theoretical value of ω_{01} is 434 cm^{-1} [146].

order decreases, and a planar structure with an elongated C-Cl bond relative to the ground state is preferred. Likewise, in 1^2A_1 the C-Cl vibrational frequency is lower, while the OPLA vibrational frequency is considerably higher than in the ground state (due to the decrease in σ bond order and the increase in π bond order, respectively). The results presented in Tables V.1 and V.2 are consistent with this picture. Similar considerations explain the properties of the cation, which is derived by removing an electron from the π^*_{CCl} antibonding orbital. The full double C-Cl bond in the cation explains the C-Cl bond contraction relative to the ground state and the OPLA frequency increase up to 1147 cm^{-1}. This value approaches the OPLA frequency of the valence excited state (1253 cm^{-1}). For reference, the OPLA vibrational frequency of formaldehyde (CH_2O), a molecule with a full π_{CO} bond, is 1167 cm^{-1} [2].

As seen in Table V.1, the difference between the C-H equilibrium bond lengths in the ground and the lowest excited state of the CH_2Cl radical is only 0.016 Å. The change in the H-C-H angle is also small (2.19^o). This suggests that the minimum energy path for the C-Cl bond breaking reaction on the 1^2A_1 PES is close to the pure C-Cl stretch (for C-Cl separations $\sim$ 1.25-2.10 Å), and that the other degrees of freedom can be frozen. Thus, we have calculated one-dimensional cuts of the PESs along the C-Cl stretch, with the values of the other two internal coordinates being fixed at the ground state equilibrium values. The resulting adiabatic potential energy curves are shown in Fig. V.2.

The barrier on the 2^2A_1 state curve is due to an avoided crossing of the Rydberg 3s state with the 9^2A_1 valence state (which has been identified as a $\pi^*_{CCl} \leftarrow \sigma_{CCl}$

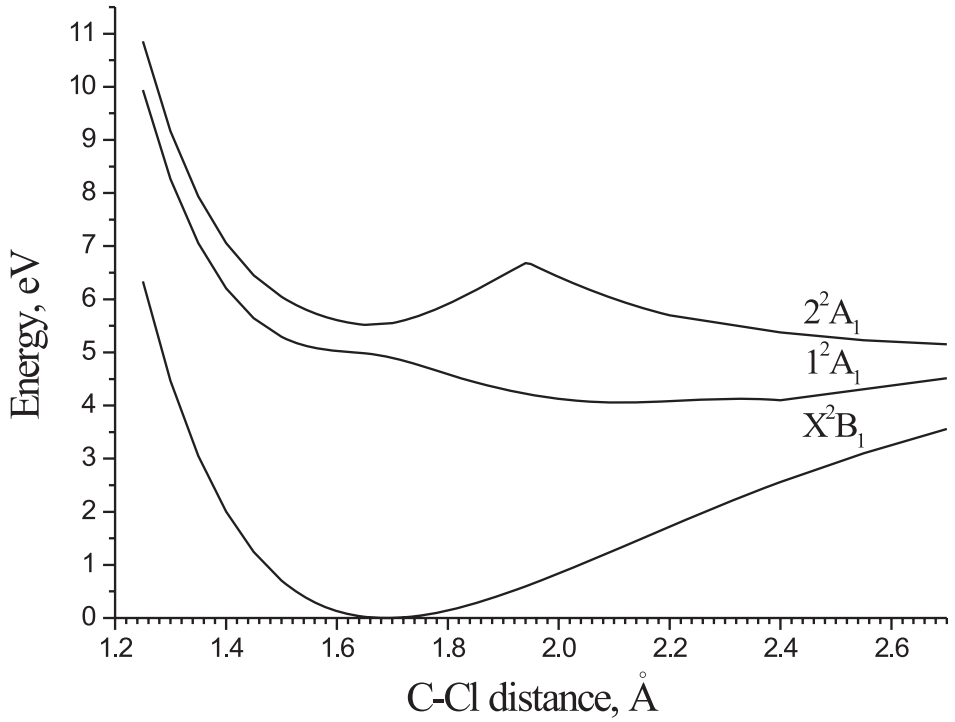

Figure V.2: Potential energy curves for the ground X^2B_1 and the two lowest $^2A_1$ excited states along the C-Cl coordinate (all other degrees of freedom are held at their ground state equilibrium values). All curves are shifted such that the ground state energy at equilibrium is zero.

transition, and therefore is expected to be purely repulsive [145]). This is confirmed by the sharp drop in the size of the electron density for large C-Cl separations. Such behavior of Rydberg states in bond breaking reactions is general and was described by Gordon and coworkers (see Ref. [91] and references therein).

An interesting feature of the 1^2A_1 curve shown in Fig. V.2 is its shelf-like shape in the vicinity of the ground state equilibrium geometry (i.e., in the active Franck-Condon region). Similar shapes of the excited state potentials were observed in alkali atom dimers [11, 166, 167, 249], where a double minimum is formed as a result of Rydberg-valence interaction [11, 130, 249]. In Sec. V.3.3 we demonstrate that the

shelf on the 1^2A_1 PES indeed is a result of coupling between the valence and the 3s Rydberg states.

The calculated dependence of the electronic transition dipole strength on the C-Cl separation for the $1^2A_1 \leftarrow X^2B_1$ and $2^2A_1 \leftarrow X^2B_1$ transitions is shown in Fig. V.3.

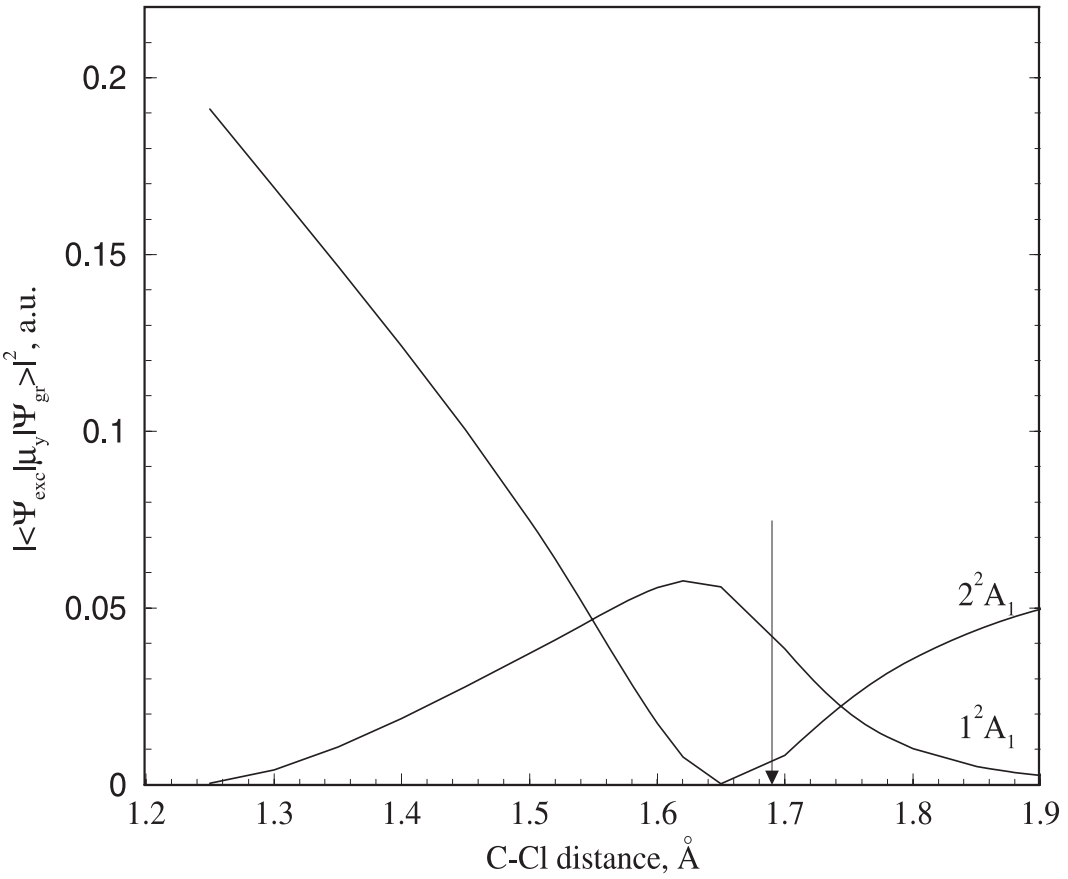

Figure V.3: Dipole strength dependence on the C-Cl distance for the $1^2A_1 \leftarrow X^2B_1$ and $2^2A_1 \leftarrow X^2B_1$ transitions. The vertical arrow indicates the ground state equilibrium C-Cl distance.

Due to the Rydberg-valence interaction in the 1^2A_1 and 2^2A_1 states mentioned above, the dipole strength of the transition to the 1^2A_1 state increases at shorter C-Cl distances ($\sim$1.6 Å) (see Sec. V.3.3). As shown in Sec. V.4, this behavior of the

transition dipole moment contributes to the enhancement of the absorption probability for vibrationally excited CH_2Cl. The sharp rise in the $2^2A_1 \leftarrow X^2B_1$ transition dipole strength at $r_{CCl} < 1.6$ Å results from the increased $3p_z$ character at short C-Cl distances (see Sec. V.3.3).

V.3.3 Rydberg-valence interactions in the lowest excited states of CH_2Cl

This subsection presents our analysis of the changes in the character of the wave functions for the two lowest adiabatic states along the C-Cl stretching coordinate. Avoided crossings due to Rydberg-valence interactions in closed-shell species were extensively characterized by Gordon and Caldwell [91], and Salem [202]. Gordon's study [90, 91] of saturated molecules (e.g., alkanes) demonstrates that their low lying vertical excited states are Rydberg states. Since photodissociation of alkanes excited to these Rydberg states yields ground state products, an avoided crossing between an initially excited Rydberg state and a dissociative valence state must take place [91].

Salem [202] characterized avoided crossings due to Rydberg-valence interaction as avoided crossing between the relevant molecular orbitals (i.e., one-electron states). For open-shell species (like CH_2Cl), in which there are low lying valence *and* Rydberg excited states derived from the promotion of the unpaired electron, this type of avoided crossing is expected to be quite common.

Obviously, the distinction between Rydberg and valence states is merely qualitative. From a quantum chemical perspective, an excited state is a Rydberg state if its

configurational expansion is dominated by configurations in which the excited electron occupies diffuse (Rydberg) orbitals. We have used this and several other criteria when assigning Rydberg or valence character to the excited states of CH_2Cl [145]. In this study, the size and spatial asymmetry of electron density are used. [10] Near the ground state equilibrium geometry, the 1^2A_1 and 2^2A_1 states can be assigned valence and 3s Rydberg character, respectively [145]. Changes in the size and asymmetry of the electron density along the C-Cl stretch reflect changes in the excited states' characters.

Figure V.4a presents the spherical average $\langle r^2 \rangle = \frac{1}{3}(\langle x^2 \rangle + \langle y^2 \rangle + \langle z^2 \rangle)$ of the electron charge distribution for the ground and the two lowest excited states as a function of the carbon-chlorine separation.

The monotonous increase of $\langle r^2 \rangle$ for the ground state as the C-Cl distance increases reflects the increase in molecular size due to the C-Cl bond elongation. Therefore, it is convenient to eliminate this dependence by subtracting the ground state $\langle r^2 \rangle$ from the $\langle r^2 \rangle$ of the excited states. As can be seen in Fig. V.4b, the relative size of the electron charge distribution $\Delta\langle r^2 \rangle$ of the 1^2A_1 state is small at large C-Cl distances (r_{CCl} $\sim$1.8 Å), then increases at smaller r_{CCl}, and remains approximately constant at r_{CCl} <1.56 Å. $\Delta\langle r^2 \rangle$ of the 2^2A_1 state is larger than that of the 1^2A_1 state at large r_{CCl}, then the difference between their relative sizes decreases as the C-Cl

[10] The size of electron density can be estimated as an expectation value of the one-electron operator $\frac{1}{3}(\hat{x}^2 + \hat{y}^2 + \hat{z}^2)$. By considering $\langle \hat{x}^2 \rangle$, $\langle \hat{y}^2 \rangle$, and $\langle \hat{z}^2 \rangle$ separately one can characterize the deviation of the electron distribution from a spherical shape. For s-type Rydberg states this deviation is expected to be small, while p-type Rydberg states will exhibit larger charge anisotropy.

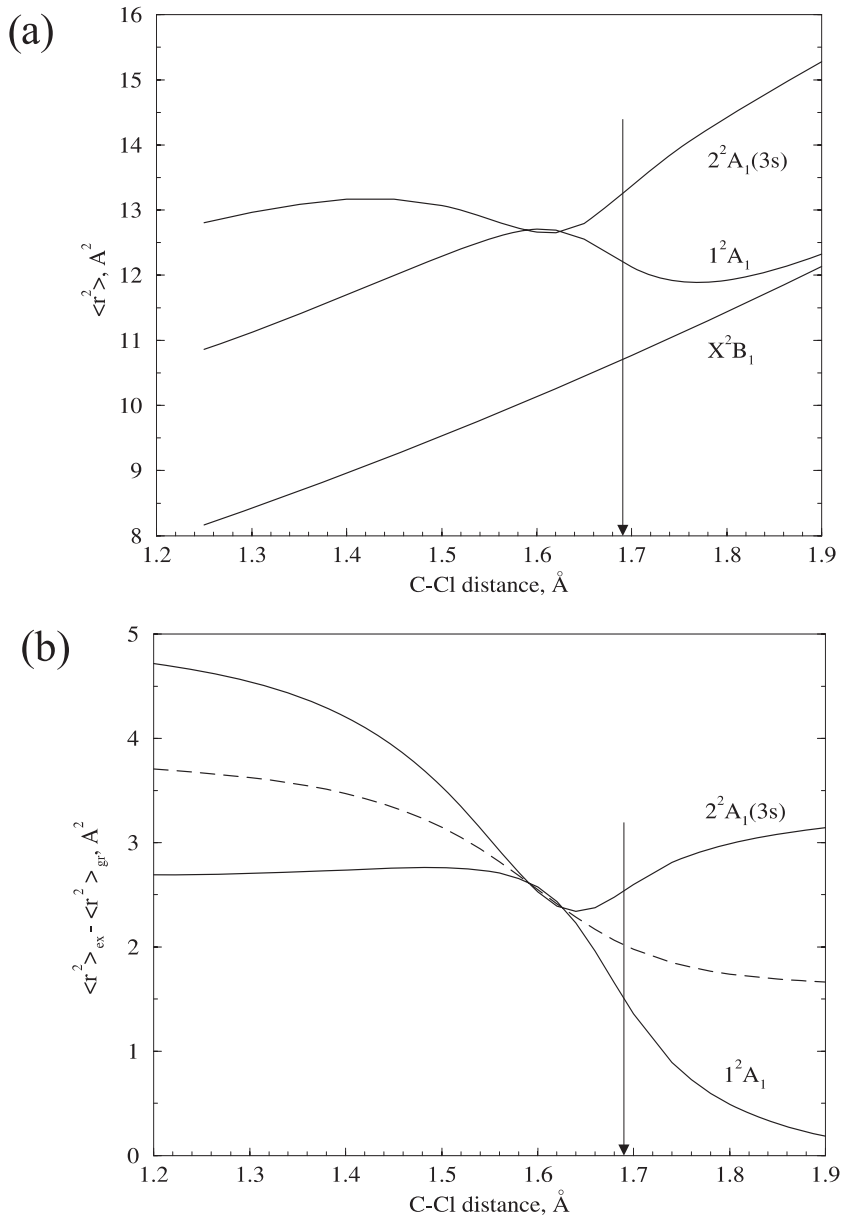

Figure V.4: Spherical average of the electron density, $\langle r^2 \rangle$, as a function of the C-Cl distance for the ground and the two lowest $^2A_1$ excited states of the CH_2Cl radical (upper panel). The lower panel shows changes in the excited state density relative to the ground state, i.e., $\Delta\langle r^2 \rangle = \langle r^2 \rangle_{ex} - \langle r^2 \rangle_{gr}$ (this subtracts changes due to molecular size increase at larger molecular separations). The dashed line corresponds to the average value for both states. The vertical arrow indicates the ground state equilibrium C-Cl distance.

bond contracts, and it vanishes at r_{CCl}=1.62 Å. This variation reflects the interaction between the two states. At shorter C-Cl distances, $\Delta\langle r^2\rangle$ of the 2^2A_1 state continues to increase until it approaches a higher constant value at r_{CCl} <1.2 Å.

This behavior confirms that the 1^2A_1 and 2^2A_1 states indeed interact with each other. However, the sum of $\Delta\langle r^2\rangle$ for these two states, which exchange their character, is not constant (the dashed line in Fig. V.4b represents the average). This implies that other states are mixed in. The increase in $\Delta\langle r^2\rangle$ of the 2^2A_1 state at r_{CCl} <1.62 Å signifies a higher Rydberg character. We identify this character as $3p_z$, based on the following observations. First, the next vertically excited state of A_1 symmetry above 2^2A_1 is the Rydberg $3p_z$ state [145]. Second, the dipole strength of the transition to this state is the largest among the other calculated A_1 states, which explains the sharp rise of the dipole strength of the transition to the 2^2A_1 state at small r_{CCl} (Fig. V.3). Third, the calculated relative sizes of the electron density along the X, Y, and Z axes (presented in Fig. V.5) demonstrate that the anisotropy of the 2^2A_1 density increases and becomes much larger than that of the 1^2A_1 state due to elongation of the electron density along the molecular axis (Z) as the C-Cl bond contracts.

This indicates that the 2^2A_1 state acquires Rydberg $3p_z$ character at short C-Cl distances.

The above analysis explains the interactions in the low lying excited states of CH_2Cl, which are reflected in Fig. V.4. At large C-Cl separations ($\sim$ 1.8 Å) the lowest excited state is the valence state derived from the $\sigma^* \leftarrow \pi^*$ excitation, while the second excited state has a predominant 3s character. At the ground state geometry

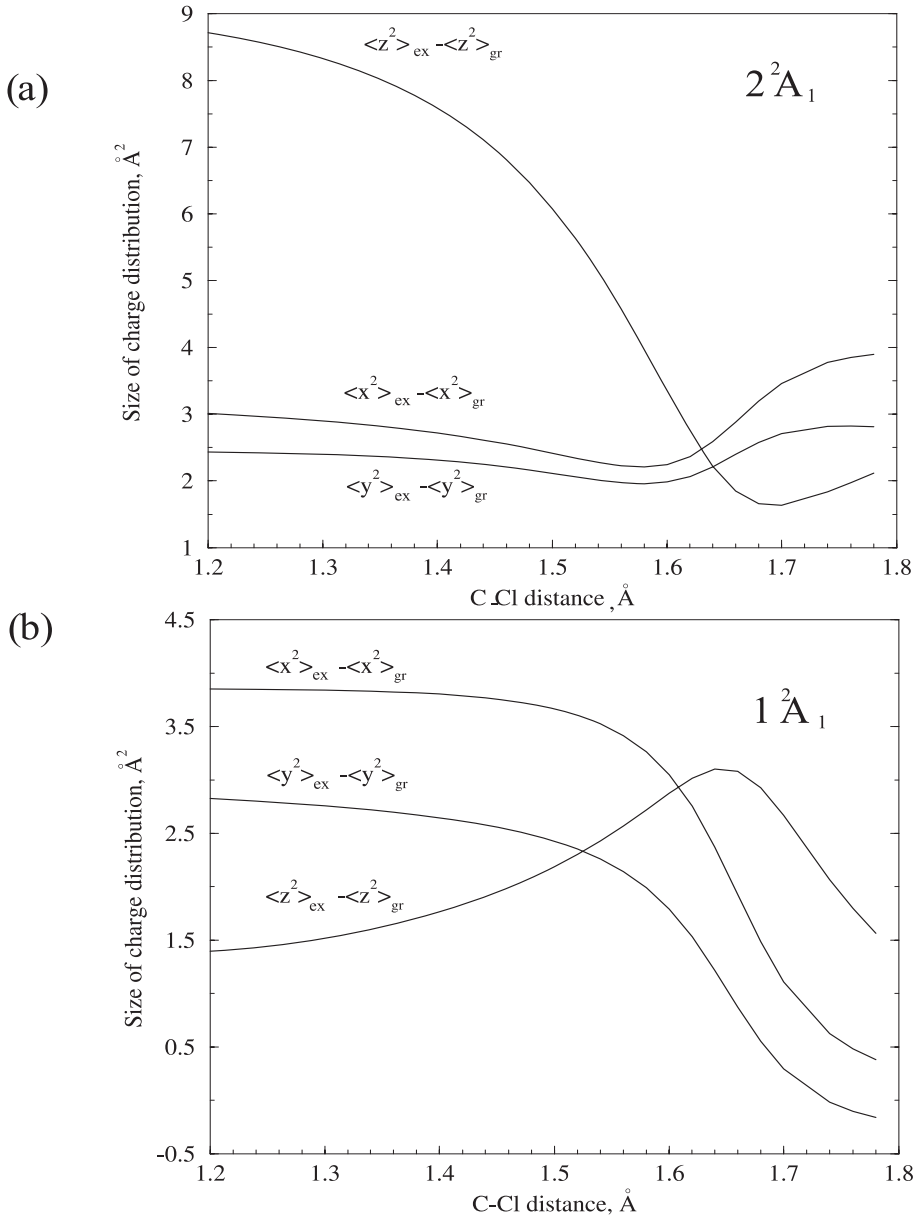

Figure V.5: $\langle x^2 \rangle$, $\langle y^2 \rangle$, and $\langle z^2 \rangle$ components of the total electron charge distribution for 2^2A_1 (upper panel) and 1^2A_1 (lower panel) as a function of the C-Cl bond length. The molecular plane is the XZ-plane, the C-Cl bond defines the Z-axis.

(~ 1.69 Å) the two states are already mixed, but still retain their identities. At shorter C-Cl bond lengths (< 1.6 Å), the lower state becomes the 3s Rydberg state, while the upper state acquires a mixed valence and Rydberg 3p$_z$ character. The interaction

with the $3p_z$ state leads to the double crossing of the curves in Fig. V.4, and to the larger size of electron density for 2^2A_1 at small r_{CCl}.

V.4 Enhancement of hot bands' intensities

Based on the results of the *ab initio* calculations we can give now (at least qualitatively) an explanation for the "hot bands" enhancement in the absorption probability for the perpendicular $1^2A_1 \leftarrow X^2B_1$ transition. The probability of a transition between two states, which are characterized by the total wave functions $\Psi^0(\vec{r}_e, \vec{r}_N)$ and $\Psi^1(\vec{r}_e, \vec{r}_N)$ is proportional to the square of the transition dipole moment:

$$P \sim \left[\int \Psi^0(\vec{r}_e, \vec{r}_N) \vec{\mu}(\vec{r}_e) \Psi^1(\vec{r}_e, \vec{r}_N) dr \right]^2 \tag{V.4}$$

where $\vec{\mu}$ is the dipole moment operator, and $\vec{r}_e$ and $\vec{r}_N$ represent electronic and nuclear coordinates, respectively. In the Born-Oppenheimer approximation, $\Psi^0(\vec{r}_e, \vec{r}_N)$ and $\Psi^1(\vec{r}_e, \vec{r}_N)$ are separable into electronic and nuclear parts:

$$\Psi^i \approx \psi_e^i(\vec{r}_e; \vec{r}_N) \phi_{vib}^i(\vec{r}_N), \qquad i = 0,\ 1 \tag{V.5}$$

where $\phi_{vib}^0(\vec{r}_N)$ and $\phi_{vib}^1(\vec{r}_N)$ are vibrational functions for the initial and final electronic states, respectively, and the dependence of $\psi_e^i(\vec{r}_e; \vec{r}_N)$ on nuclear coordinates

is parametric rather than explicit. Since $\phi^0_{vib}(\vec{r}_N)$ and $\phi^1_{vib}(\vec{r}_N)$ do not depend on electronic coordinates, Eq.(V.4) can be rewritten as:

$$P \sim \left[\int \phi^0_{vib}(\vec{r}_N) \vec{\mu}_e(\vec{r}_N) \phi^1_{vib}(\vec{r}_N) d\vec{r}_N \right]^2 \tag{V.6}$$

where $\vec{\mu}_e(\vec{r}_N)$ is the electronic transition dipole moment, which is given by integration over the electronic coordinates $\vec{r}_e$:

$$\vec{\mu}_e(\vec{r}_N) = \int \psi^0_e(\vec{r}_e; \vec{r}_N) \vec{\mu}(\vec{r}_e) \psi^1_e(\vec{r}_e; \vec{r}_N) d\vec{r}_e \tag{V.7}$$

As follows from Eq.(V.6), two factors contribute to the transition probability: the spatial overlap of the initial and final vibrational functions and the value of the electronic transition dipole moment in the region of maximum spatial overlap. For convenience, we discuss the dependence of the integral in Eq.(V.6) on vibrational excitation in terms of vibrational Franck-Condon factors and electronic transition dipole moments, although in our simulations we do not assume constant $\mu_e(R)$.

Although Eq.(V.6) should be integrated over all nuclear coordinates, because the transition to the 1^2A_1 state mainly affects the C-Cl bond length we limit our qualitative treatment to a one-dimensional potential energy curve:

$$P \sim \left[\int_0^\infty \phi^0_{vib}(R) \vec{\mu}_e(R) \phi^1_{vib}(R) dR \right]^2 \tag{V.8}$$

where $\vec{\mu}_e(R)$ is the electronic transition dipole moment as a function of the C-Cl distance R. The lower state vibrational functions can be calculated either in the harmonic or (more accurately) in the Morse potential approximation. Since excitation occurs close to the dissociation threshold of the upper state, the corresponding wave function can be calculated in the linear approximation by using Airy functions [141]. The important feature of this wave function is that it is concentrated around the "classical" turning point and oscillates beyond this region, as shown schematically in Fig. V.6.

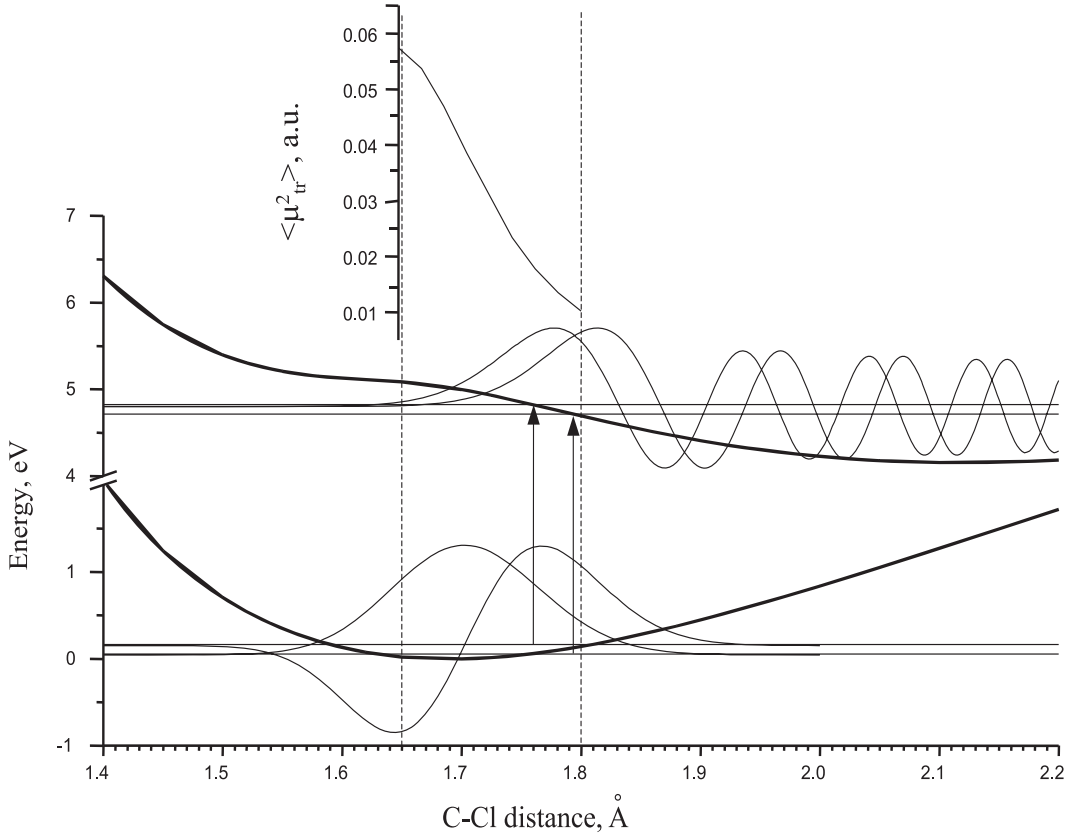

Figure V.6: Illustration of the hot bands' enhancement mechanism. Horizontal lines at the bottom of the potential energy curve for the ground state represent vibrational levels of the C-Cl stretch. Vertical arrows show electronic excitation upon absorption of a 266 nm photon. Transition dipole strength is shown in the inset.

As a consequence, the vertical electronic transition is centered mostly near this turning point.

We were able to simulate qualitatively the enhanced probability for "hot band" excitation by calculating the Franck-Condon integrals for the ground and 1^2A_1 states for Morse and Airy wave functions, respectively. This was done for the same range of photon energies as used in the experiments. By shifting the excited-state curve within the error bars of the calculations ($\pm$ 0.1 eV; $\pm$ 0.1 Å), we could find conditions that gave enhancements that are comparable to the observed ones.

The simulations and the discussion above can now be combined to give a physical interpretation to the observed enhancement. The picture that emerges is illustrated in Fig. V.6. The horizontal lines at the bottom of the ground state potential energy curve represent the ground and first excited vibrational levels of the C-Cl stretch. The vertical lines illustrate 266 nm absorption that promotes the radical to the excited 1^2A_1 state. In the upper panel, the dipole strength of this transition is shown in the active Franck-Condon region (between the vertical dashed lines). As seen in Fig. V.6, the spatial overlap of the vibrational functions in the ground and 1^2A_1 states is small as a result of their very different equilibrium geometries.

At the low-energy edge of the perpendicular absorption band, the turning points on the 1^2A_1 state are reached only at long C-Cl distances in the ground electronic state, where the probability density of the ground vibrational level is very small. Moreover, at these long C-Cl distances, the electronic transition strength is also small. This makes P small for excitation from the ground vibrational state.

Upon vibrational excitation in the ground electronic state, the probability density of the higher vibrational level is larger at long R than for the ground vibrational state. At long wavelengths, two effects conspire to enhance the absorption probability from excited vibrational states. First, the probability densities of the higher vibrational levels at long C-Cl distances are larger than for the ground vibrational state. This increases the vibrational Franck-Condon factor. Second, photon absorption originating in an excited vibrational level reaches the turning point on the upper electronic curve at shorter C-Cl distances. This increases not only the vibrational Franck-Condon overlap, but also the electronic dipole strength (see Fig. V.6). The result is a significant increase in absorption probability for the "hot bands".

The enhancement effect is expected to be largest at the longest wavelengths. At shorter wavelengths the upper curve can be reached from the ground vibrational state at the equilibrium C-Cl distance, and therefore the contribution of the ground vibrational level will start to dominate. This agrees with the experimental observations.

V.5 Conclusions

Based on EOM-CCSD calculations of potential energy curves and properties of excited states, we have explained the enhancement in the electronic absorption probability for vibrationally excited CH_2Cl observed experimentally. For this purpose, we have calculated equilibrium structures, vibrational frequencies, and PESs for the ground, X^2B_1, and the two lowest excited states, 1^2A_1 and 2^2A_1, of CH_2Cl. We have

found that the changes in geometries and frequencies upon excitation are in good agreement with the molecular orbital picture developed in our previous work [145]. In order to estimate Franck-Condon factors, we have also calculated transition dipole moments for the $1^2A_1 \leftarrow \mathrm{X}^2B_1$ and $2^2A_1 \leftarrow \mathrm{X}^2B_1$ transitions.

Analysis of the size and asymmetry of the electron density at different C-Cl separations reveals that the valence 1^2A_1 and the Rydberg 2^2A_1 states exchange their character, which results in an avoided crossing at about 1.62 Å. This changes the shape of the 1^2A_1 potential curve considerably. Moreover, a third Rydberg state is mixed in with the 2^2A_1 state at shorter distances causing a significant increase in transition dipole strength. These changes result in a large increase in Franck-Condon factors for absorption from vibrationally excited CH_2Cl. Our results demonstrate that the Rydberg-valence interactions, which have a pronounced effect on the photodynamics, involve more than two excited states of CH_2Cl, even within a small range of geometry variations. This confirms the importance and prevalence of Rydberg-valence interactions in open-shell systems.

Chapter VI. EOM-SF-CCSD versus EOM-EE-CCSD: electronic states of cyclobutadiene

In order to demonstrate capabilities and advantages of the EOM-SF-CCSD model, we have applied it to calculate vertical and adiabatic electronic excitation energies in cyclobutadiene. As explained below, the degree of orbital degeneracy and, consequently, the character of the low-lying valence states of cyclobutadiene depend strongly on nuclear positions — while at the lowest triplet state equilibrium geometry the lowest singlet state is two-configurational, it becomes predominantly single-configurational at its own equilibrium geometry. We will demonstrate that although advanced single reference techniques (e.g., EOM-EE-CCSD) give reasonable description of the cyclobutadiene excited states in the latter case, they fail in the former. EOM-SF-CCSD, however, treats both limits well, and therefore yields accurate results for both vertical and adiabatic energies.

Most of the calculations are performed in the cc-pVTZ basis set [65]. The performance of the less expensive basis set composed of the cc-pVTZ basis on carbon atoms and cc-pVDZ on hydrogens is also investigated. Equilibrium geometries of the

X^1A_g ground state and the 1^3A_{2g} excited state are optimized by the CCSD(T) [193] and SF-DFT [216] methods. [11] Vertical and adiabatic excitation energies are calculated at these geometries. All electrons are active in the CCSD(T) and the EOM-CCSD calculations. Both UHF and ROHF references are used in the EOM-SF-CCSD calculations.

VI.1 Molecular orbitals and characterization of low-lying valence states of cyclobutadiene

Fig. VI.1 shows the π-system of cyclobutadiene — molecular orbitals derived from the four atomic p_z-orbitals of carbons (Z-axis is perpendicular to the molecular plane).

At the square (D_{4h}) geometry (Fig. VI.1, left panel), two of the four π-orbitals are exactly degenerate. This degeneracy is lifted by a rectangular distortion (Fig. VI.1, right panel). The leading electronic configurations of the lowest valence states are shown in Fig. VI.2.

At both D_{4h} and D_{2h} structures, the lowest four states are derived by distributing two electrons in two (nearly)-degenerate molecular orbitals. Therefore, these states are best described as diradical states [24, 25, 203, 221, 223]. Note that at the D_{4h} geometry, all the electronic states are exactly two-configurational, while at the

[11] We used the functional composed of the equal mixture of the following exchange and correlation parts: 50% Hartree-Fock + 8 % Slater + 42 % Becke for exchange, and 19% VWN + 81% LYP for correlation.

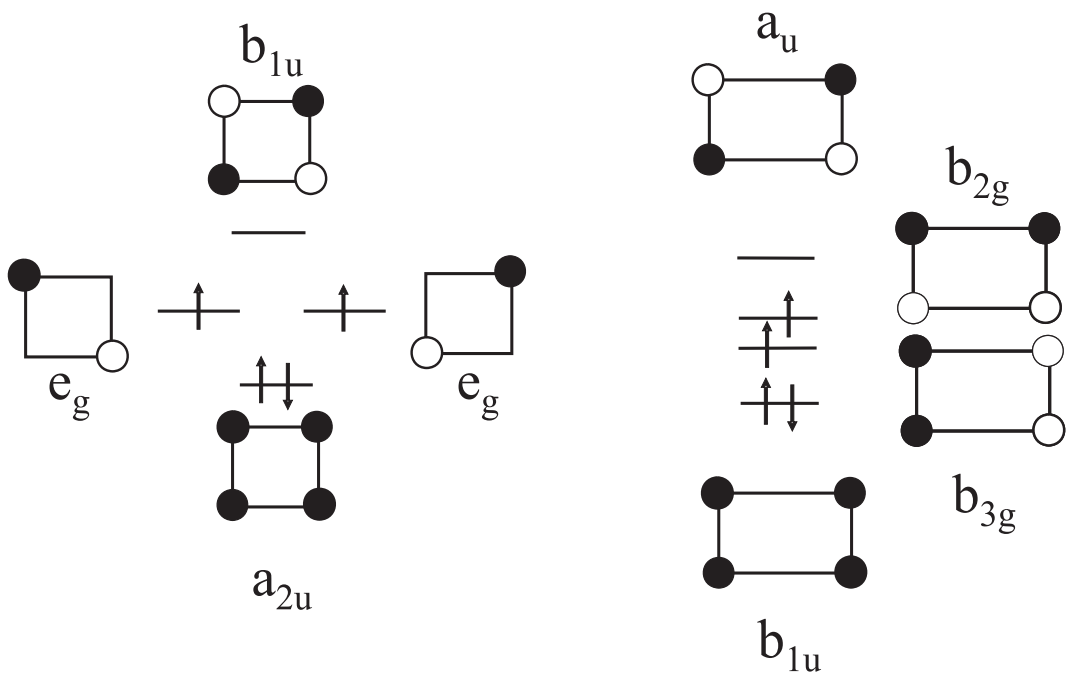

Figure VI.1: Molecular π-orbitals derived from carbons' p-orbitals at the 1^3A_{2g} equilibrium geometry (left panel), and at the X^1A_g equilibrium geometry (right panel). Electronic configuration of the triplet state is shown.

D_{2h} structure the wave-function of the ground X^1A_g state is dominated by a single determinant. As it follows from the molecular orbital picture, D_{2h} distortions are energetically favorable for the ground X^1A_g state [126].

The experimental structure of cyclobutadiene is not available, however, there is a host of theoretical calculations [3, 5, 6, 15, 27, 32, 35, 60, 61, 79, 89, 93, 100–102, 117, 126, 127, 173, 180, 195, 205–207, 215]. Table VI.1 summarizes some of the previously reported structures of the X^1A_g state calculated by single-reference (SR) and multi-reference (MR) SCF, CC, and DFT methods.

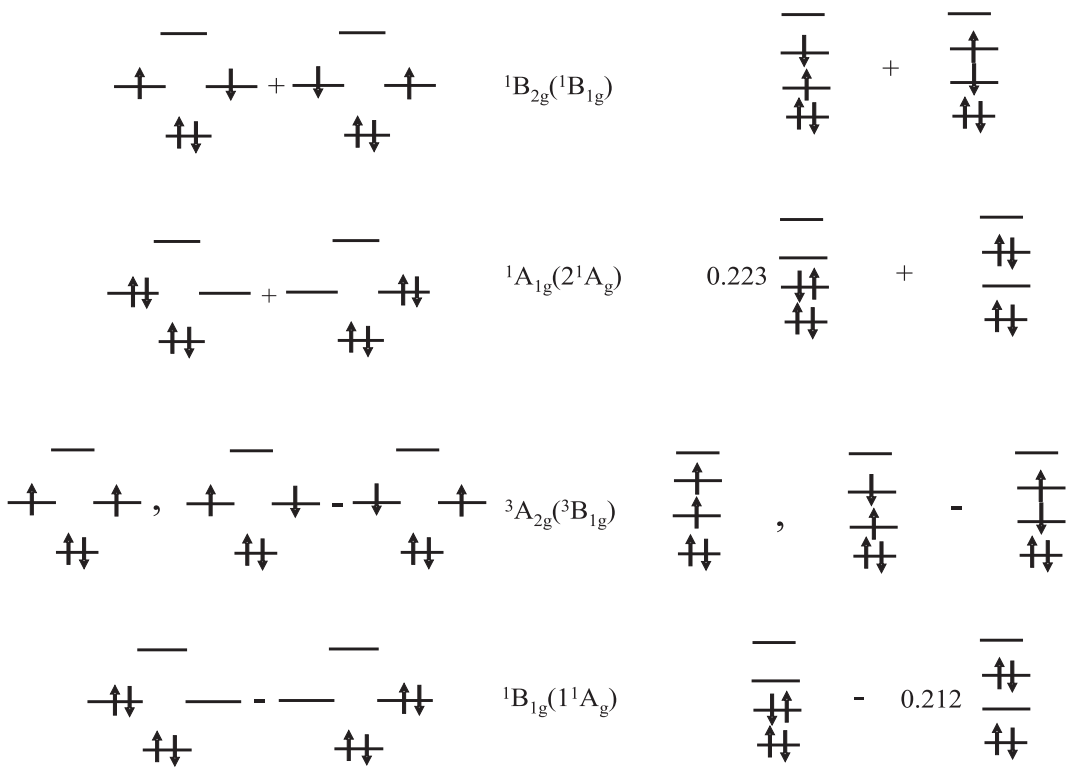

Figure VI.2: Leading electronic configurations in the EOM-SF-CCSD wave functions of the valence states of cyclobutadiene at the square (left panel) and rectangular (right panel) geometries. For the D_{4h} geometries (left panel), D_{2h} symmetry labels are given in parentheses.

Fig. VI.3 presents the equilibrium geometries of the $^3A_{2g}$ and X^1A_g states optimized at the CCSD(T)/cc-pVTZ level. For the well-behaved triplet state, the errors in the CCSD(T)/cc-pVTZ geometry should not exceed 0.002 Å [97].

However, the accuracy of the CCSD(T) model for the X^1A_g state may deteriorate due to the anticipated multi-configurational character of this state. To clarify this, we performed geometry optimization with the SF-DFT method which was shown to yield very accurate structures for diradicals and triradicals [216, 222, 223]. An excellent agreement between the SF-DFT and CCSD(T) geometries suggests relatively

Table VI.1: Optimized geometries of the rectangular ground X^1A_g state of cyclobutadiene. The bondlength alternation, Δ_{CC}, is also shown. Bondlengths are in angstrom, angles — in degrees.

	C-C	C=C	Δ_{CC}	CH	HCC[a]
SCF/cc-pVDZ[b]	1.569	1.323	0.25	1.079	134.9
B3LYP/cc-pVDZ[c]	1.581	1.339	0.24	1.090	134.9
CCSD/[3s2p1d/2s][d]	1.609	1.383	0.23	1.092	134.6
CCSD(T)/cc-pVDZ[b]	1.583	1.364	0.22	1.095	134.9
MCSCF/6-31G[e]	1.553	1.366	0.22	1.068	134.8
MPJ5(GVB)/cc-pVDZ[c]	1.580	1.336	0.24	1.068	134.9
MR-CCSD/[3s2p1d/1s][f]	1.570	1.367	0.20	1.103	134.7
SF-DFT/6-311G**[g]	1.56	1.33	0.23	1.07	134.9
CCSD(T)/cc-pVTZ[g]	1.566	1.343	0.22	1.074	134.9

[a] the angle between the CH bond and the longer CC bond.
[b] Ref. [205, 206].
[c] Ref. [205].
[d] this work, basis from Ref. [35].
[e] CAS within the π system, Ref. [180].
[f] Ref. [15].
[g] this work, see also Fig. VI.3.

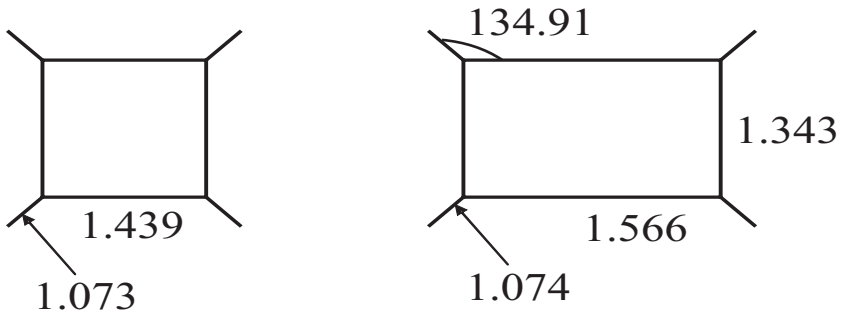

Figure VI.3: Equilibrium geometries of the 1^3A_{2g} (left) and X^1A_g (right) references, optimized at the CCSD(T)/cc-pVTZ level of theory. Bond lengths are in angstroms, angles — in degrees.

minor multi-configurational character in the X^1A_g state. This is also confirmed by the EOM-SF-CCSD amplitudes (see Fig. VI.2).

As it follows from Table VI.1, the ground state structure is rather sensitive to the theoretical method employed. First, including dynamical correlation effects

results in longer CC and CH bonds — compare, for example, the SCF/cc-pVDZ and CCSD(T)/cc-pVDZ results. Secondly, a basis set of a better than cc-pVDZ quality is required for accurate geometries — comparison between the CCSD(T)/cc-pVDZ and CCSD(T)/cc-pVTZ results shows that the increase in the basis set size results in considerably shorter bond lengths. Finally, non-dynamical correlation leads to more square structures, e.g., compare the bond alternation for the SCF and MCSCF methods, or for CCSD and MR-CCSD. Overall, we conclude that the CCSD(T)/cc-pVTZ geometries present the best estimates of the equilibrium structures, and we employ these geometries in our calculations of vertical and adiabatic excitation energies. Of course, the lowest singlet at square geometries is multi-configurational, and would not be correctly described by the traditional single-reference methods.

VI.2 Vertical and adiabatic excitation energies of cyclobutadiene

Calculated vertical excitation energies at the singlet and triplet geometries are presented in Tables VI.2 and VI.3, respectively.

The EOM-SF-CCSD results are also shown in Fig. VI.4.

One of the many non-trivial features of cyclobutadiene is the violation of Hund's rule — the singlet state is below the triplet even at the triplet equilibrium geometry, when HOMO and LUMO are exactly degenerate [25, 32]. Although Hund's rule always works for atoms, it can be violated in molecules through the effect of dynamic spin-polarization [25].

Table VI.2: Total energies (hartree) of the ground X^1A_g state of cyclobutadiene, and vertical excitation energies (eV) at the X^1A_g equilibrium geometry[a].

	$E_{tot}(X^1A_g)$[b]	1^3B_{1g}	2^1A_g	1^1B_{1g}
EOM-CCSD[c]	-154.39346	1.353	n/a	3.326
EOM-CCSD[d]	-154.41693	1.351	n/a	3.319
UHF-EOM-SF-CCSD[c]	-154.40152	1.661	4.376	3.426
UHF-EOM-SF-CCSD[d]	-154.42495	1.659	4.369	3.420
ROHF-EOM-CCSD[d]	-154.44254	1.661	4.363	3.417

[a] D_{2h} symmetry, optimized at the CCSD(T)/cc-pVTZ level of theory.
[b] For EOM-CCSD, the total CCSD energy of the X^1A_g reference; for EOM-SF-CCSD, the total energy of the EOM 1^1A_g target state. The 1^3B_{1g} reference is employed in the SF calculations.
[c] Mixed basis: cc-pVTZ on carbons and cc-pVDZ on hydrogens.
[d] Full cc-pVTZ basis.

Table VI.3: Total energies (hartree) of the ground X^1B_{1g} state of cyclobutadiene, and vertical excitation energies (eV) at the 1^3A_{2g} equilibrium geometry[a].

	$E_{tot}(X^1B_{1g})$[b]	1^3A_{2g}	2^1A_{1g}	1^1B_{2g}
EOM-CCSD/cc-pVTZ[c]	-154.35712	-0.592	n/a	1.539
EOM-CCSD/cc-pVTZ[d]	-154.38058	-0.590	n/a	1.534
UHF-EOM-SF-CCSD/cc-pVTZ[c]	-154.38952	0.369	1.826	2.145
UHF-EOM-SF-CCSD/cc-pVTZ[d]	-154.41301	0.369	1.824	2.143
ROHF-EOM-SF-CCSD/cc-pVTZ[d]	-154.41342	0.369	1.814	2.137

[a] D_{4h} symmetry, optimized at the CCSD(T)/cc-pVTZ level of theory.
[b] For EOM-CCSD, the total CCSD energy of the X^1B_{1g} reference; for EOM-SF-CCSD, the total energy of the EOM X^1B_{1g} target state. The 1^3A_{2g} reference is employed in the SF calculations.
[c] Mixed basis: cc-pVTZ on carbons and cc-pVDZ on hydrogens.
[d] Full cc-pVTZ basis.

Since the HOMO-LUMO degeneracy is lifted by the rectangular distortion from the square geometry (Fig. VI.2, right panel), the EOM-CCSD provides qualitatively correct description of the excited states, i.e., singlet-triplet ordering at the singlet geometry. Quantitatively, however, the difference between the EOM-EE-CCSD and

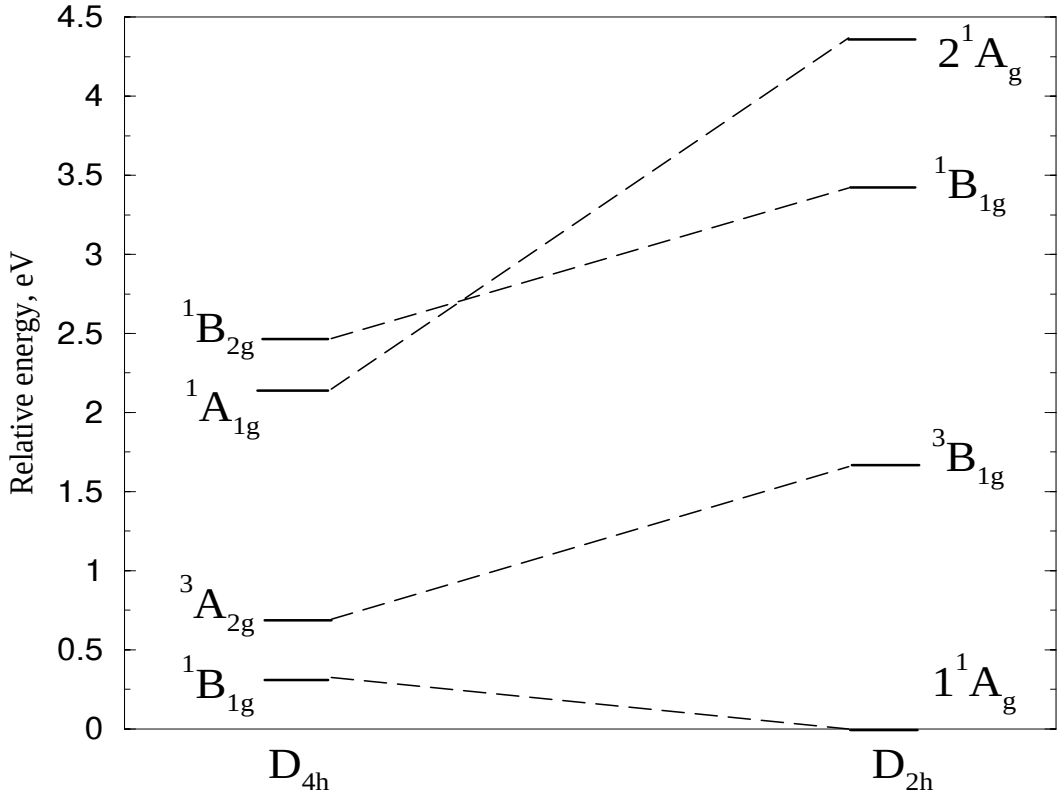

Figure VI.4: Excitation energies of the valence states of cyclobutadiene relative to the ground X^1A_g state at the CCSD(T)/cc-pVTZ optimized geometry.

the EOM-SF-CCSD excitation energies equals 0.308 eV, which is beyond the EOM-CCSD error bars of 0.1-0.3 eV [142]. Therefore, even at the distorted geometry the ground state is sufficiently multi-configurational for the EOM-CCSD to fail (see Fig. VI.2, right panel). The EOM-CCSD errors for the second closed-shell singlet are much larger due to substantial doubly excited character.

At the square geometry, where HOMO and LUMO are exactly degenerate, the EOM-CCSD model fails more dramatically, e.g., singlet-triplet ordering is reversed due to the unbalanced treatment of the two leading determinants (see Fig.VI.2, left

panel). The EOM-SF-CCSD model, however, gives the correct singlet-triplet ordering because both degenerate configurations are formally single excitations (with a spin-flip) from the high-spin triplet reference, and therefore are treated on an equal footing by the SF methods.

Finally, the EOM-EE-CCSD and EOM-SF-CCSD adiabatic excitation energies for the $^3A_{2g} \leftarrow X^1A_g$ transition are 0.399 and 0.694 eV, respectively.

We found that the EOM-SF-CCSD excitation and total energies are rather insensitive to the reference employed, for example, the difference between the UHF and ROHF excitation energies does not exceed 0.01 eV. This is consistent with the recent study of Sears *et al.* [210]. On a more technical side, Tables VI.2 and VI.3 demonstrate that the excitation energies calculated with the full cc-pVTZ basis and a smaller basis composed of the cc-pVTZ basis on carbons and the cc-pVDZ basis on hydrogen are very close.

The experimental data on the electronic spectrum of C_4H_4 are scarce and contradictory [12, 16, 151, 157, 158]. The most recent measurement of the UV absorption spectrum of argon-matrix isolated cyclobutadiene was reported by Michl's group [12]. It shows only one intense peak around 200 nm (6.2 eV), however, a weak absorption tail extends up to about 500 nm (2.5 eV). Note that the only spin- and symmetry-allowed transition from Table VI.2 is $^1B_{1g} \leftarrow X^1A_g$ at 3.42 eV.

The electronic spectrum of cyclobutadiene has been serving as a sharpening stone for electronic structure methodology [3, 5, 6, 15, 26, 27, 32, 48, 60, 74, 79, 93, 117, 156, 180, 228, 251]. For a comprehensive review of earlier results, see Ref. [16].

Table VI.4: Vertical excitation energies (eV) at rectangular singlet (RS) and square triplet (ST) geometries. The geometries are specified in the footnotes. D_{4h} symmetry labels are shown in parentheses. The $X^1A_g(X^1B_{1g})$ is the lowest state at both geometries.

	$1^3B_{1g}(^3A_{2g})$	$2^1A_g(^1A_{1g})$	$1^1B_{1g}(^1B_{2g})$
RS (D_{2h}) geometry			
PPP-CI/[a]		4.351	3.523
SCF-CI/[5s5p/5s][b]	1.622	4.767	5.984
SCF-CI/3-21(+)G[c]	1.12	4.90	3.46
MCSCF/SVP[d]	1.274	3.715	4.138
H^ν/(4s5p1d/2s1p)[e]	1.44	4.06	3.39
EOM-CCSD/4-31G[f]	1.12	5.36	3.67
EOM-CCSD/cc-pVTZ[g]	1.351	n/a	3.319
EOM-SF-CCSD/cc-pVTZ[g]	1.659	4.369	3.420
ST (D_{4h}) geometry			
SCF-CI/[5s5p/5s][h]	0.590	2.754	4.914
ROKS(BLYP)/TZ2P[i]	-0.208	1.040	0.797
EOM-CCSD/cc-pVTZ[g]	-0.590	n/a	1.534
EOM-SF-CCSD/cc-pVTZ[g]	0.369	1.824	2.143

[a] Ref. [16]; at the geometry from Ref. [127]: R_{C-C}=1.57 Å, $R_{C=C}$=1.34 Å, R_{CH}=1.085 Å, θ_{HCC}=135^o.
[b] Ref. [32]; R_{C-C} = 1.514 Å, $R_{C=C}$=1.338 Å, R_{CH}=1.059 Å, θ_{HCC}=130^o.
[c] Ref. [79]; R_{C-C}=1.526 Å, $R_{C=C}$=1.316 Å, R_{CH}=1.08 Å, θ_{HCC}=135^o.
[d] Ref. [3]; R_{C-C}=1.548 Å, $R_{C=C}$=1.375 Å, R_{CH}=1.085 Å, θ_{HCC}=135^o.
[e] Ref. [156]; at the geometry from Ref. [35]: R_{C-C}=1.567 Å, $R_{C=C}$=1.346 Å, R_{CH}=1.084 Å, θ_{HCC}=134.9^o.
[f] Ref. [93]; R_{C-C}=1.581 Å, $R_{C=C}$=1.323 Å, R_{CH}=1.067 Å, θ_{HCC}=134.7^o.
[g] this work; geometry is shown in Fig. VI.3.
[h] Ref. [32]; R_{CC}=1.424 Å, R_{CH}=1.059Å.
[i] Ref. [74]; unspecified triplet geometry.

Table VI.4 summarizes some of the theoretical results for the vertical excitation energies of cyclobutadiene at the singlet and triplet equilibrium geometries.

The best agreement between the EOM-SF-CCSD valence transitions is with the semi-empirical Parr-Pariser-Pople (PPP) model with the full CI in the π-system [16], as well as with the effective valence shell Hamiltonian (H^ν) method [156]. Note that

the geometries employed in these calculations are very close to the geometries used in this work. While the PPP-CI method is not an accurate structural tool because only π electrons are considered, it may still yield reasonably accurate excitation energies within π-systems due to the high degree of parameterization.

There is an interesting relation between the H^{ν} method and EOM-SF-CCSD. In both cases, the effective Hamiltonian which includes dynamical correlation effects is diagonalized in a smaller configurational subspace. While in EOM-SF-CCSD, the reference and excited state spaces are separated by their spin-projection values (M_s = 1 for the triplet reference, and M_s = 0 for target states), in the H^{ν} approach total configuration space is divided to valence subspace and its orthogonal compliment [156]. This allows to separate the degenerate configurations (π-system) from the rest of the configurational space (σ-system) and treat them in a reasonably balanced fashion without sacrificing π-σ and σ-σ dynamical correlation. This explains the fairly good agreement between the H^{ν} and EOM-SF-CCSD results.

The importance of the π-σ correlation is confirmed by the comparison of SCF-CI results for the open-shell singlet $^1B_{1g}$ state obtained by Buenker and Peyerimhoff [32], and by Fratev *et al.* [79] (see Table VI.4). Buenker and Peyerimhoff included in their CI all configurations derived from distributing the four π electrons among the eight π spin-orbitals. The resulting energy of the $^1B_{1g} \leftarrow X^1A_g$ transition (5.984 eV) is 2.56 eV higher than the corresponding EOM-SF-CCSD value. Moreover, contrarily to the EOM-SF-CCSD results, this state is placed above the 2^1A_g state. The CI space employed by Fratev *et al.* included only single excitations from

HOMO, but these excitations were not limited to the π-system. Inclusion of the excitations to σ-antibonding orbitals results in much better agreement between SCF-CI and EOM-SF-CCSD (3.46 eV and 3.42 eV, respectively).

To conclude, a large basis set and a high level of correlation is required for a proper description of cyclobutadiene. High degeneracy in the π-system, along with strong dynamical π-σ and σ-σ correlation require well balanced treatment of all electrons. This is easily achieved in the presented SF variant of EOM-CCSD. Despite the fact that degeneracy is lifted by rectangular distortions, the ground X^1A_g state is still considerably multi-configurational. This causes traditional single-configurational approaches to fail for transition energies, although it has only a minor effect on the geometry of the ground state.

Chapter VII. EOM-SF-CCSD analytic gradients: equilibrium geometries and transition structures of the low-lying valence states of cuclobutadiene

Here, I present the results of our application of the EOM-SF-CCSD analytic gradients to characterize equilibrium geometries and transition structures for the four low lying valence states of CB, and the energy barrier for the interconversion between the two rectangular ground state structures.

Although the electronic structure of CB was subjected to exhaustive theoretical investigations (see Ref. [147] and Refs.[62-86] therein), no fully converged w.r.t. correlation treatment and one-electron basis set optimized geometries and transition structures have yet been reported. The difficulties originate in multi-configurational character of the low lying electronic states of CB, including the ground state, which results from the quasidegeneracy (or exact degeneracy at the square geometry) in the π-system [16, 147]. Traditionally, this problem was treated by multi-reference methods [3, 15, 35, 74, 117, 180, 204, 206]. Due to the large computational costs of MR methods with proper account of dynamical correlation, previously reported results

were obtained using relatively small bases. Alternatively, electronic structure of CB and other diradical systems can be described by starting from dication or dianion reference, and treating target states by diagonalizing the coupled-cluster similarity transformed Hamiltonian in the basis of configurations that contain the same number of electrons as the neutral system (EOM-DIP-CC and EOM-DEA-CC methods, respectively) [183,253]. These methods are single-reference, and a large basis set can be employed for moderate systems when the CC amplitudes are truncated at double excitations. However, insufficient account of orbital relaxation upon ionization may result in large errors in optimized geometries [245]. Finally, the EOM-SF-CCSD method provides balanced account of dynamical and non-dynamical correlation for all low-lying states of CB [147], and can be employed with large one-electron basis sets.

The optimized geometries and transition structures of CB are presented in Fig. VII.1.

Molecular orbital picture for the four states is shown in Fig. VII.2.

The largest basis set we employ is cc-pVTZ on carbon and cc-pVDZ on hydrogen [65], with all orbitals being active. Additional calculation of the optimized geometry for the rectangular ground X^1A_g state with the full cc-pVTZ basis set on both carbon and hydrogen atoms yields at most 0.002 Å difference in the CC bond lengths relative to the mixed basis set.

As the results presented in Fig. VII.1 demonstrate, the increase in the basis set size leads to more compact structures for all the states considered: C-C bond lengths

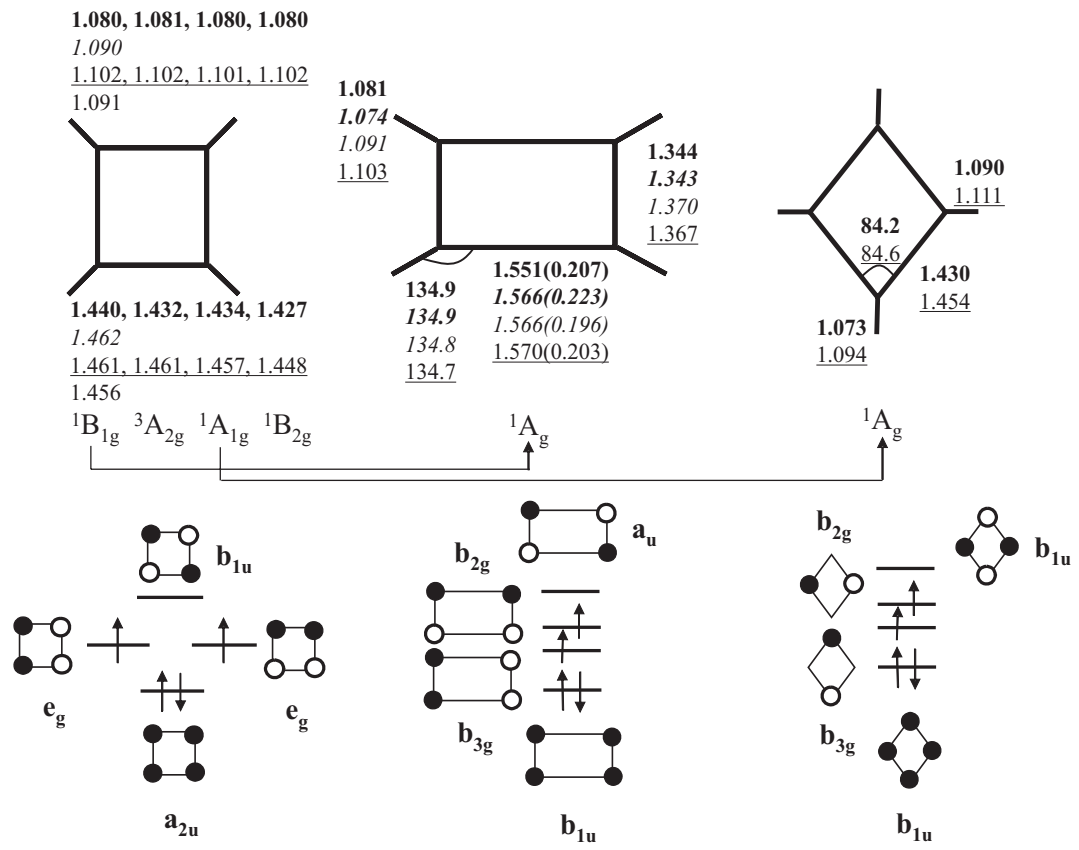

Figure VII.1: Optimized geometries and transition structures of the four low lying valence states of cyclobutadiene. For the square geometry, the values of C-H and C-C bond lengths, Å, for different states are separated by commas. The results are shown for the following methods (from top to bottom): EOM-SF-CCSD/cc-pVTZ(mixed), EOM-SF-CCSD/[3s2p1d/2s], MR-CCSD/[3s2p1d/2s], MR-BWCCSD/cc-pVDZ. The parameters for the rectangular ground state equilibrium geometry are shown for the following methods (starting from top): EOM-SF-CCSD/cc-pVTZ(mixed), CCSD(T)/cc-pVTZ, EOM-SF-CCSD/[3s2p1d/2s], MR-CCSD/[3s2p1d/2s]. Only the second closed-shell singlet is stabilized by the rhombic distortion, and the corresponding equilibrium geometries are shown for EOM-SF-CCSD/cc-pVTZ(mixed) (upper number) and MR-CCSD/[3s2p1d/2s] (lower number). On the lower panel, π molecular orbitals and electronic configuration of triplet reference are shown.

calculated with cc-pVTZ basis set are 0.02-0.03 Å shorter than those calculated with the [3s2p1d/2s] basis set employed by Balková and Bartlett [15]. This conclusion

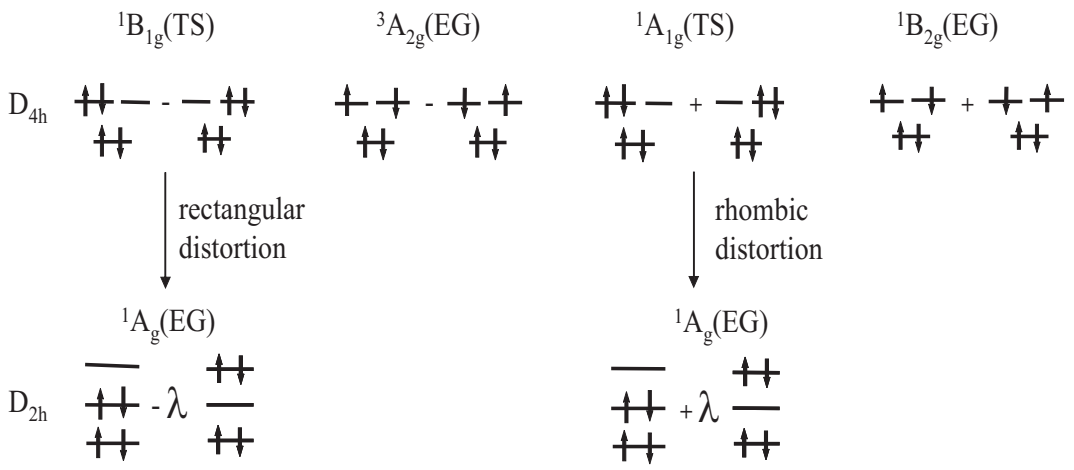

Figure VII.2: Electronic configurations of the four low lying states of CB at the square geometry, and their change upon stabilizing distortions. In parentheses, the type of molecular geometry stationary points is indicated for each state: TS stands for a transition structure, while EG denotes an equilibrium geometry.

is confirmed by the EOM-SF-CCSD/[3s2p1d/2s] geometry optimization for the rectangular and square ground state CB, which gives at most 0.004 Å deviation from MR-CCSD/[3s2p1d/2s] C-C bond lengths [15]. Shortening of the equilibrium bond lengths upon increase of the basis set size is due to the increased number of polarization functions, which allows for more ionic character of the bonds.

Another interesting observation is that the multi-configurational character of the rectangular ground state has small but noticeable effect on the equilibrium C-C bond lengths. Comparison between the CCSD(T) and EOM-SF-CCSD results (see Fig. VII.1) shows that CCSD(T) gives longer single C-C bond (1.566 Å vs. 1.551 Å), but almost the same double C-C bond (1.343 Å vs. 1.344 Å for EOM-SF-CCSD). This difference indicates that the single reference CCSD(T) method underestimates contribution of the second diradical configuration (see Fig. VII.2) in the overall wave function, because this configuration is doubly excited w.r.t. the first one. On the other

hand, both configurations are single spin-flipping excitations from high-spin triplet reference, and are correlated equally well in EOM-SF-CCSD.

The EOM-SF-CCSD/(cc-pVTZ/cc-pVDZ) energy difference between the optimized rectangular and square ground state structures (the automerization barrier) is 7.6 kcal/mol. This value does not include the zero-point vibrational energy. This result is very close to 7.4 kcal/mol obtained by the extrapolation of the MR-BWCCSD energies in the cc-pVDZ and cc-pVTZ bases to the basis set limit [206].

General conclusions

The results presented in this dissertation clearly demonstrate the advantages of the equation-of-motion coupled-cluster methods over other *ab initio* methods. These are the following: (i) the EOM-CC model is *size-consistent*, i.e., *its quality does not degrade with the increase of system size*; (ii) it is bivariational, i.e., the equations are well defined and derived within a mathematically rigorous procedure, which suggests that a stable algorithm converging fast to the solutions exists; (iii) it is single-reference, i.e., does not involve an active space, which is on one hand not well defined, but can greatly influence the results of calculations on the other; (iv) it is state universal (or multi-state), i.e., allows for simultaneous calculation of several target states with uniform accuracy independent of their character, which is especially important in the case of radicals, where there are low-lying both Rydberg and valence states; (v) EOM-CC separates correlation effects in the reference and in the target states, providing means for a compact representation of electronic wave functions, which greatly simplifies the assignment of the electronic transitions in terms of occupation change of bonding, antibonding, non-bonding, and Rydberg orbitals with respect to the reference determinant; (vi) EOM-CC describes both dynamic and

non-dynamic correlation effects simultaneously, thus providing a balanced treatment of the electron correlation problem within one computational scheme; (vii) the EOM-CC analytic derivatives and other properties can be readily derived and implemented largely utilizing the same computer code which was used for the EOM-CC energy calculations. Firm theoretical foundations, clear architecture, and flexibility make the EOM-CC model a versatile tool not only for accurate calculations of electronic states of molecular systems, but also for first-principle studies of the nature of electron correlation and further development of *ab initio* methods.

Future work

As was demonstrated in Section I.1, the EOM-CC model is exact, i.e., equivalent to FCI, if the excitation operator $\hat{R}$ in the EOM part is not truncated. However, the truncation poses limitations on the area of applicability of EOM-CC. For example, EOM-EE-CCSD, in which the operator $\hat{R}$ is truncated at double excitations, does not describe doubly excited states. Also, when a double bond is broken, it is not enough to have single spin-flipping excitations in EOM-SF-CCSD to describe the corresponding PES. From this perspective, it is worth trying to extend EOM-SF-CC model to include higher spin-flipping excitations in the EOM part, as it would allow one to account for dynamical correlation in systems with increasing level of degeneracy (e.g., double bond breaking, multi-radical systems). However, there are two main problems to be faced along this straightforward rout. First, it is unclear how to unambiguously determine the lowest excitation level required for a given system. Second, the computational cost rises steeply with increasing the level of excitation (e.g., inclusion of full triple excitations into the EOM part of EOM-CCSD results in the increase of computational scaling from N^6 to N^8). The solution of these problems

would also yield in developing a procedure for automatic state averaging, generation of active space, and orbital optimization for multireference coupled-cluster methods.

In my opinion, the problem of determining the minimum number of spin-flipping excitations required for an accurate description of a degenerate system could be approached by studying the relation between the spin contamination of the reference and the level of degeneracy in the system. If one could retrieve the information about the degeneracy from the reference, it would give the optimal orbitals and the number of spin-flipping excitations at the low computational cost of the Hartree-Fock model.

The second problem of increasing computational cost as the level of degeneracy, and, consequently, the level of excitation increases, could be solved by separating the spin-flipping excitations from the additional excitations required for correlating the target states, preserving their spin symmetry. In other words, one could separate excitations within and outside the active space, as is done in multireference methods. The important difference, however, is that we know exactly the class of states the new method is applicable to, and the orbitals and active space are no longer free parameters.

With the growth of computer power and resources, the area of applicability of EOM-CC methods rapidly extends. The EOM-SF-CC model could be very useful, for example, for accurate treatment of the problem of interaction of an arbitrary (not molecular) few electron degenerate system with molecules. This problem is closely related to the interaction of the molecules with “artificial atoms”, quantum dots.

Reference List

[1] Basis sets were obtained from the Extensible Computational Chemistry Environment Basis Set Database, Version , as developed and distributed by the Molecular Science Computing Facility, Environmental and Molecular Sciences Laboratory which is part of the Pacific Northwest Laboratory, P.O. Box 999, Richland, Washington 99352, USA, and funded by the U.S. Department of Energy. The Pacific Northwest Laboratory is a multi-program laboratory operated by Battelle Memorial Institue for the U.S. Department of Energy under contract DE-AC06-76RLO 1830. Contact David Feller or Karen Schuchardt for further information.

[2] NIST Chemistry WebBook. webbook.nist.gov/chemistry/.

[3] H. Årgen, N. Correia, A. Flores-Riveros, and H.J.AA. Jensen. Direct restricted-step MCSCF calculations on the structure and spectrum of cyclobutadiene. *Int. J. Quant. Chem. Symp.*, 19:237–246, 1986.

[4] W.D. Allen, D.A. Horner, R.L. Dekock, R.B. Remington, and H.F. Schaefer III. The lithium superoxide radical: Symmetry breaking phenomena and potential energy surfaces. *Chem. Phys.*, 133:11–45, 1989.

[5] N.L. Allinger, C. Gilardeau, and L.W. Chow. A theoretical study of the structures and electronic spectra of cyclobutadiene and dimethylenecyclobutene. *Tetrahedron*, 24:2401–2406, 1968.

[6] N.L. Allinger and J.C. Tai. Further theoretical studies of the structure and electronic spectrum of cyclobutadiene. *Theor. Chim. Acta*, 12:29–33, 1968.

[7] T. Amano, P.F. Bernath, C. Yamada, Y. Endo, and E. Hirota. Difference frequency laser spectroscopy of the ν_3 band of the CH_3 radical. *J. Chem. Phys.*, 77:5284–5287, 1982.

[8] L. Andrews, J.M. Dyke, N. Jonathan, N. Keddar, and A. Morris. Photoelectron spectroscopic study of the ground states of CH_2Cl^+, $CHCl_2^+$, and $CHFCl^+$. *J. Am. Chem. Soc.*, 106:299–303, 1984.

[9] L. Andrews, J.M. Dyke, N. Jonathan, N. Keddar, A. Morris, and A. Ridha. A photoelectron spectroscopic study of the ground states of CH_2f^+ and CD_2F^+. *J. Phys. Chem.*, 88:2364–2368, 1984.

[10] L. Andrews and D.W. Smith. Matrix infrared spectrum and bonding in monochloromethyl radical. *J. Chem. Phys.*, 53(7):2956–2966, 1970.

[11] Y. Arasaki, K. Takatsuka, K. Wang, and V. McKoy. Femtosecond energy- and angle-resolved photoelectron spectroscopy. *J. Chem. Phys.*, 112:8871–8884, 2000.

[12] B.R. Arnold and J. Michl. Ultraviolet and polarized infrared spectroscopy of matrix-isolated cyclobutadiene and its isotopomers. *J. Phys. Chem.*, 97:13348–13354, 1993.

[13] K.K. Baeck. The analytic gradient for the equation-of-motion coupled-cluster energy with a reduced molecular orbital space: An application for the first excited state of formaldehyde. *J. Chem. Phys.*, 112:1–4, 2000.

[14] K.L. Bak, J. Gauss, P. Jørgensen, J. Olsen, T. Helgaker, and J.F. Stanton. The accurate determination of molecular equilibrium structures. *J. Chem. Phys.*, 114:6548–6556, 2001.

[15] A. Balkova and R.J. Bartlett. A multireference coupled-cluster study of the ground state and lowest excited states of cyclobutadiene. *J. Chem. Phys.*, 101:8972–8987, 1994.

[16] T. Bally and S. Masamune. Cyclobutadiene. *Tetrahedron*, 36:343–370, 1980.

[17] L.A. Barnes and R. Lindh. Symmetry breaking in O_4^+: an application of the brueckner coupled-cluster method. *Chem. Phys. Lett.*, 223:207–214, 1994.

[18] R.J. Bartlett and J.F. Stanton. Applications of post-Hartree-Fock methods: A tutorial. *Rev. Comp. Chem.*, 5:65–169, 1994.

[19] F. Bernardi, N.D. Epiotis, W. Cherry, H.B. Schlegel, M.-H. Whangbo, and S. Wolfe. A molecular orbital interpretation of the static, dynamic, and chemical properties of CH_2X radicals. *J. Am. Chem. Soc.*, 98:469–478, 1976.

[20] D.L. Beveridge, P.A. Dobosh, and J.A. Pople. Molecular-orbital theory of geometry and hyperfine coupling constants of fluorinated methyl radicals. *J. Chem. Phys.*, 48:4802–4803, 1968.

[21] J.F. Black and I. Powis. Rotational structure and predissociation dynamics of the methyl $4p_z$(v=0) Rydberg state investigated by resonance enhanced multiphoton ionization spectroscopy. *J. Chem. Phys.*, 89:3986–3992, 1988.

[22] O. Bludsky, K.L. Bak, P. Jørgensen, and V. Spirko. Ab initio calculations of anharmonic vibrational transition intensities of trans-2,3-dideuteriooxirane. *J. Chem. Phys.*, 103:10110–10115, 1995.

[23] O. Bludsky, V. Spirko, R. Kobayashi, and P. Jørgensen. An ab initio quartic force field and the fundamental frequencies of o-benzyne. *Chem. Phys. Lett.*, 228:568–574, 1994.

[24] V. Bonačić-Koutecký, J. Koutecký, and J. Michl. Neutral and charged biradicals, zwitterions, funnels in S_1, and proton translocation: Their role in photochemistry, photophysics, and vision. *Angew. Chem. Int. Ed. Engl.*, 26:170–189, 1987.

[25] W.T. Borden, editor. *Diradicals*. Wiley, New York, 1982.

[26] W.T. Borden and E.R. Davidson. Effects of electron repulsion in conjugated hydrocarbon diradicals. *J. Am. Chem. Soc.*, 99:4587–4594, 1977.

[27] W.T. Borden, E.R. Davidson, and P. Hart. The potential energy surfaces for the lowest singlet and triplet states of cyclobutadiene. *J. Am. Chem. Soc.*, 100:388–392, 1978.

[28] P. Botschwina, J. Flesch, and W. Meyer. Spectroscopic properties of the methyl radical calculated from UHF SCEP wavefunctions. *Chem. Phys.*, 74:321–338, 1983.

[29] P. Botschwina, E. Schick, and M. Horn. The barrier to dissociation in the $\tilde{B}^2A_1'$ state of the methyl radical. *J. Chem. Phys.*, 98:9215, 1993.

[30] J.M. Bowman. Self-consistent field energies and wavefunctions for coupled oscillators. *J. Chem. Phys.*, 68:608–610, 1978.

[31] J.M. Bowman. The self-consistent-field approach to polyatomic vibrations. *Acc. Chem. Res.*, 19:202–208, 1986.

[32] R.J. Buenker and S.D. Peyerimhoff. *ab initio* study on the stability and geometry of cyclobutadiene. *J. Chem. Phys.*, 48:354–373, 1968.

[33] E.F.C. Byrd, C.D. Sherrill, and M. Head-Gordon. The theoretical prediction of molecular radical species: a systematic study of equilibrium geometries and harmonic vibrational frequencies. *J. Phys. Chem. A*, 105(42):9736–9747, 2001.

[34] M.R. Cameron and S.H. Kable. A new design for a simple and effective pyrolysis nozzle in a supersonic free jet. *Rev. Sci. Instrum.*, 67:283–287, 1996.

[35] P. Carsky, R.J. Bartlett, G. Fitzgerald, J. Noga, and V. Spirko. *Ab initio* calculations on the energy of activation and tunneling in the automerization of cyclobutadiene. *J. Chem. Phys.*, 89:3008–3015, 1988.

[36] T.G. Carver and L. Andrews. Matrix infrared spectrum and bonding in dibromomethyl radical. *J. Chem. Phys.*, 50(10):4223–4234, 1969.

[37] T.G. Carver and L. Andrews. Matrix infrared spectrum and bonding in dichlormethyl radical. *J. Chem. Phys.*, 50(10):4235–4245, 1969.

[38] L.S. Cederbaum and W. Domcke. Theoretical aspects of ionization potentials and photoelectron spectroscopy: A Green's function approach. *Adv. Chem. Phys.*, 36:205–344, 1977.

[39] P. Celani and H.-J. Werner. Analytical energy gradients for internally contracted second-order multireference perturbation theory. *J. Chem. Phys.*, 119:5044–5057, 2003.

[40] G.M. Chaban and J.O. Jung ad R.B. Gerber. Ab initio calculation of anharmonic vibrational states of polyatomic systems: Electronic structure combined with vibrational self-consistent field. *J. Chem. Phys.*, 111(5):1823–1829, 1999.

[41] G.M. Chaban and R.B. Gerber. Anharmonic vibrational spectroscopy of the glycine-water complex: Calculations for ab-initio, empirical, and hybrid quantum mechanics/molecular mechanics potentials. *J. Chem. Phys.*, 115:1340–1348, 2001.

[42] C.K. Chong, X. Zheng, and D.L. Phillips. Transient resonance raman and density functional theory investigation of bromomethyl radical. *Chem. Phys. Lett.*, 328:113–118, 2000.

[43] J. Cizek. On the correlation problem in atomic and molecular systems. Calculation of wavefunction components in Ursell-type expansion using quntum-field theoretical methods. *J. Chem. Phys.*, 45:4256–4266, 1966.

[44] J. Cizek. *Adv. Chem. Phys.*, 14:35, 1969.

[45] T. Clark, J. Chandrasekhar, and P.V.R. Schleyer. Efficient diffuse function-augmented basis sets for anion calculations. III. The 3-21+g basis set for first-row elements, li-f. *J. Comput. Chem.*, 4:294–301, 1983.

[46] R.D. Cohen and C.D. Sherrill. The performance of density functional theory for equilibrium molecular properties of symmetry breaking molecules. *J. Chem. Phys.*, 114:8257–8269, 2001.

[47] D.C. Comeau and R.J. Bartlett. The equation-of-motion coupled-cluster method. Applications to open- and closed-shell reference states. *Chem. Phys. Lett.*, 207:414–423, 1993.

[48] D.P. Craig. Electronic levels in simple conjugated systems I. Configuration interaction in cyclobutadiene. *Proc. R. Soc. London A*, 202:498–506, 1950.

[49] T.D. Crawford and J.F. Stanton. Some surprising failures of Brueckner coupled cluster theory. *J. Chem. Phys.*, 112:7873–7879, 2000.

[50] T.D. Crawford, J.F. Stanton, W.D. Allen, and H.F. Schaefer III. Hartree-Fock orbital instability envelopes in highly correlated single-reference wave functions. *J. Chem. Phys.*, 107:10626–10632, 1997.

[51] T.D. Crawford, J.F. Stanton, P.G. Szalay, and H.F. Schaefer III. The $\tilde{C}^2A_2$ excited state of NO_2: Evidence for a C_s equilibrium structure and a failure of some spin-restricted reference wavefunctions. *J. Chem. Phys.*, 107:2525–2528, 1997.

[52] T.D. Crawford, S.S. Wesolowski, E.F. Valeev, R.A. King, M.L. Leininger, and H.F. Schaefer III. *The past, present, and future of quantum chemistry. Chemistry for the 21st Century*, pages 219–246. Wiley-VCH Verlag GmbH, Weinheim, Germany, 2001.

[53] S.M. Dancoff. Non-adiabatic meson theory of nuclear forces. *Phys. Rev.*, 78:382–385, 1950.

[54] E.R. Davidson. The iterative calculation of a few of the lowest eigenvalues and corresponding eigenvectors of large real-symmetric matrices. *J. Comput. Phys.*, 17:87–94, 1975.

[55] E.R. Davidson and W.T. Borden. Symmetry breaking in polyatomic molecules: Real and artifactual. *J. Phys. Chem.*, 87:4783–4790, 1983.

[56] S. Davis, D.T. Anderson G. Duxbury, and D.J. Nesbitt. Jet-cooled molecular radicals in slit supersonic discharges: Sub-Doppler infrared studies of methyl radical. *J. Chem. Phys.*, 107:5661–5675, 1997.

[57] D.V. Dearden, J.W. Hudgens, R.D. Johnson III, B.P. Tsai, and S.A. Kafafi. Spectroscopic and ab initio studies of difluoromethyl radicals and cations. *J. Phys. Chem.*, 96:585–594, 1992.

[58] J.J. DeCorpo, D.A. Bafus, and J.L. Franklin. *J. Chem. Thermodyn.*, 3:125, 1971.

[59] A.V. Demyanenko, A.B. Potter, V. Dribinski, and H. Reisler. NO angular distributions in the photodissociation of $(NO)_2$ at 213 nm: Deviations from axial recoil. *J. Chem. Phys.*, 117:2568–2577, 2002.

[60] M.J.S. Dewar and G.J. Gleicher. Self-consistent field molecular orbital calculations for cyclobutadiene. *J. Am. Chem. Soc.*, 87:3255–3256, 1965.

[61] M.J.S. Dewar and A. Komornicki. Ground states of molecules. 36. The cyclobutadiene problem and MINDO/3 calculations of molecular vibration frequencies. *J. Am. Chem. Soc.*, 99:6174–6179, 1977.

[62] D.A. Dixon, D. Feller, and K.A. Peterson. Accurate calculations of the electron affinity and ionization potential of the methyl radical. *J. Phys. Chem. A*, 101:9405–9409, 1997.

[63] V. Dribinski, A.V. Demyanenko, A.B. Potter, and H. Reisler. Photodissociation dynamics of the CH_2Cl radical: Ion imaging studies of the $Cl+CH_2$ channel. *J. Chem. Phys.*, 115(16):7474–7484, 2001.

[64] V. Dribinski, A. Ossadtchi, V.A. Mandelshtam, and H. Reisler. Reconstruction of Abel-transformable images: The Gaussian basis set expansion Abel transform method. *Rev. Sci. Instrum.*, 73:2634–2642, 2002.

[65] T.H. Dunning. Gaussian basis sets for use in correlated molecular calculations. I. The atoms boron through neon and hydrogen. *J. Chem. Phys.*, 90:1007–1023, 1989.

[66] J. Dyke, N. Jonathan, E. Lee, and A. Morris. Vacuum ultraviolet photoelectron spectroscopy of transient species. *J. Chem. Soc., Faraday Trans. 2*, 72:1385–1396, 1976.

[67] K. Emrich. An extension of the coupled-cluster formalism to excited states (I). *Nucl. Phys.*, A351:379–396, 1981.

[68] Y. Endo, S. Saito, and E. Hirota. The microwave spectrum of the chlormethyl radical, CH_2Cl. *Can. J. Phys.*, 62:1347–1360, 1984.

[69] Y. Endo, C. Yamada, S. Saito, and E. Hirota. The microwave spectrum of the fluoromethyl radical, CH_2F. *J. Chem. Phys.*, 79:1605–1611, 1983.

[70] L. Engelbrecht and B. Liu. An orthogonal orbital MCSCF plus CI treatment of molecular symmetry breaking. I. The lowest $^3B_2$ and $^3A_2$ states of CO_2. *J. Chem. Phys.*, 78:3097–3106, 1983.

[71] S.T. Epstein. *The variation method in quantum chemistry*. Academic Press, New York, 1974.

[72] R.W. Fessenden. Electron spin resonance spectra of some isotopically substituted hydrocarbon radicals. *J. Phys. Chem.*, 71:74–83, 1967.

[73] R.W. Fessenden and R.H. Schuler. Esr spectra and structure of the fluorinated methyl radicals. *J. Chem. Phys.*, 43:2704–2712, 1965.

[74] M. Filatov and S. Shaik. Application of spin-restricted open-shell Kohn-Sham method to atomic and molecular multiplet states. *J. Chem. Phys.*, 110:116–125, 1999.

[75] B.J. Finlayson-Pitts and J.N. Pitts. *Chemistry of the Upper and Lower Atmosphere: Theory, Experiments, and Applications*. Academic Press, New York, 1999.

[76] J. Finley, P.-Å. Malmqvist, B.O. Roos, and L. Serrano-Andrés. The multi-state caspt2 method. *Chem. Phys. Lett.*, 288:299–306, 1998.

[77] J.B. Foresman, M. Head-Gordon, J.A. Pople, and M.J. Frisch. Toward a systematic molecular orbital theory for excited states. *J. Phys. Chem.*, 96:135–149, 1992.

[78] J.S. Francisco and M.M. Maricq. Atmospheric photochemistry of alternative halocarbons. In *Advances in photochemistry*, volume 20, pages 79–163. John Wiley & Sons, Inc, 1995.

[79] F. Fratev, V. Monev, and R. Janoschek. *Ab initio* study of cyclobutadiene in excited states: Optimized geometries, electronic transitions and aromaticities. *Tetrahedron*, 38:2929–2932, 1982.

[80] M.J. Frisch, J.A. Pople, and J.S. Binkley. Self-consistent molecular orbital methods 25. Supplementary functions for Gaussian basis sets. *J. Chem. Phys.*, 80:3265–3269, 1984.

[81] F. Furche and R. Ahlrichs. Adiabatic time-dependent density fuctional methods for excited state properties. *J. Chem. Phys.*, 117:7433–7447, 2002.

[82] J. Gauss, D. Cremer, and J.F. Stanton. The r_e structure of cyclopropane. *J. Phys. Chem. A*, 104:1319–1324, 2000.

[83] J. Gauss and J.F. Stanton. The equilibrium structure of benzene. *J. Phys. Chem. A*, 104:2865–2868, 2000.

[84] J. Gauss, J.F. Stanton, and R.J. Bartlett. Coupled-cluster open-shell analytic gradients: Implementation of the direct product decomposition approach in energy gradient calculations. *J. Chem. Phys.*, 95:2623–2638, 1991.

[85] J. Geertsen, M. Rittby, and R.J. Bartlett. The equation-of-motion coupled-cluster method: excitation energies of Be and CO. *Chem. Phys. Lett.*, 164:57–62, 1989.

[86] R.B. Gerber and M.A. Ratner. A semiclassical self-consistent field (SC SCF) approximation for eigenvalues of coupled-vibration systems. *Chem. Phys. Lett.*, 68:195–198, 1979.

[87] R.B. Gerber and M.A. Ratner. Self-consistent-field methods for vibrational excitations in polyatomic systems. *Adv. Chem. Phys.*, 70:97–132, 1998.

[88] E.D. Glendening, J.K. Badenhoop, A.E. Reed, J.E. Carpenter, and F. Weinhold. NBO 4.0. Theoretical Chemistry Institute, University of Wisconsin, Madison, WI, 1996.

[89] M.N. Glukhovtsev, S. Laiter, and A. Pross. Thermochemistry of cyclobutadiene and tetrahedrane: A high-level computational study. *J. Phys. Chem.*, 99:6828–6831, 1995.

[90] M.S. Gordon. Excited states and photochemistry of saturated molecules. Extended basics calculations of the $1B_1$ ($1T_2$) state of methane. *Chem. Phys. Lett.*, 52:161–167, 1977.

[91] M.S. Gordon and J.W. Caldwell. Excited states of saturated molecules. In B. Pullman and N. Goldblum, editors, *Excited states in organic chemistry and biochemistry*, pages 257–270. D. Reidel publishing company, Dordrecht, Holland, 1977.

[92] S.R. Gwaltney and R.J. Bartlett. Gradients for the partitioned equation-of-motion coupled-cluster method. *J. Chem. Phys.*, 110:62–71, 1999.

[93] R.C. Haddon and G.R.J. Williams. A molecular orbital study of the electronic structure and spectrum of rectangular (d_{2h}) cyclobutadiene. *J. Am. Chem. Soc.*, 97:6582–6584, 1975.

[94] N.C. Handy and H.F. Schaefer III. On the evaluation of analytic energy derivatives for correlated wave functions. *J. Chem. Phys.*, 81:5031–5033, 1984.

[95] M. Head-Gordon and T.J. Lee. Single reference coupled cluster and perturbation theories of electronic excitation energies. In R.J. Bartlett, editor, *Modern Ideas in Coupled Cluster Theory*. World Scientific, Singapore, 1997.

[96] M. Head-Gordon, R.J. Rico, M. Oumi, and T.J. Lee. A doubles correction to electronic excited states from configuration interaction in the space of single substitutions. *Chem. Phys. Lett.*, 219:21–29, 1994.

[97] T. Helgaker, P. Jørgensen, and J. Olsen. *Molecular electronic structure theory*. John Wiley & Sons, 2000.

[98] G. Herzberg. *Molecular spectroscopy and molecular structure; Electronic spectra end electronic structure of polyatomic molecules*, volume III. van Nostrand Reinhold: New York, 1966.

[99] G. Herzberg and J. Shoosmith. Absorption spectrum of free CH_3 and CD_3 radicals. *Can. J. Phys.*, 34:523, 1956.

[100] B.A. Hess Jr., P. Carsky, and L.J. Schaad. *Ab initio* second-order Möller-Plesset calculation of the vibrational spectra of cyclobutadiene and its isotopic derivatives. *J. Am. Chem. Soc.*, 105:695–701, 1983.

[101] P.C. Hiberty. The destortive tendencies of delocalized π electronic systems. Benzene, cyclobutadiene and related heteroannulenes. *Top. Curr. Chem.*, 153:27–39, 1990.

[102] P.C. Hiberty, G. Ohanessian, S.S. Shaik, and J.P. Flament. The delocalization of π electronic systems as a destabilizing constraint imposed by the σ frame. Allyl, benzene, cyclobutadiene and related heteroannulenes. *Pure Appl. Chem.*, 65:35–45, 1993.

[103] K. Hirao and H. Nakatsuji. A generalization of the Davidson's method to large nonsymmetric eigenvalue problems. *J. Comput. Phys.*, 45:246–254, 1982.

[104] S. Hirata and M. Head-Gordon. Time-dependent density functional theory within the Tamm-Dancoff approximation. *Chem. Phys. Lett.*, 314:291–299, 1999.

[105] S. Hirata, M. Nooijen, and R.J. Bartlett. High-order determinantal equation-of-motion coupled-cluster calculations for electronic excited states. *Chem. Phys. Lett.*, 326:255–262, 2000.

[106] H.J.Aa. Jensen, P. Jørgensen, H. Ågren, and J. Olsen. Second-order Møller-Plesset perturbation theory as a configuration and orbital generator in multi-configuration self-consistent field calculations. *J. Chem. Phys.*, 88:3834–3839, 1988.

[107] J.L. Holmes and F.P. Lossing. Heats of formation and bond dissociation energies in halogen-substituted methyl and ethyl radicals. *J. Am. Chem. Soc.*, 110:7343–7345, 1988.

[108] P.L. Holt, K.E. McCurdy, R.B. Weisman, J.S. Adams, and P.S. Engel. Transient CARS spectroscopy of the ν_1 band of methyl radical. *J. Chem. Phys.*, 81:3349–3350, 84.

[109] T.R. Horn, R.B. Gerber, and M.A. Ratner. Vibrational states of very floppy clusters — approximate separability and the choice of good curvilinear coordinates for $XeHe_2$, I_2He. *J. Chem. Phys.*, 91:1813–1823, 1989.

[110] J. Hrušák and S. Iwata. The vibrational spectrum of $H_2O_2^+$ radical cation: An illustration of symmetry breaking. *J. Chem. Phys.*, 106:4877–4888, 1997.

[111] J.W. Hudgens, T.G. DiGiuseppe, and M.C. Lin. Two photon resonance enhanced multiphoton ionization spectroscopy and state assignments of the methyl radical. *J. Chem. Phys.*, 79:571–582, 1983.

[112] J.W. Hudgens, C.S. Dulcey, G.R. Long, and D.J. Bogan. Multiphoton ionization spectra of radical products in the F(^2P)+ketene system: Spectral assignments and formation reaction for CH_2F, observation of CF and CH. *J. Chem. Phys.*, 87(8):4546–4558, 1987.

[113] J.W. Hudgens, R.D. Johnson III, and B.P. Tsai. New electronic spectra of the CHFCl radical observed with resonance enhanced multiphoton ionization. *J. Chem. Phys.*, 98:1925–1932, 1993.

[114] C.F. Jackels and E.R. Davidson. The two lowest energy ^{2}A′ states of NO_2. *J. Chem. Phys.*, 64:2908–2917, 1976.

[115] M.E. Jacox. Vibrational and electronic energy levels of polyatomic transient molecules. *J. Phys. Chem. Ref. Data*, pages 1–461, 1994. Monograph No. 3.

[116] M.E. Jacox and D.E. Milligan. Matrix-isolation study of the vacuum-ultraviolet photolysis of methyl chloride and methylene chloride. Infrared and ultraviolet spectra of the free radicals CCl, H_2CCl, and CCl_2. *J. Chem. Phys.*, 53(7):2688–2701, 1970.

[117] J.A. Jafri and M.D. Newton. Potential energy surfaces of cyclobutadiene: *Ab initio* SCF and CI calculations for the low-lying singlet and triplet states. *J. Am. Chem. Soc.*, 100:5012–5017, 1978.

[118] R.D. Johnson III and J.F. Hudgens. Structural and thermochemical properties of hydroxymethyl (CH_2OH) radicals and cations derived from observations of $\tilde{B}\,^2A'$(3p)$\leftarrow \tilde{X}\,^2A''$ electronic spectra and from ab initio calculations. *J. Phys. Chem.*, 100:19874–19890, 1996.

[119] J.O. Jung and R.B. Gerber. Vibrational wave functions and energy levels of large anharmonic clusters: A vibrational SCF study of Ar_{13}. *J. Chem. Phys.*, 105:10682–10690, 1996.

[120] J.O. Jung and R.B. Gerber. Vibrational wave functions and spectroscopy of $(H_2O)_n$, n=2,3,4,5: Vibrational self-consistent field with correlation corrections. *J. Chem. Phys.*, 105:10332–10348, 1996.

[121] S.A. Kafafi and J.W. Hudgens. Ab initio calculations of the electronic structure and vibrational frequencies of the dichlormethyl radical and cation. *J. Phys. Chem.*, 93:3474–3479, 1989.

[122] U. Kaldor. Symmetry breaking in radicals: NO_2, NS_2 and NO_3. *Chem. Phys. Lett.*, 185:131–135, 1991.

[123] P.B. Kelly and S.G. Westre. Resonance Raman spectroscopy of the methyl radical. *Chem. Phys. Lett.*, 151:253–257, 1988.

[124] H. Koch, H. Jørgen Aa. Jensen, P. Jørgensen, and T. Helgaker. Excitation energies from the coupled clusters singles and doubles linear response functions (CCSDLR). Applications to Be, CH^+, CO, and H_2O. *J. Chem. Phys.*, 93(5):3345–3350, 1990.

[125] D.W. Kohn, H. Clauberg, and P. Chen. Flash pyrolysis nozzle for generation of radicals in a supersonic jet expansion. *Rev. Sci. Instrum.*, 63:4003–4005, 1992.

[126] H. Kollmar and V. Staemmler. A theoretical study of the structure of cyclobutadiene. *J. Am. Chem. Soc.*, 99:3583–3587, 1977.

[127] H. Kollmar and V. Staemmler. On the structure of cyclobutadiene. Theoretical determination of its infraread spectrum. *J. Am. Chem. Soc.*, 100:4304–4305, 1978.

[128] J. Kong, C.A. White, A.I. Krylov, C.D. Sherrill, R.D. Adamson, T.R. Furlani, M.S. Lee, A.M. Lee, S.R. Gwaltney, T.R. Adams, C. Ochsenfeld, A.T.B. Gilbert, G.S. Kedziora, V.A. Rassolov, D.R. Maurice, N. Nair, Y. Shao, N.A. Besley, P. Maslen, J.P. Dombroski, H. Daschel, W. Zhang, P.P. Korambath, J. Baker, E.F.C. Bird, T. Van Voorhis, M. Oumi, C.-P. Hsu S. Hirata, N. Ishikawa, J. Florian, A. Warshel, B.G. Johnson, P.M.W. Gill, M. Head-Gordon, and J.A. Pople. Q-Chem 2.0: A high performance ab initio electronic structure program package. *J. Comput. Chem.*, 21(16):1532–1548, 2000.

[129] H. Konishi and K. Morokuma. *Ab initio* studies of hyperfine coupling in free radicals. II. Methyl and fluoromethyl radicals, and α-fluorine spin coupling parameters. *J. Am. Chem. Soc.*, 94:5603–5612, 1972.

[130] D.D. Konowalow and J.L. Fish. The molecular electronic structure of the twenty-six lowest lying states of Li_2 at short and intermediate internuclear separations. *Chem. Phys.*, 84:463–475, 1984.

[131] K. Kowalski and P. Piecuch. The active space equation-of-motion coupled-cluster methods for excited electronic states: the EOMCCSDt approach. *J. Chem. Phys.*, 113(19):8490–8502, 2000.

[132] K. Kowalski and P. Piecuch. The active space equation-of-motion coupled-cluster methods for excited electronic states: Full EOMCCSDt. *J. Chem. Phys.*, 115(2):643–651, 2001.

[133] R. Krishnan, J.S. Binkley, R. Seeger, and J.A. Pople. Self-consistent molecular orbital methods. XX. A basis set for correlated wave functions. *J. Chem. Phys.*, 72:650, 1980.

[134] A.I. Krylov. Size-consistent wave functions for bond-breaking: The equation-of-motion spin-flip model. *Chem. Phys. Lett.*, 338:375–384, 2001.

[135] A.I. Krylov. Spin-flip configuration interaction: An electronic structure model that is both variational and size-consistent. *Chem. Phys. Lett.*, 350:522–530, 2001.

[136] A.I. Krylov and C.D. Sherrill. Perturbative corrections to the equation-of-motion spin-flip SCF model: Application to bond-breaking and equilibrium properties of diradicals. *J. Chem. Phys.*, 116:3194–3203, 2002.

[137] A.I. Krylov, C.D. Sherrill, E.F.C. Byrd, and M. Head-Gordon. Size-consistent wavefunctions for non-dynamical correlation energy: The valence active space optimized orbital coupled-cluster doubles model. *J. Chem. Phys.*, 109(24):10669–10678, 1998.

[138] A.I. Krylov, C.D. Sherrill, and M. Head-Gordon. Efficient C++ tensor library for coupled-cluster calculations. unpublished.

[139] A.I. Krylov, C.D. Sherrill, and M. Head-Gordon. Excited states theory for optimized orbitals and valence optimized orbitals coupled-cluster doubles models. *J. Chem. Phys.*, 113:6509–6527, 2000.

[140] S.A. Kucharski, M. Włoch, M. Musiał, and R.J. Bartlett. Coupled-cluster theory for excited electronic states: The full equation-of-motion coupled-cluster single, double, and triple excitation method. *J. Chem. Phys.*, 115:8263–8266, 2001.

[141] L.D. Landau and E.M. Lifshitz. *Quantum Mechanics: Non-relativistic theory*. Pergamon, Oxford, 1977.

[142] H. Larsen, K. Hald, J. Olsen, and P. Jørgensen. Triplet excitation energies in full configuration interaction and coupled-cluster theory. *J. Chem. Phys.*, 115:3015–3020, 2001.

[143] R.J. Le Roy. LEVEL 7.1: A Computer Program for Solving the Radial Schro dinger Equation for Bound and Quasibound Levels. University of Waterloo Chemical Physics Research Report CP-642R (2000). The source

code and manual for this program may be obtained from the www site *http://theochem.uwaterloo.ca/~leroy*.

[144] S.V. Levchenko, A.V. Demyanenko, V. Dribinski, A.B. Potter, and and A.I. Krylov H. Reisler. Rydberg-valence interactions in $CH_2Cl \rightarrow CH_2$ + Cl photodissociation: Dependence of absorption probability on ground state vibrational excitation. *J. Chem. Phys.*, 118:9233–9240, 2003.

[145] S.V. Levchenko and A.I. Krylov. Electronic structure of halogen-substituted methyl radicals: Excited states of CH_2Cl and CH_2F. *J. Chem. Phys.*, 115(16):7485–7494, 2001.

[146] S.V. Levchenko and A.I. Krylov. Electronic structure of halogen-substituted methyl radicals: Vibrational spectra of CH_2Cl and CH_2F. *J. Phys. Chem. A*, 106(20):5169–5176, 2002.

[147] S.V. Levchenko and A.I. Krylov. Equation-of-motion spin-flip coupled-cluster model with single and double substitutions: Theory and application to cyclobutadiene. *J. Chem. Phys.*, 120(1):175–185, 2004.

[148] Y. Li and J.S. Francisco. CASSCF and MRCI studies of the electronic excited states of CH_2Cl and CH_2Br. *J. Chem. Phys.*, 114:2879, 2001.

[149] Z. Li and J.S. Francisco. High level ab initio molecular orbital study of the structures and vibrational spectra of CH_2Br and CH_2Br^+. *J. Chem. Phys.*, 110(2):817–822, 1999.

[150] S.G. Lias, J.E. Bartmess, J.F. Liebman, J.L. Holmes, R.D. Levin, and W.G. Mallard. Gas-phase ion and neutral thermochemistry. *J. Phys. Chem. Ref. Data*, 17, 1988.

[151] Y. Lin and A. Krantz. Matrix preparation of cyclobutadiene. *JCS Chem. Comm.*, (19):1111–1112, 1972.

[152] J. Linderberg and Y. Öhrn. *Propagators in quantum chemistry*. Academic, London, 1973.

[153] G.R. Long and J.W. Hudgens. Resonance-enhanced multiphoton ionization spectroscopy of $CHCl_2$ and $CDCl_2$. *J. Phys. Chem.*, 91:5870–5872, 1987.

[154] P.-O. Löwdin. On operators, superoperators, Hamiltonians and Liouvillians. *Int. J. Quant. Chem. Symp.*, 16:485–560, 1982.

[155] P.-O. Löwdin. Some aspects on the Hamiltonian and Liouvillian formalism, the special propagator methods, and the equation of motion approach. *Adv. Quantum Chem.*, 17:285–334, 1985.

[156] C.H. Martin, R.L. Graham, and K.F. Freed. *Ab initio* study of cyclobutadiene using the effective valence shell Hamiltonian method. *J. Chem. Phys.*, 99:7833–7844, 1993.

[157] S. Masamune, M. Suda, H. Ona, and L.M. Leichter. Cyclobutadiene. *J. Chem. Soc., Chem. Commun.*, pages 1268–1269, 1972.

[158] S. Masamune, Y. Sugihara, K. Morio, and J.E. Bertie. [4]annulene. Comments on its infrared spectrum. *Can. J. Chem.*, 54:2679–2680, 1976.

[159] P.E. Maslen, N.C. Handy, R.D. Amos, and P. Jayatilaka. Higher analytic derivatives. 4. Anharmonic effects in the benzene spectrum. *J. Chem. Phys.*, 97:4233–4254, 1992.

[160] D. Maurice and M. Head-Gordon. On the nature of electronic transitions in radicals: An extended single excitation configuration interaction method. *J. Phys. Chem.*, 100(15):6131–6137, 1996.

[161] C.W. McCurdy, T.N. Rescigno, D.L. Yeager, and V. McKoy. *Modern Theoretical Chemistry*, volume 3, chapter The equations of motion method: An approach to dynamical properties of atoms and molecules, pages 339–386. Plenum Press, New York, 1977.

[162] A.D. McLean and G.S. Chandler. Contracted Gaussian basis sets for molecular calculations. I. Second row atoms, Z=11-18. *J. Chem. Phys.*, 72:5639, 1980.

[163] A.D. McLean, B.H. Lengsfield, J. Pacansky, and Y. Ellinger. Symmetry breaking in molecular calculations and the reliable prediction of equilibrium geometries. The formyloxyl radical as an example. *J. Chem. Phys.*, 83:3567–3576, 1985.

[164] R. McWeeny. *Methods of Molecular Quantum Mechanics*. Academic Press, 2nd edition, 1992.

[165] A.M. Mebel and S.-H. Lin. Excited electronic states of the methyl radical. Ab initio molecular orbital study of geometries, excitation energies and vibronic spectra. *Chem. Phys.*, 215:329, 1997.

[166] Ch. Meier and V. Engel. Electron kinetic energy distributions from multiphoton ionization of Na_2 with femtosecond laser pulses. *Chem. Phys. Lett.*, 212:691–696, 1993.

[167] Ch. Meier and V. Engel. Mapping of wave-packet dynamics in a double-well potential via femtosecond pump/probe photoelectron spectroscopy. *J. Chem. Phys.*, 101:2673–2677, 1994.

[168] F. Mertins and J. Schirmer. Algebraic propagator approaches and intermediate-state representations. I. The biorthogonal and unitary coupled-cluster methods. *Phys. Rev. A*, 53:2140–2152, 1996.

[169] F. Mertins, J. Schirmer, and A. Taranteli. Algebraic propagator approaches and intermediate-state representations. I. The equation-of-motion methods for N, N+/-1, and N+/-2 electrons. *Phys. Rev. A*, 53:2153–2168, 1996.

[170] J.P. Michaut and J. Roncin. ESR study of the CH_2Cl radical in a single crystal of CH_3Cl. *Chem. Phys. Lett.*, 12(1):95–97, 1971.

[171] K. Mikhaylichenko, C. Riehn, L. Valachovic, A. Sanov, and C. Wittig. Unimolecular decomposition of NO_3: The $NO+O_2$ threshold regime. *J. Chem. Phys.*, 105:6807–6817, 1996.

[172] D.E. Milligan and M.E. Jacox. Infrared and ultraviolet spectroscopic study of the products of the vacuum-ultraviolet photolysis of methane in Ar and N_2 matrices. The infrared spectrum of the free radical CH_3. *J. Chem. Phys.*, 47:5146–5156, 1967.

[173] Y. Mo, W. Wu, and Q. Zhang. Theoretical resonance energies of benzene, cyclobutadiene, and butadiene. *J. Phys. Chem.*, 98:10048–10053, 1994.

[174] T. Momose, M. Miki, M. Uchida, T. Shimizu, I. Yoshizawa, and T. Shida. Infrared spectroscopic studies on photolysis of methyl iodide and its clusters in solid parahydrogen. *J. Chem. Phys.*, 103:1400–1405, 1995.

[175] H.J. Monkhorst. Calculation of properties with the coupled-cluster method. *Int. J. Quant. Chem. Symp.*, 11:421–432, 1977.

[176] K Morokuma, L. Pedersen, and M. Karplus. Structure of CH_3 and CF_3. *J. Chem. Phys.*, 48:4801–4802, 1968.

[177] J.A. Mucha, D.A. Jennings, K.M. Evenson, and J.T. Hougen. Far-infrared laser magnetic resonance spectrum of CH_2F. *J. Molec. Spect.*, 68:122–124, 1977.

[178] D. Mukherjee and P.K. Mukherjee. A response-function approach to the direct calculation of the transition-energy in a multiple-cluster expansion formalism. *Chem. Phys.*, 39:325–335, 1979.

[179] R.S. Mulliken. Charge-transfer spectra. *J. Chem. Phys.*, 7:20, 1939.

[180] K. Nakamura, Y. Osamura, and S. Iwata. Second-order Jahn-Teller effect of cyclobutadiene in low-lying states. An MCSCF study. *Chem. Phys.*, 136:67–77, 1989.

[181] O.J. Nielsen, J. Munk, G. Locke, and T.J. Wallington. Ultraviolet absorption spectra and kinetics of the self-reaction of bromomethyl and peroxybromomethyl radicals in the gas phase at 298 K. *J. Phys. Chem.*, 95:8714–8719, 1991.

[182] M. Nooijen and R.J. Bartlett. Equation of motion coupled cluster method for electron attachment. *J. Chem. Phys.*, 102:3629–3647, 1995.

[183] M. Nooijen and R.J. Bartlett. Similarity transformed equation-of-motion coupled-cluster theory: Details, examples, and comparisons. *J. Chem. Phys.*, 107:6812–6830, 1997.

[184] J.V. Ortiz. Toward an exact one-electron picture of chemical bonding. *Adv. Quantum Chem.*, 35:33–52, 1999.

[185] J. Pacansky and J. Bargon. Low temperature photochemical studies on acetyl benzoyl peroxide. the observation of methyl and phenyl radicals by matrix isolation infrared spectroscopy. *J. Am. Chem. Soc.*, 97:6896–6897, 1975.

[186] R.G. Parr and W. Yang. *Density functional theory of atoms and molecules*, volume 16 of *International Series of Monographs on Chemistry*. Oxford, New-York, 1989.

[187] B.J. Persson, P.R. Taylor, and J.M.L. Martin. Ab initio calibration study of the heat of formation, geometry, and anharmonic force field of fluoroacetylene. *J. Phys. Chem. A*, 102:2483–2492, 1998.

[188] P. Piecuch and R.J. Bartlett. EOMXCC: A new coupled-cluster method for electronic excited states. *Adv. Quantum Chem.*, 34:295–380, 1999.

[189] J. A. Pople. Electron interaction in unsaturated hydrocarbons. *Trans. Faraday Soc.*, 49:1375–1385, 1953.

[190] A.B. Potter, V. Dribinski, A.V. Demyanenko, and H. Reisler. Competitive channels in the jet-cooled photodissociation of the CH_2Cl radical. *Chem. Phys. Lett.*, 349:257–265, 2001.

[191] P. Pulay. *Ab initio* calculation of force constants and equilibrium geometries in polyatomic molecules. I. Theory. *Mol. Phys.*, 17:197–204, 1969.

[192] G.D. Purvis and R.J. Bartlett. A full coupled-cluster singles and doubles model: The inclusion of disconnected triples. *J. Chem. Phys.*, 76:1910, 1982.

[193] K. Raghavachari, G.W. Trucks, J.A. Pople, and M. Head-Gordon. A fifth-order perturbation comparison of electron correlation theories. *Chem. Phys. Lett.*, 157:479–483, 1989.

[194] J.I. Raymond and L. Andrews. Matrix reactions of fluorohalomethanes with alkali metals: infrared spectrum and bonding in the monofluoromethyl radical. *J. Phys. Chem.*, 75:3235–3242, 1971.

[195] R.L. Redington. State-specific vibrational anharmonicities in cyclobutadiene and evidence for fast automerization by $^{12}C_4H_4$. *J. Chem. Phys.*, 109:10781–10794, 1998.

[196] A.E. Reed, L.A. Curtiss, and F. Weinhold. Intermolecular interactions from natural bond orbital, donor-aceptor viewpoint. *Chem. Rev.*, 88:899–926, 1988.

[197] S. Rettrup. An iterative method for calculating several of the extreme eigensolutions of large real non-symmetric matrices. *J. Comput. Phys.*, 45:100–107, 1982.

[198] R.J. Rico and M. Head-Gordon. Single-reference theories of molecular excited states with single and double substitutions. *Chem. Phys. Lett.*, 213:224–232, 1993.

[199] J.M. Riveros. Anharmonicity of the out-of-plane vibration of the methyl radical. *J. Chem. Phys.*, 51:1269–1270, 1969.

[200] P.B. Roussel, P.D. Lightfoot, F. Caraip, V. Catoire, R. Lesclaux, and W. Forst. Ultraviolet absorption spectra of the CH_2Cl and $CHCl_2$ radicals and the kinetics of their self-recombination reactions from 273 to 686 K. *J. Chem. Soc., Faraday Trans.*, 87:2367–2377, 1991.

[201] D.J. Rowe. Equations-of-motion method and the extended shell model. *Rev. Mod. Phys.*, 40:153–166, 1968.

[202] L. Salem. Theory of photochemical reactions. *Science*, 191:822–830, 1976.

[203] L. Salem and C. Rowland. The electronic properties of diradicals. *Angew. Chem. Int. Ed. Engl.*, 11(2):92–111, 1972.

[204] J.C. Sancho-Garcia and F. Moscardo. Usefulness of the Colle-Salvetti model for the treatment of the nondynamic correlation. *J. Chem. Phys.*, 118:1054–1058, 2003.

[205] J.C. Sancho-Garcia, A.J. Perez-Jimenez, and F. Moscardo. A comparison between DFT and other *ab initio* schemes on the activation energy in the automerization of cyclobutadiene. *Chem. Phys. Lett.*, 317:245–251, 2000.

[206] J.C. Sancho-Garcia, J. Pittner, and P. Carsky. Multireference coupled-cluster calculations on the energy of activation in the automerization of cyclobutadiene: Assessment of the state-specific multireference Brillouin-Wigner theory. *J. Chem. Phys.*, 112:8785–8788, 2000.

[207] L.J. Schaad, B.A. Hess Jr., and C.S. Ewig. Calculated infrared and Raman spectra of the ^1A_g ground states of rectangular cyclobutadiene and tetradeuteriocyclobutadiene. *J. Am. Chem. Soc.*, 101:2281–2283, 1979.

[208] R. Schinke. *Photodissociation Dynamics*. Cambridge Monographs on Atomic, Molecular, and Chemical Physics. Cambridge University Press, 1993.

[209] D.M. Schrader and M. Karplus. Orbital following in the methyl radical. *J. Chem. Phys.*, 40:1593–1601, 1964.

[210] J.S. Sears, C.D. Sherrill, and A.I. Krylov. A spin-complete version of the spin-flip approach to bond breaking: What is the impact of obtaining spin eigenfunctions? *J. Chem. Phys.*, 118:9084–9094, 2003.

[211] T.J. Sears, F. Temps, H.Gg. Wagner, and M. Wolf. Far-infrared laser magnetic resonance spectroscopy of CH_2Cl ($\tilde{X}^2B_1$). *J. Molec. Spect.*, 168:136–146, 1994.

[212] J.A. Seetula. Kinetics and thermochemistry of the R + HBr $\leftrightarrow$ RH + Br (R = CH_2Cl, $CHCl_2$, CH_3CHCl or CH_3CCl_2) equilibrium. *J. Chem. Soc., Faraday Trans.*, 92:3069–3079, 1996.

[213] J.A. Seetula. *Ab initio* study of the transition states for determining the enthalpies of formation of alkyl and halogenated alkyl free radicals. *Phys. Chem. Chem. Phys.*, 2:3807–3812, 2000.

[214] H. Sekino and R.J. Bartlett. A linear response, coupled-cluster theory for excitation energy. *Int. J. Quant. Chem. Symp.*, 18:255–265, 1984.

[215] S.S. Shaik, P.C. Hiberty, J.-M. Lefour, and G. Ohanessian. Is delocalization a driving force in chemistry? Benzene, allyl radical, cyclobutadiene and their isoelectronic species. *J. Am. Chem. Soc.*, 109:363–374, 1987.

[216] Y. Shao, M. Head-Gordon, and A.I. Krylov. The spin-flip approach within time-dependent density functional theory: Theory and applications to diradicals. *J. Chem. Phys.*, 118:4807–4818, 2003.

[217] C.D. Sherrill, A.I. Krylov, E.F.C. Byrd, and M. Head-Gordon. Energies and analytic gradients for a coupled-cluster doubles model using variational Brueckner orbitals: Application to symmetry breaking in O_4^+. *J. Chem. Phys.*, 109:4171, 1998.

[218] D. Sinha, D. Mukhopadhya, R. Chaudhuri, and D. Mukherjee. The eigenvalue-independent partitioning technique in Fock space: An alternative route to open-shell coupled-cluster theory for incomplete model spaces. *Chem. Phys. Lett.*, 154:544–549, 1989.

[219] M.O. Sinnokrot and C.D. Sherrill. Density functional theory predictions of anharmonicity and spectroscopic constants for diatomic molecules. *J. Chem. Phys.*, 115:2439–2448, 2001.

[220] S. Skokov, K.A. Peterson, and J.M. Bowman. Accurate variational calculations and analysis of the HOCl vibrational energy spectrum. *J. Chem. Phys.*, 109:2662–2671, 1998.

[221] L.V. Slipchenko and A.I. Krylov. Singlet-triplet gaps in diradicals by the spin-flip approach: A benchmark study. *J. Chem. Phys.*, 117:4694–4708, 2002.

[222] L.V. Slipchenko and A.I. Krylov. Electronic structure of the 1,3,5,-tridehydrobenzene triradical in its ground and excited states. *J. Chem. Phys.*, 118:9614–9622, 2003.

[223] L.V. Slipchenko and A.I. Krylov. Electronic structure of the trimethylenemethane diradical in its ground and electronically excited states: Bonding, equilibrium structures and vibrational frequencies. *J. Chem. Phys.*, 118:6874–6883, 2003.

[224] L.V. Slipchenko and A.I. Krylov. Spin-conserving and spin-flipping equation-of-motion coupled-cluster method with triple excitations. *J. Chem. Phys.*, 2005. in press.

[225] D.W. Smith and L. Andrews. Matrix infrared spectrum and bonding in monoiodomethyl radical. *J. Chem. Phys.*, 58(12):5222–5229, 1970.

[226] D.W. Smith and L. Andrews. Matrix infrared spectrum and bonding in the monobromomethyl radical. *J. Chem. Phys.*, 55(11):5295–5303, 1971.

[227] A. Snelson. Infrared matrix isolation spectrum of the methyl radical produced by pyrolysis of methyl iodine and dimethyl mercury. *J. Phys. Chem.*, 74:537–544, 1970.

[228] L.C. Snyder. A simple molecular orbital study of aromatic molecules and ions having orbitally degenerate ground states. *J. Phys. Chem.*, 66:2299–2306, 1962.

[229] J.F. Stanton. Many-body methods for excited state potential energy surfaces. I. General theory of energy gradients for the equation-of-motion coupled-cluster method. *J. Chem. Phys.*, 99(11):8840–8847, 1993.

[230] J.F. Stanton and R.J. Bartlett. The equation of motion coupled-cluster method. A systematic biorthogonal approach to molecular excitation energies, transition probabilities, and excited state properties. *J. Chem. Phys.*, 98:7029–7039, 1993.

[231] J.F. Stanton and J. Gauss. Analytic energy derivatives for ionized states described by the equation-of-motion coupled cluster method. *J. Chem. Phys.*, 101(10):8938–8944, 1994.

[232] J.F. Stanton and J. Gauss. Analytic energy derivatives for the equation-of-motion coupled-cluster method — algebraic expressions, implementation and application to the S_1 state of HFCO. *Theor. Chim. Acta*, 91:267–289, 1995.

[233] J.F. Stanton and J. Gauss. Many-body methods for excited state potential energy surfaces. II. Analytic second derivatives for excited state energies in the equation-of-motion coupled-cluster method. *J. Chem. Phys.*, 103(20):88931–8943, 1995.

[234] J.F. Stanton, J. Gauss, and R.J. Bartlett. On the choice of orbitals for symmetry breaking problems with application to NO_3. *J. Chem. Phys.*, 97:5554–5559, 1992.

[235] J.F. Stanton, J. Gauss, J.D. Watts, W.J. Lauderdale, and R.J. Bartlett. ACES II, 1993. The package also contains modified versions of the MOLECULE Gaussian integral program of J. Almlöf and P.R. Taylor, the ABACUS integral derivative program written by T.U. Helgaker, H.J.Aa. Jensen, P. Jørgensen and P.R. Taylor, and the PROPS property evaluation integral code of P.R. Taylor.

[236] J.F. Stanton, C.L. Lopreore, and J. Gauss. The equilibrium structure and fundamental vibrational frequencies of dioxirane. *J. Chem. Phys.*, 108:7190–7196, 1998.

[237] P.J. Stephens, F.J. Devlin, C.F. Chabalowski, and M.J. Frisch. *Ab Initio* calculation of vibrational absorption and circular dichroism spectra using density functional force fields. *J. Phys. Chem.*, 98:11623–11627, 1994.

[238] A. Szabo and N.S. Ostlund. *Modern Quantum Chemistry: Introduction to Advanced Electronic Structure Theory*. McGraw-Hill, New York, 1989.

[239] P.G. Szalay. Analytic energy derivatives for coupled-cluster methods describing excited states: General formulas and comparison of computational costs. *Int. J. Quant. Chem.*, 55:151–163, 1995.

[240] Z. Szekeres, Á. Szabados, M. Kállay, and P.R. Surján. On the ”killer condition” in the equation-of-motion method: Ionization potentials from multireference wave functions. *Phys. Chem. Chem. Phys.*, 3:696–701, 2001.

[241] S. Tam, M. Macler, and M.E. Fajardo. Matrix isolation spectroscopy of laser ablated carbon species in Ne, D_2, and H_2 matrices. *J. Chem. Phys.*, 106:8955–8963, 1997.

[242] I. Tamm. *J. Phys. USSR*, 9:449, 1945.

[243] L.Y. Tan, A.M. Winer, and G.C. Pimentel. Infrared spectrum of gaseous methyl radical by rapid scan spectroscopy. *J. Chem. Phys.*, 57:4028–4037, 1972.

[244] I. Tanarro, M.M. Sanz, D. Bermejo, C. Domingo, and J. Santos. Double modulation-high resolution infrared spectroscopic technique: The ν_3 band of the CH_3 radical and excited states of CH_4 in a hollow cathode discharge. *J. Chem. Phys.*, 100:238–246, 1994.

[245] M. Tobita, S.A. Perera, M. Musial, R.J. Bartlett, M. Nooijen, and J.S. Lee. Critical comparison of single-reference and multireference coupled-cluster methods: Geometry, harmonic frequencies, and excitation energies of N_2O_2. *J. Chem. Phys.*, 119:10713–10723, 2003.

[246] N.E. Triggs, M. Zahedi, and J.W. Nibler. High resolution study of the ν_1 vibration of CH_3 by coherent Raman photofragment spectroscopy. *J. Chem. Phys.*, 96:1822–1831, 1992.

[247] B.P. Tsai, R.D. Johnson III, and J.W. Hudgens. Electronic spectra of CF_2Cl and $CFCl_2$ radicals observed by resonance-enhanced multiphoton ionization. *J. Phys. Chem.*, 93:5334–5336, 1989.

[248] E. Tschuikow-Roux and S. Paddison. Bond dissociation energies and radical heats of formation in CH_3Cl, CH_2Cl_2, CH_3Br, CH_2Br_2, CH_2FCl, and $CHFCl_2$. *Int. J. Chem. Kinet.*, 19:15–24, 1987.

[249] J. Verges, C. Effantin, J. d'Incan, D.L. Cooper, and R.F. Barrow. Double-minimum $(2)^1\sigma_u^+$ state of Na_2. *Phys. Rev. Lett.*, 53:46–47, 1984.

[250] E. Villenave and R. Lesclaux. The UV absorption spectra of CH_2Br and CH_2BrO_2 with itself and with HO_2 at 298 K. *Chem. Phys. Lett.*, 236:376–384, 1995.

[251] A.F. Voter and W.A. Goddard III. The generalized resonating valence bond description of cyclobutadiene. *J. Am. Chem. Soc.*, 108:2830–2837, 1986.

[252] M. Weissman and S.W. Benson. Heat of formation of the $CHCl_2$ radical. bond dissociation energies in chloromethanes and chloroethanes. *J. Phys. Chem.*, 87:243–244, 1983.

[253] M. Wladyslawski and M. Nooijen. The photoelectron spectrum of the NO_3 radical revisited: A theoretical investigation of potential energy surfaces and conical intersections. In *ACS Symposium Series*, volume 828, pages 65–92, 2002.

[254] Y. Xie, W.D. Allen, Y. Yamaguchi, and H.F. Schaefer III. Is the oxywater radical cation more stable than neutral oxywater. *J. Chem. Phys.*, 104:7615–7623, 1996.

[255] C. Yamada and E. Hirota. Infrared diode laser spectroscopy of the ν_3 band of the fluoromethyl radical, CH_2F. *J. Molec. Spect.*, 116:101–107, 1986.

[256] C. Yamada, E. Hirota, and K. Kawaguchi. Diode laser study of the ν_2 band of the methyl radical. *J. Chem. Phys.*, 75:5256–5264, 1981.

[257] M. Zahedi, J.A. Harrison, and J.W. Nibler. 266 nm CH_3I photodissociation: CH_3 spectra and population distributions by coherent Raman spectroscopy. *J. Chem. Phys.*, 100:4043–4055, 1994.

Appendix I

We solve Eqns. (I.34)-(I.35) by using a generalized Davidson's iterative diagonalization procedure [54, 103, 197], which requires calculation of products of the transformed Hamiltonian matrix with trial vectors:

$$\sigma_i^a = ([\bar{H}_{SS} - E_{CC}]R_1)_i^a + (\bar{H}_{SD}R_2)_i^a \tag{AI.1}$$

$$\sigma_{ij}^{ab} = (\bar{H}_{DS}R_1)_{ij}^{ab} + ([\bar{H}_{DD} - E_{CC}]R_2)_{ij}^{ab}$$

$$\tilde{\sigma}_i^a = (\bar{L}_1[H_{SS} - E_{CC}])_i^a + (L_2\bar{H}_{DS})_i^a \tag{AI.2}$$

$$\tilde{\sigma}_{ij}^{ab} = (L_1\bar{H}_{SD})_{ij}^{ab} + (L_2[\bar{H}_{DD} - E_{CC}])_{ij}^{ab}$$

Programmable expressions for right σ and left $\tilde{\sigma}$ are:

$$([\bar{H}_{SS} - E_{CC}]R_1)_i^a =< \Phi_i^a|\bar{H} - E_{CC}|R_1\Phi_0 >=$$

$$= \sum_b r_i^b F_{ab} - \sum_j r_j^a F_{ij} - \sum_{jb} r_j^b I_{ibja}^1 \tag{AI.3}$$

$$(\bar{H}_{SD}R_2)_i^a =< \Phi_i^a|\bar{H}|R_2\Phi_0 >=$$

$$= \sum_{jb} r_{ij}^{ab} F_{jb} - \frac{1}{2}\left(\sum_{jkb} r_{jk}^{ab} I_{ibjk}^6 + \sum_{jbc} r_{ij}^{bc} I_{jabc}^7\right) \quad \text{(AI.4)}$$

$$(\bar{H}_{DS}R_1)_{ij}^{ab} =< \Phi_{ij}^{ab}|\bar{H}|R_1\Phi_0 >=$$

$$= \sum_k (r_k^a I_{ijkb}^2 - r_k^b I_{ijka}^2) + \sum_c (r_i^c I_{jcab}^3 - r_j^c I_{icab}^3)$$
$$+ \sum_l (T_{il}^1 t_{jl}^{ab} - T_{jl}^1 t_{il}^{ab}) + \sum_d (T_{ad}^2 t_{ij}^{bd} - T_{bd}^2 t_{ij}^{ad}) \quad \text{(AI.5)}$$

$$([\bar{H}_{DD} - E_{CC}]R_2)_{ij}^{ab} =< \Phi_{ij}^{ab}|\bar{H} - E_{CC}|R_2\Phi_0 >=$$

$$= \sum_k \left(r_{jk}^{ab} F_{ik} - r_{ik}^{ab} F_{jk}\right) + \sum_c \left(r_{ij}^{ac} F_{bc} - r_{ij}^{bc} F_{ac}\right)$$
$$+ \sum_{kc} \left(r_{jk}^{ac} I_{ickb}^1 - r_{ik}^{ac} I_{jckb}^1 + r_{ik}^{bc} I_{jcka}^1 - r_{jk}^{bc} I_{icka}^1\right) + \sum_{kl} r_{kl}^{ab} I_{ijkl}^4$$
$$+ \sum_{cd} r_{ij}^{cd} I_{abcd}^5 + \sum_l (T_{il}^3 t_{jl}^{ab} - T_{jl}^3 t_{il}^{ab}) + \sum_d (T_{ad}^4 t_{ij}^{bd} - T_{bd}^4 t_{ij}^{ad}) \quad \text{(AI.6)}$$

$$(L_1[\bar{H}_{SS} - E_{CC}])_i^a =< \Phi_0 L_1|\bar{H} - E_{CC}|\Phi_i^a >=$$

$$= \sum_b l_i^b F_{ba} - \sum_j l_j^a F_{ji} - \sum_{jb} l_j^b I_{jaib}^1 \quad \text{(AI.7)}$$

$$(L_2\bar{H}_{DS})_i^a =< \Phi_0 L_2|\bar{H}|\Phi_i^a >= \frac{1}{2}\sum_{jkb} l_{jk}^{ab} I_{jkib}^2 + \frac{1}{2}\sum_{jbc} l_{ij}^{bc} I_{jabc}^3$$
$$+ \sum_{lk} T_{lk}^5 I_{ikla}^6 + \sum_{dc} T_{dc}^6 I_{idac}^7 \quad \text{(AI.8)}$$

$$(L_1\bar{H}_{SD})_{ij}^{ab} =< \Phi_0 L_1|\bar{H}|\Phi_{ij}^{ab} >= l_i^a F_{jb} - l_j^a F_{ib} + l_j^b F_{ia} - l_i^b F_{ja}$$

$$+ \sum_k (l_k^b I_{ijka}^6 - l_k^a I_{ijkb}^6) + \sum_c (l_j^c I_{icab}^7 - l_i^c I_{jcab}^7) \quad \text{(AI.9)}$$

$$(L_2[\bar{H}_{DD} - E_{CC}])_{ij}^{ab} =< \Phi_0 L_2|\bar{H} - E_{CC}|\Phi_{ij}^{ab} >= \sum_k (l_{jk}^{ab} F_{ki} - l_{ik}^{ab} F_{kj})$$
$$+ \sum_c (l_{ij}^{ac} F_{cb} - l_{ij}^{bc} F_{ca}) + \sum_{kl} l_{kl}^{ab} I_{klij}^4 + \sum_{cd} l_{ij}^{cd} I_{cdab}^5$$
$$+ \sum_{kc} \left(-l_{ik}^{ac} I_{kbjc}^1 + l_{jk}^{ac} I_{kbic}^1 + l_{ik}^{bc} I_{kajc}^1 - l_{jk}^{bc} I_{kaic}^1\right)$$
$$+ \sum_l \left(T_{il}^5 < jl||ab > - T_{jl}^5 < il||ab >\right)$$
$$+ \sum_d \left(T_{ad}^6 < ij||bd > - T_{bd}^6 < ij||ad >\right) \quad \text{(AI.10)}$$

Intermediates used in Eqns. (AI.3-AI.10) are given in Table AI.1.

Table AI.1: Intermediates used in Eqns. (AI.3-AI.10). To avoid storage of large 6-index quantities, intermediates which have to be updated at each iteration of diagonalization procedure were introduced.

$$F_{ia} = f_{ia} + \sum_{jb} t_j^b < ij||ab >$$
$$F_{ij} = f_{ij} + \sum_a t_i^a f_{ja} + \sum_{ka} t_k^a < jk||ia > + \sum_{kab} t_i^a t_k^b < jk||ab > + \tfrac{1}{2} \sum_{kbc} t_{ik}^{bc} < jk||bc >$$
$$F_{ab} = f_{ab} - \sum_i t_i^a f_{ib} - \sum_{ic} t_i^c < ia||bc > + \sum_{ijc} t_i^c t_j^a < ij||bc > - \tfrac{1}{2} \sum_{jkc} t_{jk}^{ac} < jk||bc >$$
$$I^1_{iajb} = < ia||jb > - \sum_k t_k^b < jk||ia > - \sum_c t_i^c < jb||ac > + \sum_{kc} t_i^c t_k^b < jk||ac > - \sum_{kc} t_{ik}^{bc} < jk||ac >$$
$$I^2_{ijka} = - < ij||ka > + 2 \sum_l t_l^a I^4_{ijkl} + \sum_b \left(t_i^b (< jb||ka > - \sum_{lc} t_{jl}^{ac} < kl||bc >) - t_j^b (< ib||ka > - \sum_{lc} t_{il}^{ac} < kl||bc >) \right) - \sum_{bc} t_i^b t_j^c < ka||bc > - \sum_{lbc} t_l^b t_{ij}^{ac} < kl||bc > + \sum_c t_{ij}^{bc} f_{kc} - \tfrac{1}{2} \sum_{cd} t_{ij}^{cd} < kb||cd > + \sum_{lc} (t_{il}^{bc} < jc||kl > - t_{jl}^{bc} < ic||kl >)$$
$$I^3_{icab} = - < ic||ab > + 2 \sum_d t_i^d I^5_{bcad} + \sum_j \left(t_j^b (< ia||jc > - \sum_{kd} t_{ik}^{cd} < jk||ad >) - t_j^c (< ia||jb > - \sum_{kd} t_{ik}^{bd} < jk||ad >) \right) - \sum_{jk} t_j^b t_k^c < jk||ia > - \sum_{jkd} t_j^d t_{ik}^{bc} < jk||ad > + \sum_k t_{ik}^{ab} f_{kc} - \tfrac{1}{2} \sum_{kl} t_{kl}^{ab} < ic||kl > + \sum_{kd} (t_{ik}^{ad} < kb||cd > - t_{ik}^{bd} < ka||cd >)$$
$$I^4_{ijkl} = \tfrac{1}{2} < ij||kl > + \tfrac{1}{2} \sum_a (t_j^a < kl||ia > - t_i^a < kl||ja >) + \tfrac{1}{2} \sum_{ab} t_i^a t_j^b < kl||ab > + \tfrac{1}{4} \sum_{cd} t_{ij}^{cd} < kl||cd >$$
$$I^5_{abcd} = \tfrac{1}{2} < ab||cd > - \tfrac{1}{2} \sum_i (t_i^a < ib||cd > - t_i^b < ia||cd >) + \tfrac{1}{2} \sum_{ij} t_i^a t_j^b < ij||cd > + \tfrac{1}{4} \sum_{kl} t_{kl}^{ab} < kl||cd >$$
$$I^6_{ijka} = < ij||ka > - \sum_c t_k^c < ij||ac >$$
$$I^7_{iabc} = < ia||bc > - \sum_j t_j^a < ij||bc >$$

$$T^1_{ij} = \sum_{kc} r_k^c I^6_{jkic}$$
$$T^2_{ab} = \sum_{kc} r_k^c I^7_{kabc}$$
$$T^3_{ij} = \tfrac{1}{2} \sum_{kcd} r_{ik}^{cd} < jk||cd >$$
$$T^4_{ab} = \tfrac{1}{2} \sum_{klc} r_{kl}^{ac} < kl||bc >$$
$$T^5_{ij} = \tfrac{1}{2} \sum_{kab} l_{ik}^{ab} t_{jk}^{ab}$$
$$T^6_{ab} = \tfrac{1}{2} \sum_{ijc} l_{ij}^{ac} t_{ij}^{bc}$$

$$r_0 = \tfrac{1}{\omega} \left(\sum_{ia} r_i^a F_{ia} + \tfrac{1}{4} \sum_{ijab} r_{ij}^{ab} < ij||ab > \right)$$
$$r_0 = - \sum_{ia} r_i^a z_i^a - \tfrac{1}{4} \sum_{ijab} r_{ij}^{ab} z_{ij}^{ab}$$

$$A_{iaia} = F_{aa} - F_{ii} - I^1_{iaia}$$
$$D_{ijab,ijab} = -F_{ii} - F_{jj} + F_{aa} + F_{bb} - (I^1_{ibib} + I^1_{jbjb} + I^1_{iaia} + I^1_{jaja}) + I^4_{ijij} + I^5_{abab} - \tfrac{1}{2} \sum_l (< jl||ab > t_{jl}^{ab} + < il||ab > t_{il}^{ab}) - \tfrac{1}{2} \sum_d (< ij||bd > t_{ij}^{bd} + < ij||ad > t_{ij}^{ad})$$

Appendix II

AII.1 Variational properties of the EOM functional

To differentiate the EOM energy functional w.r.t. R and L, we start from Eq. (II.1):

$$E = \frac{< \Phi_0 L|\bar{H}|R\Phi_0 >}{< \Phi_0 L|R\Phi_0 >} = \frac{\sum_{\mu=1}^{2} L_\mu < \Phi_\mu|\bar{H}|R\Phi_0 >}{\sum_{\mu=1}^{2} L_\mu < \Phi_\mu|R\Phi_0 >} \qquad \text{(AII.1)}$$

By differentiation the energy w.r.t. the amplitudes L_μ and by using Eq. (II.1) we obtain:

$$\begin{aligned} \frac{\partial E}{\partial L_\mu} &= \frac{< \Phi_\mu|\bar{H}|R\Phi_0 >< \Phi_0 L|R\Phi_0 > - < \Phi_0 L|\bar{H}|R\Phi_0 >< \Phi_\mu|R\Phi_0 >}{< \Phi_0 L|R\Phi_0 >^2} = \\ &= \frac{< \Phi_0 L|\bar{H}|R\Phi_0 > -E < \Phi_\mu|R\Phi_0 >}{< \Phi_0 L|R\Phi_0 >} = \frac{< \Phi_\mu|\bar{H} - E|R\Phi_0 >}{< \Phi_0 L|R\Phi_0 >} \end{aligned} \qquad \text{(AII.2)}$$

which is zero because equations for R are satisfied, see Eq. (II.2). Likewise, $\frac{\partial E}{\partial R_\mu} = 0$ by virtue of Eq. (II.3).

AII.2 Derivation of orbital response equations

By combining Eq. (II.44) and Eq. (II.45), we arrive to the following:

$$\begin{aligned}\sum_{\mu} C_{\mu u}\frac{\partial \mathcal{L}}{\partial C_{\mu t}} &= \sum_{pq}\left(\sum_{\mu} C_{\mu u}\frac{\partial h_{pq}}{\partial C_{\mu t}}\right)\gamma_{pq} + \frac{1}{4}\sum_{pqrs}\left(\sum_{\mu} C_{\mu u}\frac{\partial < pq||rs >}{\partial C_{\mu t}}\right)\Gamma_{pqrs} \\ &+ \frac{1}{2}\sum_{pq}\lambda_{pq}\left(\sum_{\mu} C_{\mu u}\frac{\partial f_{pq}}{\partial C_{\mu t}}\right) + \sum_{pq}\omega_{pq}\left(\sum_{\mu} C_{\mu u}\frac{\partial S_{pq}}{\partial C_{\mu t}}\right) \qquad \text{(AII.3)}\end{aligned}$$

Thus, the evaluation of the derivative requires differentiation of the Hamiltonian and overlap matrix elements w.r.t. C, followed by contraction with C. The one-particle integral term is [217]:

$$\sum_{\mu} C_{\mu u}\frac{\partial h_{pq}}{\partial C_{\mu t}} = \sum_{\mu} C_{\mu u}\frac{\partial(\sum_{\nu\lambda} C_{\nu p}h_{\nu\lambda}C_{\lambda q})}{\partial C_{\mu t}} =$$

$$\sum_{\mu} C_{\mu u}\left(\delta_{pt}\sum_{\lambda} C_{\lambda q}h_{\mu\lambda} + \delta_{qt}\sum_{\nu} C_{\nu p}h_{\nu\mu}\right) = \delta_{pt}h_{uq} + \delta_{qt}h_{pu} \qquad \text{(AII.4)}$$

Similarly, the two-electron part yields:

$$\begin{aligned}\sum_{\mu} C_{\mu u}\frac{\partial < pq||rs >}{\partial C_{\mu t}} &= \delta_{pt} < uq||rs > + \delta_{qt} < pu||rs > \\ &+ \delta_{rt} < pq||us > + \delta_{st} < pq||ru > \qquad \text{(AII.5)}\end{aligned}$$

The Fock matrix derivatives are:

$$\sum_{\mu} C_{\mu u} \frac{\partial f_{pq}}{\partial C_{\mu i}} = \delta_{ip} f_{uq} + \delta_{iq} f_{pu} + < pu||qi > + < pi||qu > \tag{AII.6}$$

$$\sum_{\mu} C_{\mu u} \frac{\partial f_{pq}}{\partial C_{\mu a}} = \delta_{ap} f_{uq} + \delta_{aq} f_{pu} \tag{AII.7}$$

And, finally, the overlap term is:

$$\sum_{\mu} C_{\mu u} \frac{\partial S_{pq}}{\partial C_{\mu t}} = \delta_{pt} S_{uq} + \delta_{qt} S_{pu} \tag{AII.8}$$

Appendix III

Below we prove that the adiabatic and diabatic effective OPLA potentials (IV.15) have identical harmonic parts. As a result, the approximate account of the interaction between modes by the adiabatic model affects only quartic and higher terms of the effective OPLA potential, leaving the harmonic part unchanged.

The proof is based on the following: (i) the OPLA normal mode does not belong to the fully symmetric irreducible representation (irrep), e.g., it is b_1 in C_{2v} or a_2'' in D_{3h}; and (ii) the OPLA vibration is the only mode in this irrep. The above result is valid for any mode which satisfies (i) and (ii). However, for the sake of clarity the discussion below is focused on the specific case of the OPLA mode.

With (i) and (ii) satisfied for the OPLA mode, the global potential energy surface is symmetric w.r.t. positive and negative displacements along the OPLA coordinate:

$$V(\theta, Q_2, \ldots, Q_N) = V(-\theta, Q_2, \ldots, Q_N), \qquad \text{(AIII.1)}$$

where θ denotes the normal coordinate for the OPLA motion. The potential along any fully symmetric coordinate is necessarily asymmetric (consider for example the

symmetric CH stretch). Moreover, Eq. (AIII.1) would not hold if θ were not the only mode in its irrep, because the displacements along other modes from the same irrep would lower the symmetry of the system such that θ would become a fully symmetric coordinate at this reduced symmetry.

The derivative of the symmetric potential (AIII.1) w.r.t. any Q_i is also symmetric w.r.t. positive and negative distortions along θ:

$$\frac{\partial V(\theta, Q_2, \ldots, Q_N)}{\partial Q_i} = \frac{\partial V(-\theta, Q_2, \ldots, Q_N)}{\partial Q_i} \tag{AIII.2}$$

Therefore, the $\{Q_i^{opt}\}_{i=2}^{N}$ defined by Eq. (IV.17) are also even functions of θ:

$$Q_i^{opt}(\theta) = Q_i^{opt}(-\theta), \tag{AIII.3}$$

which means that the derivative of the $\{Q_i^{opt}(\theta)\}$ w.r.t. θ is zero at $\theta = 0$:

$$\frac{\partial Q_i^{opt}(\theta)}{\partial \theta}|_{\theta=0} = 0 \tag{AIII.4}$$

Let us now consider the Taylor expansion of the effective potential of Eq. (IV.15), $V_\Phi(\theta)$, around $\theta = 0$ and analyze its quadratic terms w.r.t. θ. For the diabatic effective potential, we have:

$$V_\Phi(\theta) \approx V(\theta, Q_2^{eq}, \ldots, Q_N^{eq})|_{\theta=0} + \frac{1}{2}\frac{\partial^2 V(\theta, Q_2^{eq}, \ldots, Q_N^{eq})}{\partial \theta^2}|_{\theta=0} \cdot \theta^2 + \ldots, \tag{AIII.5}$$

where terms with higher powers of θ are neglected (the term linear in θ is absent because $\theta = 0$ corresponds to the equilibrium geometry, i.e. $\frac{\partial V}{\partial \theta}|_{\theta=0} = 0$). The potential above is simply the harmonic potential for the OPLA normal mode with the curvature defined by the second derivative at the equilibrium geometry.

Likewise, for the adiabatic effective potential we have:

$$\begin{aligned} V(\theta, Q_2^{eq}(\theta), \ldots, Q_N^{eq}(\theta)) \approx V(\theta, Q_2^{eq}, \ldots, Q_N^{eq})|_{\theta=0} + \\ \left(\frac{1}{2} \frac{\partial^2 V(\theta, Q_2^{eq}, \ldots, Q_N^{eq})}{\partial \theta^2}|_{\theta=0} + \right. \\ \sum_{i=2}^{N} \frac{\partial^2 V(\theta, Q_2^{eq}, \ldots, Q_N^{eq})}{\partial \theta \partial Q_i} \frac{\partial Q_i^{eq}(\theta)}{\partial \theta}|_{\theta=0} + \\ \frac{1}{2} \sum_{i,j=2}^{N} \frac{\partial^2 V(\theta, Q_2^{eq}, \ldots, Q_N^{eq})}{\partial Q_i \partial Q_j} \frac{\partial Q_i^{eq}(\theta)}{\partial \theta} \frac{\partial Q_j^{eq}(\theta)}{\partial \theta}|_{\theta=0} + \\ \left. \sum_{i=2}^{N} \frac{\partial V(\theta, Q_2^{eq}, \ldots, Q_N^{eq})}{\partial Q_i} \frac{\partial^2 Q_i^{eq}(\theta)}{\partial \theta^2}|_{\theta=0} \right) \cdot \theta^2 + \ldots \end{aligned} \tag{AIII.6}$$

Taking into account Eqns. (AIII.4) and (IV.17), one sees that the harmonic coefficients in Eq. (AIII.5) and Eq. (AIII.6) are identical.